DEVELOPMENT OF VISION SKIN: A PROXIMITY AND IMAGING SENSOR

by

Darren Edward Bergen

B.A.Sc., Simon Fraser University, 1994

THESIS SUBMITTED IN PARTIAL
FULFILLMENT OF THE REQUIREMENTS
FOR THE DEGREE OF MASTER OF APPLIED
SCIENCE
in the Faculty
of
Engineering Science

© Darren E. Bergen 1996

SIMON FRASER UNIVERSITY

April 1996

All rights reserved. This work may not be
reproduced in whole or in part, by
photocopy or other means, without
permission of the author

APPROVAL

NAME: Darren E. Bergen

DEGREE: Master of Applied Science in Engineering Science

TITLE: Development Of Vision Skin: A Proximity And Imaging Sensor

Examining Committee

Chair:

Dr. Shawn Stapleton
Associate Professor
School of Engineering Science

Senior Supervisor:

Dr. Glenn Chapman
Associate Professor
School of Engineering Science

Supervisor:

Dr. Andrew Rawicz
Associate Professor
School of Engineering Science

External Examiner:

Dr. William S. McMath
Space Technology Division
Canadian Space Agency

Date Approved: April 9 '96

PARTIAL COPYRIGHT LICENSE

I hereby grant to Simon Fraser University the right to lend my thesis, project or extended essay (the title of which is shown below) to users of the Simon Fraser University Library, and to make partial or single copies only for such users or in response to a request from the library of any other university, or other educational institution, on its own behalf or for one of its usrs. I further agree that permission for multiple copying of this work for scholarly purposes may be granted by me or the Dean of Graduate Studies. It is understood that copying or publication of this work for financial gain shall not be allowed without my written permission.

Title of Thesis/Project/Extended Essay

"Development of Vision Skin: A Proximity And Imaging Sensor"

Author:

(signature)

D. Bergen
(name)

April 11 '96
(date)

ABSTRACT

A new sensor called "Vision Skin" was built and studied in this thesis. Aimed at robotic applications it will give a high accuracy proximity height measurement of approaching objects and also generate a low resolution image. The sensor operates in the near range from between 0 to 20 mm, from the surface of contact. The proximity mode operation uses laser triangulation of the object's surface in combination with the imaging capability. The sensor makes use of an array of small holes in thick material, called a mask. The mask was created in 500 micron thick polypropylene using an Argon ion laser. The holes produced were 30 microns in diameter with a hole to hole spacing of 150 microns. These small holes created small acceptance angles (3.4 degrees), thus restricting the amount of light seen by the sensor. With the mask the sensor needs no lenses for the imaging or proximity modes and thus no depth of focus problems occur in the close range. To measure proximity, a laser spot is projected onto the surface of the object to be observed. The hole with the largest intensity is the location over the sensor surface of the laser spot. The restricted light action of the mask means the location of the spot can be accurately determined and with the angle of the laser beam simple trigonometry can be used to calculate height. The tested prototype used modified charged coupled device (CCD) sensors with the masks placed on the photoarray. Experiments have shown the sensors have a proximity accuracy ranging from +/- 0.033 mm at 1 mm to +/- 0.067 mm at 2 mm using an interpolation of light intensities. At distances of 0 to 6 mm, the sensor is capable of imaging a simple object. An integrated circuit was designed in Mitel 1.5 micron CMOS to integrate both the proximity extraction and photodetection. The circuit was simulated, and submitted to CMC. Further work on the sensor requires integration of the laser, and faster acquisition hardware and software.

ACKNOWLEDGMENTS

Versions of this sensor are currently patent pending. This work was sponsored by the Canadian Space Agency under the STEAR 7 program and was done in cooperation with Kinetic Sciences Inc. of Vancouver, BC. Funding for the equipment was received from NSERC and the BC Advanced Systems Institute.

Also I would like to thank Dr. Chapman, Taranjit Singh, T.S. Weeks for their help.

TABLE OF CONTENTS

APPROVAL ii

ABSTRACT iii

ACKNOWLEDGMENTS iv

LIST OF FIGURES viii

LIST OF TABLES xiii

CHAPTER 1: INTRODUCTION 1

CHAPTER 2: CONCEPTION AND OPERATION 4
- 2.1 Proximity Measurement 5
- 2.2 Imaging 11
- 2.3 Multilayer Masks 14
- 2.4 Charge Coupled Device 19
- 2.5 Summary 22

CHAPTER 3: MANUFACTURE OF SENSOR 23
- 3.1 Equipment 23
- 3.2 CCD Sensors 26
- 3.3 Image Acquisition Boards 30
- 3.4 Mask Production 31
  - 3.4.1 Material 32
  - 3.4.2 Early Laser Processing Result 32
  - 3.4.3. Laser Processing Results 34
    - 3.4.3.1. Threshold Power 35
    - 3.4.3.2. Tabulated Results 36
    - 3.4.3.3. Optimum Parameters 38
    - 3.4.3.4 Mask Density 38
  - 3.4.4 Double Multilayer Mask 39
- 3.5 Gluing 41
- 3.6 Summary 42

CHAPTER 4: LENSLESS IMAGING 43
- 4.1 Theory of Operation and Simulation 43
- 4.2 Set-up for Lensless Imaging 48
- 4.3 Imaging from High Density Sensor 49
- 4.4 Simulation of High Density Mask Viewing Checkerboard Pattern 53
- 4.5 Imaging from Double Mask 55
- 4.6 Summary 57

CHAPTER 5: PROXIMITY MEASUREMENT 58
5.1 Simulation of Gaussian Beam 58
5.2 Center of Gaussian 60
5.3 Angled Laser Experiments 64
5.3.1 Experimental Set-Up 64
5.3.2 Results 66
5.4 X-Y Table Laser Experiments 69
5.4.1 Experimental Set-Up 69
5.4.2 Results 71
5.5 Discussion of Errors 73
5.5.1 Simulation of Ideal Sensor Error 74
5.5.2 Simulation of Large Homogenous Hole Diameters 75
5.5.3 Simulation of Differential Hole Diameters 76
5.5.4 Calibration 78
5.5.4.1 Corrected Formula 78
5.5.4.2 Correction of Simulation 80
5.5.4.3 Correction of Data 81
5.6 Summary 82

CHAPTER 6: INTEGRATED PROXIMITY SENSOR 84
6.1 Concept 84
6.2 Photodiode Cell 86
6.3 Current Comparator 88
6.4 Control Circuit 89
6.5 Simulation 92
6.5 Second Design Improvements 94
6.6 Status of Integrated Proximity Sensor 95
6.7 Summary 96

CHAPTER 7: FUTURE DESIGN 97
7.1 Integrated Laser 97
7.2 Large Photoarrays 98
7.3 Real Time Acquisition Boards 99
7.4 Mask Hole Patterns 100
7.5 Double Masking 100
7.6 Angled Holes 101
7.7 Summary 102

CHAPTER 8: CONCLUSION 103

APPENDIX A: CODE FOR PARSING IMAGE FILE 105

APPENDIX B: PROPERTIES OF POLYPROPYLENE 108

APPENDIX C: CALCULATIONS FOR POINT LIGHT SOURCE 110

APPENDIX D: CODE FOR SIMULATING THE DETECTOR 117

APPENDIX E: CODE FOR SIMULATING CHECKERBOARD PATTERN 119

APPENDIX F: CODE FOR SIMULATION OF GAUSSIAN BEAM 122

APPENDIX G: CODE FOR CALCULATING POSITION 124

APPENDIX H: HSPICE CODE FOR SIMULATION OF INTEGRATED PROXIMITY SENSOR 126

APPENDIX I: CODE FOR EDC1000L 132

REFERENCES 137

LIST OF FIGURES

Figure 1-1: Active range finding through triangulation
(right triangle geometry shown) 2

Figure 2-1: Diagram of mask proximity detector 4

Figure 2-2: Proximity measurement with mask sensor 5

Figure 2-3: Magnified view of shadowed detectors 7

Figure 2-4: Proximity detection with a gaussian laser spot 9

Figure 2-5: Proximity sensor cone of acceptance 11

Figure 2-6: Overlap of acceptance cone 13

Figure 2-7: Attenuation of ideal spot at a height of 1 mm,
for 30 μm holes in 500 μm mask 14

Figure 2-8: Multilayer mask proximity sensor 16

Figure 2-9: Three mask proximity sensor 18

Figure 2-10: Operation principle of CCD analog shift register 20

Figure 2-11: CCD array 21

Figure 3-1: Laser control table 24

Figure 3-2: Microscope and laser beam 25

Figure 3-3: Support stand for polypropylene samples 26

Figure 3-4: TC211 mechanical data, unit in mm (inches) 26

Figure 3-5: TC245 mechanical data, unit in mm (inches) 27

Figure 3-6: Example of virtual detector 28

Figure 3-7: Parsing example 29

Figure 3-8: Polypropylene with a 50 mm focal length lens 35

Figure 3-9: Cross sectional view of a hole 38

Figure 3-10: Alignment holes for double mask 39

Figure 3-11: Alignment of masks 40

Figure 3-12: Image of rows of holes in TC211 mask 41

Figure 4-1: Intersection of light circle and detector 44

Figure 4-2: Simulation results of a light point source of light moving across detector with 30 μm holes and an aspect ratio of 16.7 47

Figure 4-3: Lensless imaging set-up 48

Figure 4-4: 1 mm checkerboard pattern at a height of 484 μm with TC211, 30 μm holes, 16.7 aspect ratio and 150 μm hole spacing 49

Figure 4-5: Parsed image of 1 mm checkerboard pattern at a height of 484 μm with TC211, 30 μm holes, 16.7 aspect ratio and 150 μm hole spacing 50

Figure 4-6: 1 mm checkerboard pattern at a height of 1119 μm with TC211, 30 μm holes, 16.7 aspect ratio and 150 μm hole spacing 50

Figure 4-7: 1 mm checkerboard pattern at a height of 2389 μm with TC211, 30 μm holes, 16.7 aspect ratio and 150 μm hole spacing 51

Figure 4-8: Checkerboard pattern at a height of 6120 μm with TC211, 30 μm holes, 16.7 aspect ratio and 150 μm hole spacing 51

Figure 4-9: Image correction of checkerboard pattern at a height of 6120 μm with TC211, 30 μm holes, 16.7 aspect ratio and 150 μm hole spacing 52

Figure 4-10: Simulation of checkerboard pattern at a height of 500 μm with 30 μm holes, 16.7 aspect ratio and 150 μm hole spacing 54

Figure 4-11: Simulation of checkerboard pattern at a height of 1100 μm with 30 μm holes, 16.7 aspect ratio and 150 μm hole spacing 54

Figure 4-12: Simulation of checkerboard pattern at a height of 2400 μm with 30 μm holes, 16.7 aspect ratio and 150 μm hole spacing 54

Figure 4-13: Simulation of checkerboard pattern at a height of 6100 μm with 30 μm holes, 16.7 aspect ratio and 150 μm hole spacing 55

Figure 4-14: Double mask with 1 mm checkerboard pattern at a height of 496 μm with TC211, 30 μm holes, 7.9 aspect ratio and 300 μm hole spacing....56

Figure 4-15: Double mask with 1 mm checkerboard pattern at a height of 5001 μm with TC211, 30 μm holes, 7.9 aspect ratio and 300 μm hole spacing 56

Figure 4-16: Double mask with 1 mm checkerboard pattern at a height of 7997 μm with TC211, 30 μm holes, 7.9 aspect ratio and 300 μm hole spacing....57

Figure 5-1: Simulation results of a laser spot moving across detector with 30 μm holes, an aspect ratio of 16.7 at a varying heights 59

Figure 5-2: Intersection of lines for center of laser spot....61

Figure 5-3: Simulation of laser spot in center of max. detector assuming 144 μm hole spacing 62

Figure 5-4: Simulation of laser spot in middle of max. and min. detector assuming 144 μm hole spacing 62

Figure 5-5: Set-up for angled laser experiments....64

Figure 5-6: Comparison of data and ideal gaussian beam for laser angled experiment with TC211, 33 μm holes and 16.7 aspect ratio....65

Figure 5-7: Graph of angled laser height measurements with TC211, 33 μm holes and 16.7 aspect ratio....66

Figure 5-8: Graph of error for angled laser height measurements with TC211, 33 μm holes and 16.7 aspect ratio....67

Figure 5-9: Graph of error using the brightest detector with TC211, 33 μm holes and 16.7 aspect ratio....67

Figure 5-10: Graph of error for a starting height of 3502 μm with TC211, 33 μm holes and 16.7 aspect ratio....68

Figure 5-11: Set-up for X-Y table laser experiments....70

Figure 5-12: Parsed image of laser spot for TC211, 16x17 holes, 30 μm holes, and 16.7 aspect ratio 71

Figure 5-13: Comparison of data and ideal gaussian beam for X-Y table laser experiment with TC211, 33 μm holes and 16.7 aspect ratio 71

Figure 5-14: Graph of error for a height of 1000 μm with TC211, 33 μm holes and 16.7 aspect ratio 72

Figure 5-15: Graph of error using the brightest detector for a height of 1000 μm with TC211, 33 μm holes and 16.7 aspect ratio 72

Figure 5-16: Graph of error at a height of 2000 μm with TC211, 33 μm holes and 16.7 aspect ratio 73

Figure 5-17: Error from simulation of ideal sensor with 30 μm holes, 16.7 aspect ratio and 144 μm spacing 74

Figure 5-18: Error from simulation of 40 μm holes, 12.5 aspect ratio and 144 μm spacing 76

Figure 5-19: Error from simulation of differential diameters 77

Figure 5-20: Error of un/corrected simulation data at 1000 μm, with differential hole sizes 80

Figure 5-21: Error of corrected simulation of differential hole diameters 81

Figure 5-22: Graph of error for calibrated proximity data at a height of 1000 μm 81

Figure 6-1: Layout of integrated proximity sensor (3.1 mm x 3.1 mm) 85

Figure 6-2: Picture of integrated proximity sensor (3.1 mm x 3.1 mm) 85

Figure 6-3: Layout of photodiode cell (200 μm x 200 μm) 87

Figure 6-4: Circuit diagram of photodiode cell 87

Figure 6-5: Circuit diagram of current comparator 89

Figure 6-6: Circuit diagram of control circuit 90

Figure 6-7: Final and Winner registers 91

Figure 6-8: Timing diagrams from simulation of integrated proximity sensor 93

Figure 6-9: Circuit diagram of improvements 95

Figure 7-1: Prototype of integrated laser 97

Figure 7-2: Higher density grid array..100

Figure 7-3: Angled holes 101

Figure C-1: Three dimensional view of hole..110

Figure C-2: X-Y view of hole and light point 111

Figure C-3: Side view of light source..111

Figure C-4: Intersection of two circles 114

LIST OF TABLES

Table 2-1: Multilayer mask examples for 0.5 mm thick mask, 60 μm, and a hole to hole spacing of 300 μm 19

Table 3-1: Threshold power in Watts 35

Table 3-2: Hole and interspacing results 37

Table 3-3: Etch rate of optimum results 37

Table 3-4: Grid density for CCDs 38

Table 6-1: Integrated proximity sensor pseudo-code 86

Table 6-2: State table 92

CHAPTER 1: INTRODUCTION

Proximity detection or measurement of distance has many uses from measuring "flatness defect indexes of products in hot strip mills"[1] to planetary microrovers in terrain exploration[2]. For robotic systems working in a complex environment, proximity information allows for "manipulation, inspection, gauging and assembly tasks as well as for obstacle avoidance and object surface tracking"[3]. These same robotic systems can also be used as profilometers and scanners.

The measurement of proximity can be completed through numerous technologies such as electro-optic (triangulation), magnetic, capacitive, and inductive by measuring field strength and microwave ultrasonic by ranging[4]. Measuring fields have the disadvantage of being sensitive to small changes in the target environment and composition. For electo-optic, the range is small. Direct physical measurements are possible but can change or harm the target whereas the former technologies are non-intrusive.

The interest of this thesis is the electo-optic technology for proximity detection, in particular the use of a laser. Different techniques exist such as using the laser as a radar (lidar) in which "the source and reflected energies mix coherently to generate a radio

frequency (RF) signal whose frequency is proportional to the range"[4]. Other techniques require simply the measurement of the time of flight to calculate distance[5]. One common method involving lasers for proximity sensing is triangulation. A laser is used to project a spot on the target, and a image sensor (CCD) is used to detect the position of the spot. As the distance changes between the sensor and the target, the spot projected on the image sensor shifts. By measuring the shift, the change in distance can be known. The diagram in Figure 1-1, shows triangulation using right triangle geometry. The distance R is a function to the focal length of the receiving lens (f), the light displacement (d) and the separation (B).

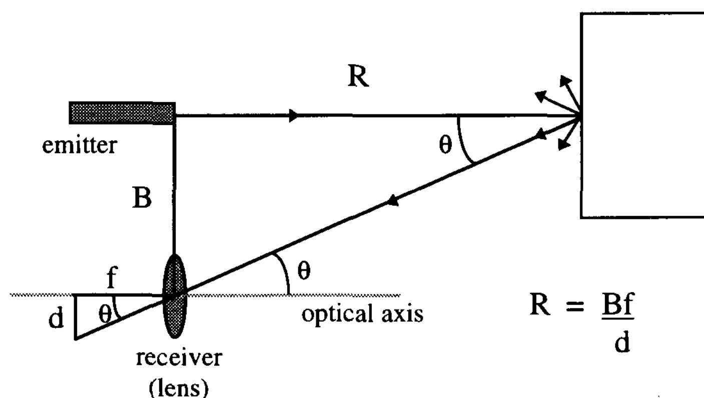

Figure 1-1: Active range finding through triangulation (right triangle geometry shown)[2]

In order to function the system in Figure 1-1 has to make use of lenses for the receiver (image sensor), which makes the unit bulky. The starting range for these types of systems are quite large for example, a point laser sensor (PLR) from Keyence has a starting range of 60 mm. The size of the assembly is 4.5 x 4.5 x 1.6 cms. Though large, this system is used as a wrist-mounted device for an industrial robotic arm[3].

The laser triangulation is also limited by speckle noise, which is caused by "coherent illumination in combination with rough surfaces"[6]. Some systems try to eliminate speckle by projecting a round spot on the target and placing a temporary image on a rotating diffuse glass plate[7].

Other problems with conventional triangulation are the method of finding the center of the gaussian laser spot. Problems arise in the formulas needed, as well as which pixels are part of the spot, and which are noise or speckle noise.

The Canadian Space Agency required small sensors for high accuracy proximity distance measurement of approaching objects and to also generate a low resolution image aimed at robotic applications. The sensor operates in the near range from between 0 to 20 mm, from the surface of contact. The proximity mode operation uses laser triangulation of the object's surface in combination with the imaging capability. The sensor makes use of an array of small holes in thick material, called a mask. The mask was created in 500 micron thick polypropylene using an Argon ion laser. The holes produced were 30 microns in diameter with a hole to hole spacing of 150 microns. These small holes created small acceptance angles (3.4 degrees), thus restricting the amount of light seen by the sensor. With the mask the sensor needs no lenses for the imaging or proximity modes and thus no depth of focus problems occur in the close range. To measure proximity, a laser spot is projected onto the surface of the object to be observed. The hole with the largest intensity is the location over the sensor surface of the laser spot. The restricted light action of the mask means the location of the spot can be accurately determined and with the angle of the laser beam simple trigonometry can be used to calculate height. The tested prototype used modified charged coupled device (CCD) sensors with the masks placed on the photoarray.

Chapter 2 describes the concept and operation of the sensor's proximity and imaging capability. The production of the mask and the sensor are shown in Chapter 3. In Chapter 4, the simulations of the sensor and the imaging results from experiments are shown. The simulations and experimental results from proximity detection are discussed in Chapter 5. The integrated proximity detector design is discussed as well as the simulations of the sensor in Chapter 6. Chapter 7 presents future designs of the proximity sensor and Chapter 8 is the conclusion.

CHAPTER 2: CONCEPTION AND OPERATION

The proximity sensor discussed in the thesis is a new design that is aimed at a short working distance (0-2 cm). The sensor consists of three major components: a photodetector, laser, and a matrix of openings or holes. This matrix, referred to further as a mask, sits on top of the photodetector as shown in Figure 2-1. The laser is fixed to the side of the detector at a set angle. One photodetector exists under each hole in the mask though in practice many detectors can be combined into a single detector for each hole. In a typical application the mask has 30 μm holes in 0.5 mm polypropylene, with a spacing around 150 μm from hole to hole center. The sensor has a thickness to hole diameter ratio (aspect ratio) of 16.7. Thus, the acceptance angle for light from this sensor is 3.4 °

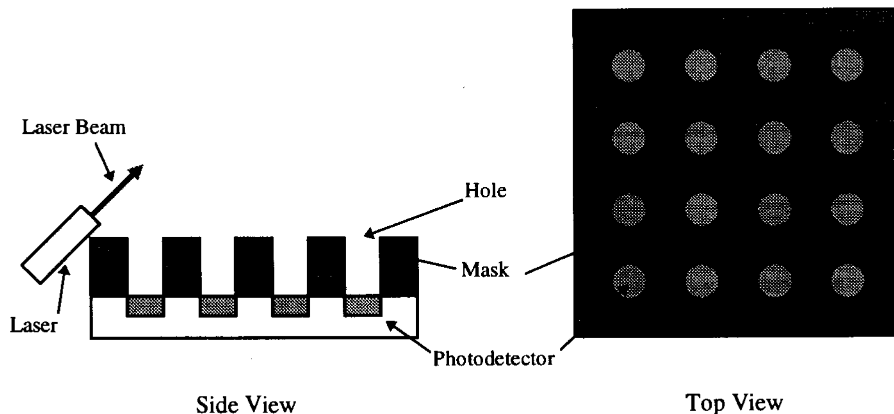

Figure 2-1: Diagram of mask proximity detector

A discussion of the proximity operation, vision capability, multilayer masking, and a short description of CCD sensors will be presented in this chapter.

2.1 Proximity Measurement

The shadow mask proximity detector measures distance with a form of laser triangulation as seen in Figure 1-1 but without the use of lenses. A laser spot is projected on the object whose height is to be measured. The sensor detects the position of the spot in order to calculate the distance. The example shown in Figure 2-2 demonstrates how distance is measured. The mask and hole dimensions are not to scale in this figure. Laser light is scattered off the surface of the object whose height is to be measured. In a first approximation, the laser light is assumed to be an ideal point source. The hole has a small acceptance angle, typically of 3.4°, for each photosensor and thus has a small area exposed to the scattered light. The surface of the object is also assumed to scatter most of the light as opposed to reflecting it. A small portion of the light maybe reflected off the object, but this light could be out of range of the sensor, or be blocked by the mask (for angles greater than 3.4 °) and not be seen by any of portion of the sensor.

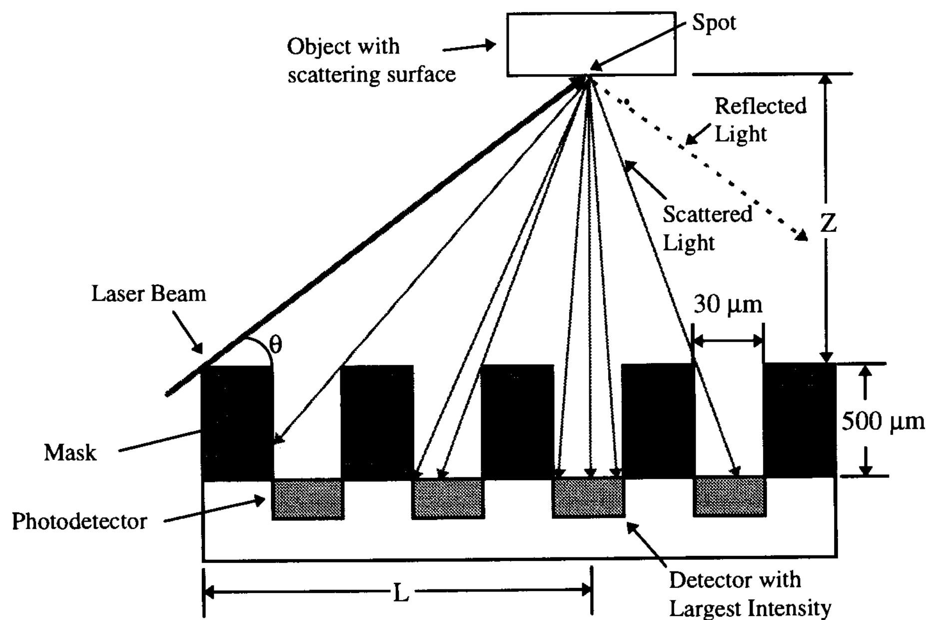

Figure 2-2: Proximity measurement with mask sensor

The position of the spot over the matrix needs to be located for triangulation. In the simplest case of this sensor, the detector with the largest intensity value is the location of the spot over the sensor. Other detectors see less light due to the shadowing of the detector by the mask edge. Because the angle of the laser and the location of the spot are known, the height (Z), from the top surface of the mask, can be calculated as in equation (2-1).

$$(2\text{-}1) \quad Z = L\,\mathrm{Tan}(\theta)$$

By using simple trigonometry, the height can be calculated. The equation is similar to the one shown in Figure 1-1. The system is aimed at short working distance (less than 1 cm) operations. The advantage of this system is that a lens is not needed to project an image of the spot onto the surface of the image detector. Instead, only the brightest spot is used to determine the location of the spot. Also, the spot is always in focus so that the sensor operates from contact on out.

If the object was titled at a large angle (e.g. 45 ^{o}), the reflected light component could reflect down a hole, but the sensor's application is for robotics for close heights (0-2 cm) and thus not very large object angles could exist.

For a point source the light is attenuated by the shadow of the mask for detectors and holes further from the projected laser spot. The example in Figure 2-2 shows the mask blocking the light on detectors a distance away from the laser spot. A greater difference in intensity exists between light detectors directly under the spot and those further from it. If no mask existed on the detectors, a smooth change in attenuation would exist and increase the possible error in determining the largest value. Figure 2-3 shows an magnified view of two detectors being shadowed from the spot by the mask.

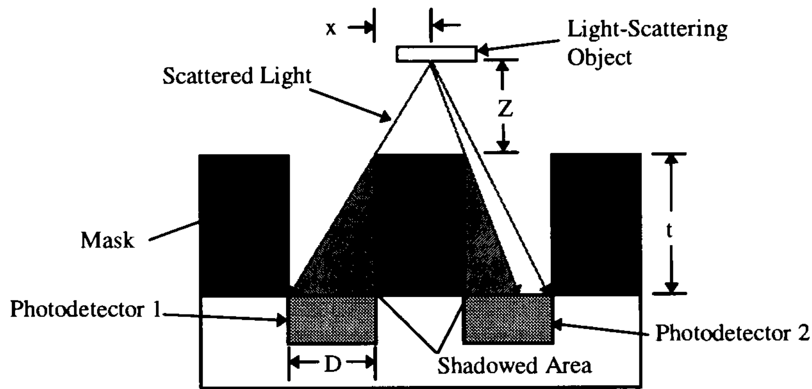

Figure 2-3: Magnified view of shadowed detectors

Photodetector 2 is shown such that only part of the detector is covered by shadow. For detector 1, the area is totally shadowed by the mask. The formula in (2-2) is the condition in which the detector will be totally shadowed by the mask.

$$\frac{Z}{x} \leq \frac{t}{D} \quad (2\text{-}2)$$

Where the variables are: Z is the height from the top of the mask to the object being measured, x is the distance from the edge of the detector to the spot, D is the diameter of the hole, and h is the thickness of the mask. As can be seen from Figure 2-3, the equation (2-2) is the condition when the angle of the scattered light ray is less than or equal to the angle created by the top near corner to the bottom far corner of the sensor. The tangent of this angle is the thickness of the mask over the diameter of the hole. This ratio is referred to as the aspect ratio. The formula (2-2) is a condition in that any of the parameters can change. For a constant aspect ratio, the mask can shadow the spot by decreasing in height or by increasing the horizontal distance (x).

The shadow mask has been demonstrated with simple geometric optics but two other factors exists which have negligible effects on the performance of the mask. The first is diffraction through the hole openings of the mask. The hole can be treated as a circular aperture. The light pattern created from this diffraction would be concentric circular rings

with most of the energy contained in the central maximum or within the range of the first minimum. Equation (2-3) shows the angle of the first minimum for diffraction of a circular aperture where λ is the wavelength of light, D the diameter of the hole, and θ_{min} the angle of the minimum. For a 30 μm hole and a laser wavelength of 670 nm (largest wavelength that will be used), the angle of the first minimum is 1.6 degrees. The first minimum can be considered the edge of the central maximum. The effect is to gather some light rays with angles larger than the acceptance angle of 3.4 °. Diffraction would be the limiting factor to the performance of the mask when the holes become smaller.

$$(2\text{-}3) \quad \mathrm{Sin}(\theta_{min}) = \frac{2.44\lambda}{D}$$

The second factor is the assumption that all light hitting the sidewalls of the holes are fully absorbed. Assuming that sidewalls only absorb 90 percent of the light, 10 percent will be reflected. If the walls are perfectly straight (good assumption with the masks created), the angle would be reflected at the same angle of approach. Thus for light entering at an angle greater than half the aspect ratio, the beam would be reflected off two walls before reaching the detector, which would result in only 1% of the original light power. Thus with angles greater than 6.9^{o} the light would reflect off two walls and for angles from 3.4^{o} to 6.9^{o} would be reflected only off one sidewall with 10% of the original power. These light levels would have a small impact on the light that reaches the sensor with no reflections.

The advantage of this sensor is that no lenses are needed for viewing the spot. Lenses have the disadvantage of a limited viewing range, especially at close distances. The viewing distance for a lens is limited by the focal length. To create a lens which would operate at distances up to 1 mm would require a focal length of 1 mm. Such a lens would be thick and bulky and would be out of range for viewing distances greater than 1 mm.

The mask for this sensors offers a small assemble, close operating range, and a larger range of distance.

The proximity measurement and shadowing has been shown for a point source of light, but it will work for a laser spot (up to a radius of 200 μm), which has finite radius, and with a gaussian intensity distribution. Chapter 5 shows the experimental usage of vision skin with a laser spot for proximity purposes. Essentially, the laser beam is an infinite number of light points, in which the intensity changes over distance which tends to create a Gaussian light distribution. Equation (2-4) is the formula for the gaussian distribution, where r is the distance from the center of the beam, and w is the laser spot radius ($1/e^2$ value).

$$\text{(2-4)} \quad I(r) = \exp\left(\frac{-2r^2}{w^2}\right)$$

The diagram in Figure 2-4, shows a laser spot being scattered on the object. The brightest detector still qualifies as the location of the spot over the mask and thus the height of the object can be calculated with equation (2-1).

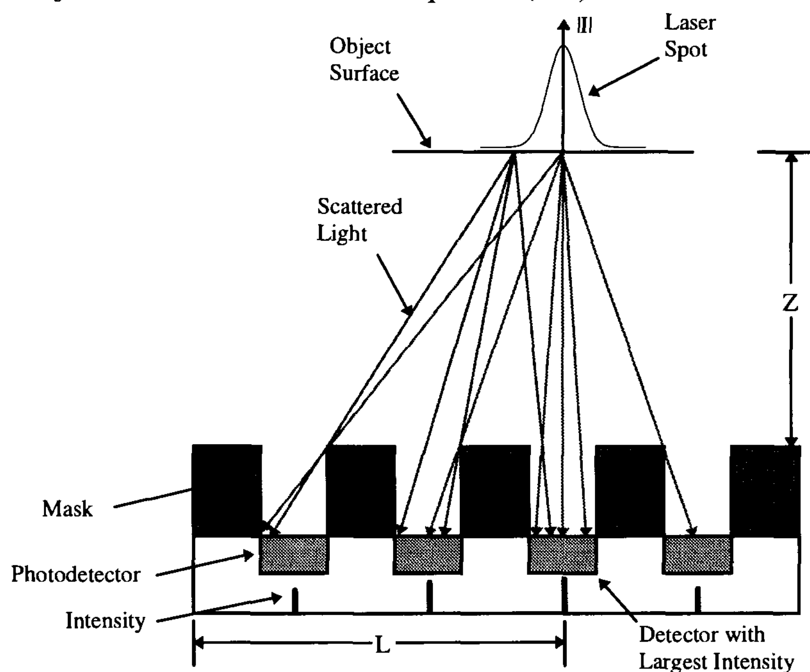

Figure 2-4: Proximity detection with a gaussian laser spot

The difference with the gaussian spot is that the scattered laser light is seen from detectors further from the spot. Near the tail ends of the beam, the beam intensity is low, and even though seen further out, does not register much intensity for these detectors.

The object in Figure 2-4 is shown as being parallel to the surface of the mask but a small angle could exist, which would change the spot shape. The beam spot would become slightly elliptical and some areas of the spot would be closer to the detectors (brighter). The effects would be minimal because the angle will not be large and the changes in distance would be small.

For the scattering of the light when projected from the top of the diffuser, the light distribution is not even and follows a cosine law. The sensor can only accept light at angles of 3.4°, thus this is the largest angle seen from the scatter resulting in 99.8% of the original intensity being projected. Of course this scattering only results when light is projected from above the diffuser (Figure 2-1 and 2-2).

As will be shown in Chapter 5, the detector with the largest intensity is still the valid location of the laser spot. The detector under the spot is exposed to light from the center of the beam as well as the tail ends. The effect of a finite sized gaussian spot is to extend the horizontal X distance over which detectors receive illumination, but the detector closest to the center of the spot still has the largest intensity. As in Figure 2-4, with a gaussian spot a larger light induced signal exists for all the detectors, including the fringes, than with a point source.

Not only is the sensor lensless, but no need exists to search for the center of the gaussian. Using a gaussian spot requires that the center of the spot be calculated through algorithms. Different ways and conditions are discussed in a paper on how to determine the center of the spot [1]. For the masked proximity sensor, the gaussian center is integrated for a range, and the brightest detector indicates the location of the spot in the X-Y plane and thus the height. Of course the error for detection is limited by the spacing

of the detector, and in the simplest case detection of the brightest spot, the absolute error is plus or minus one half of the center to center spacing of the holes in the mask.

As with the point spot, if the mask did not exist the gaussian would be projected onto the whole surface of the sensor, resulting in a smooth distribution of intensities. The mask attenuates the laser beam through shadowing more than the inverse square of distance allowing for a greater difference between the detectors under the spot and those further away. Taking the brightest hole is a zeroth order technique for calculating proximity. Better results can be produced if an interpolation of the intensities of the different holes around the brightest is taken.

2.2 Imaging

The proximity detector, shown in Figure 2-1, also has the capability for imaging detection. This vision sensor is a side-effect of the holes' limited acceptance angle, and each detectors' ability to add or integrate the light. The diagram in Figure 2-5 demonstrates the ability of each detector to look at an object, which is assumed to be illuminated from below.

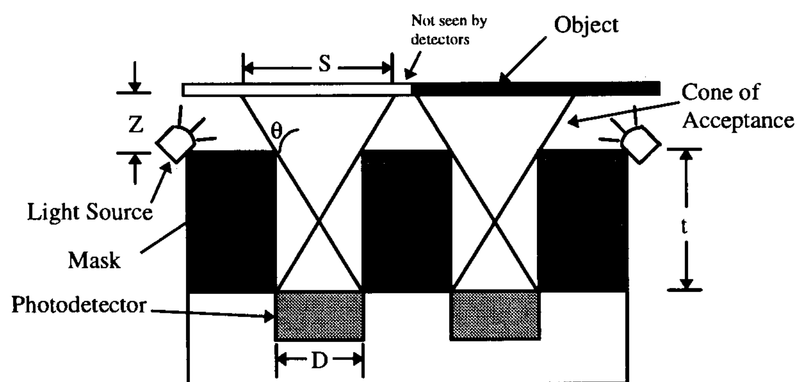

Figure 2-5: Proximity sensor cone of acceptance

Each detector has a cone of acceptance (round holes) that is dependent on the aspect ratio. The angle of acceptance, or θ, is calculated with the formula in (2-5) where D is the hole diameter and t is the mask thickness.

$$(2\text{-}5) \quad \theta = \tan^{-1}\left(\frac{D}{t}\right)$$

The acceptance spot (S) is the diameter of the circle on the object that can be viewed by a single detector at a specific height of Z.

$$(2\text{-}6) \quad S = D + 2\left(\frac{D}{t}\right)Z$$

As can be seen in Figure 2-5, each detector has a cone of acceptance, where a certain amount of light is gathered. Consider an object with checkerboard pattern (alternating light and dark areas) with a border centered between two holes. In the diagram, one sensor will record a high value, and the other will record a low value (white and black areas of the object respectively). The image seen by the sensor is one where each detector sees the average of an area of diameter S of the object directly over the detector. If the observed area overlaps an edge, the intensities seen become more "gray" or blurred out. Thus, a low resolution image of the object is seen. For a specific distance of Z from the top of the mask, the smallest detail that can be seen is of a circle of diameter S, assuming a flat plane.

Not only is the image of low resolution, but areas are not viewed when the object is too close. Figure 2-5 shows an area just between the two sensors which will not be seen by the sensor. As the object approaches closer, more area is not seen by the sensor but at the same time finer detail may be viewed, assuming of course that sufficient light can illuminate the surface.

The opposite is true for objects increasing in distance from the surface of the mask. More area is seen with a loss of detail. At some distance the cones of acceptance from neighbouring detectors will over lap, and detectors will start viewing areas seen by their neighbours. The height in which two cones will overlap is dependent not only on the aspect ratio but the center to center spacing (p) of the holes in the mask. Figure 2-6 demonstrates overlapping cones as well as the point where two cones intersect.

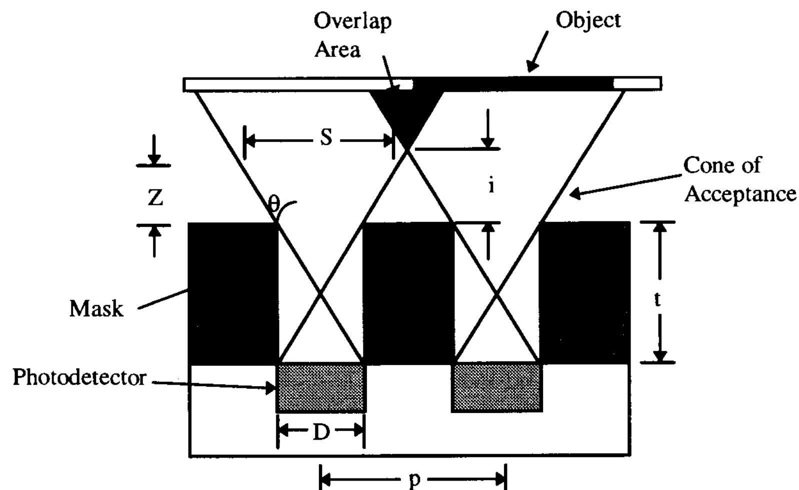

Figure 2-6: Overlap of acceptance cone

The formula for the height of intersection (i) is in (2-7). Because the dimensions are the same for all the holes, the intersection takes place at the half way point between the holes on the X-Y plane (parallel to the mask surface). The ratio between the intersection and distance from the edge of a hole has to be the same as the aspect ratio.

$$(2\text{-}7) \quad i = \left(\frac{t}{D}\right)\left(\frac{p-D}{2}\right)$$

As Figure 2-3 shows, light near the edge of area S emits into only part of the sensor. Thus, as with the proximity spot, the detector sees light at various intensities across the spot (See Chapter 4 for details). The graph in Figure 2-7 shows the attenuation of an ideal spot as it moves across a detector. At larger distances from the sensor, the intensity from the spot lessens. The flat portion of the graph around the zero displacement point is when the spot is over the hole and not shadowed by the mask. The intensity is reduced by the

inverse square law which has almost no effect because of the small distance change. The flat area corresponds to a distance of 30 μm which is the size of the hole.

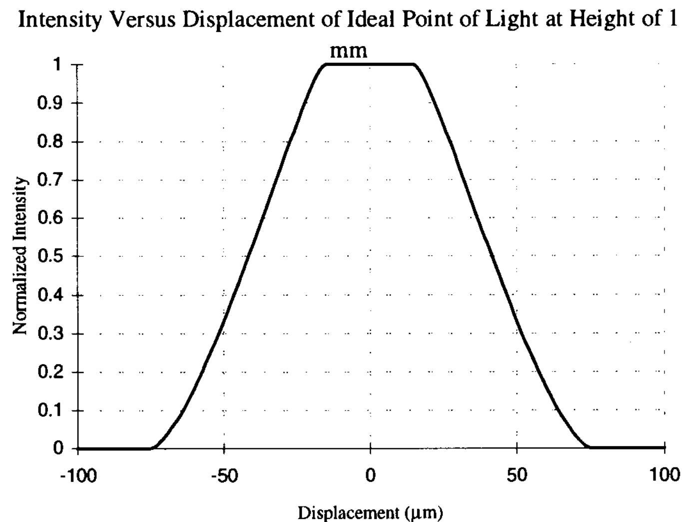

Figure 2-7: Attenuation of ideal spot at a height of 1 mm, for 30 μm holes in 500 μm mask

The vision skin detector has the ability to view objects but the range is limited. If too close, the sensor misses detail, and too far away, the areas of view overlap and blur and resolution declines. Thus a limited range exists on the sensor viewing. As a first estimate, to obtain a resolution equal to that of the hole spacing, an acceptable viewing range would be from a height of zero to a distance in which the cones of acceptance overlap by fifty percent, which would be (t/D)(p-D/2).

2.3 Multilayer Masks

As can be seen from both sections 2.1 and 2.2, the aspect ratio(t/D) is one of the determining factors in the performance of this sensor. For proximity, a larger aspect ratio would entail a larger height from the surface of the mask to the object, in which detectors would be in total shadow. To find the point where the mask totally shadows a detector and when the spot is over the middle of the detector next to it, use the distance in (2-8)

applied to equation (2-2) for the height in equation (2-9), where p is the spacing of the detector.

$$(2\text{-}8) \quad x = \left(p - \frac{D}{2}\right)$$

$$(2\text{-}9) \quad Z \le \left(\frac{t}{D}\right)\left(p - \frac{D}{2}\right)$$

The increase in aspect ratio means more shadowing occurs, and thus a greater difference in light intensities between detectors directly under the spot and those further away. Also, partial shadowing occurs at a larger height, making the sensor more responsive and accurate at larger distances.

For vision, a higher aspect ratio means less increase in the acceptance spot size as can be seen from equation (2-6). From equation (2-7) a larger aspect ratio allows for a larger height from the mask surface before neighbouring acceptance cones intersect, and thus better resolution at larger distances.

Larger aspect ratios can be created by using a smaller diameter hole, or a thicker mask material, but both will reach a limit. At this point, larger aspect ratios can still be created by using a multilayer masking process. A simple multilayer masking system just places one mask directly on top of the other, thus doubling the aspect ratio by doubling the apparent thickness of the mask.

A second technique is to create a gap between two masks, thus increasing the apparent thickness by a factor greater than two. Figure 2-8, demonstrates how this system works. Essentially, if the space is kept small enough, the light from the neighbour's top mask hole cannot fall onto the detector and must be shadowed by the bottom mask. Creating a line of sight from the neighbour's upper mask hole's top left corner to bottom right corner to the detector's bottom mask hole's top left corner to the bottom right is all that is needed to guarantee that no light enters from the neighbour. Any beams that enter at too shallow an angle will be blocked by the bottom mask; or the top mask.

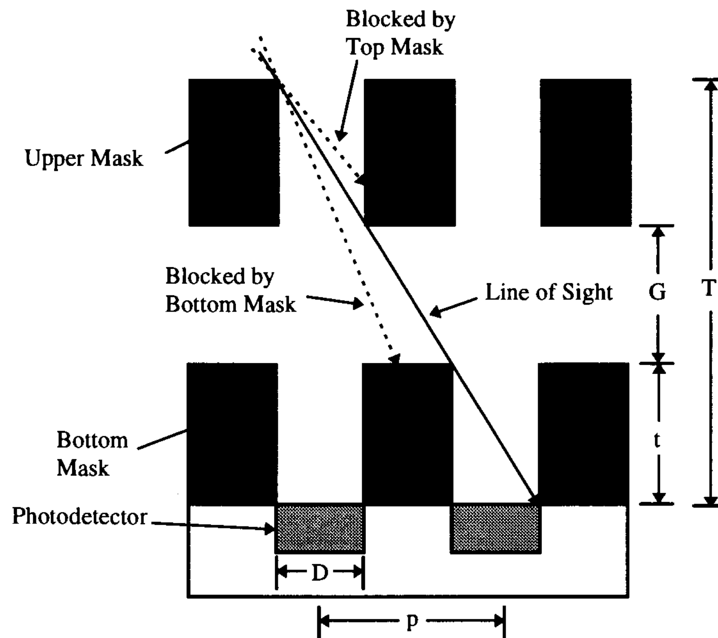

Figure 2-8: Multilayer mask proximity sensor. Dotted lines show blocked paths on either side of line of sight

The multilayer mask could act as a diffraction grating in which the top mask diffracts light, and the bottom mask causes the interference pattern. For a diffraction grating the intensity distribution is the interference pattern with an intensity modulation of the diffraction. As seen from equation (3-4), most of the intensities occurs with 1.6°, and thus the pattern from the grating would be the same as well. The effect would be minimal from this pattern. Another point is that the two masks would have to be sufficient distance from each other in order for light to reach neighbouring holes (spaced 150 μm apart). An approximate distance would be around 5.3 mm, and would require more than two masks (see table 2-1 for distances between masks).

Again, the aspect ratio and center to center line spacing determine the air space gap (G) as shown in equation (2-10). The same aspect ratio must exist for the line of sight (distance between detectors) as does the aspect ratio of the holes. The equation and diagram assume all dimensions are the same for both masks as well as a perfect alignment of the hole centers.

$$\text{(2-10)} \quad G = \left(\frac{t}{D}\right)(p - D)$$

The new thickness is the gap plus twice the thickness of the masks as shown in equation (2-11).

$$\text{(2-11)} \quad T = \left(\frac{t}{D}\right)(p - D) + 2t$$

Simplify (2-11) results in a thickness ratio in (2-12) which is also the multiplication of the original aspect ratio.

$$\text{(2-12)} \quad \frac{T}{t} = \left(\frac{p}{D} + 1\right)$$

The new aspect ratio is a multiple shown in (2-12) of the original aspect ratio. The multilayer masks acts as a full functioning mask but with a greater apparent thickness. The new aspect ratio is shown in (2-13)

$$\text{(2-13)} \quad \frac{T}{D} = \left(\frac{p}{D} + 1\right)\frac{t}{D}$$

The multilayer mask can then be used in conjunction with another single mask, such that the light does not fall from a neighbour as shown in Figure 2-9.

The same type of formula exists as in (2-10) for the gap except that the space between the detectors (p-D) has to a have a ratio with height equal to the new aspect ratio. Thus the new gap height is shown in (2-14).

$$\text{(2-14)} \quad G1 = \left(\frac{p}{D} + 1\right)\left(\frac{t}{D}\right)(p - D) = \left[\left(\frac{p}{D}\right)^2 - 1\right]t$$

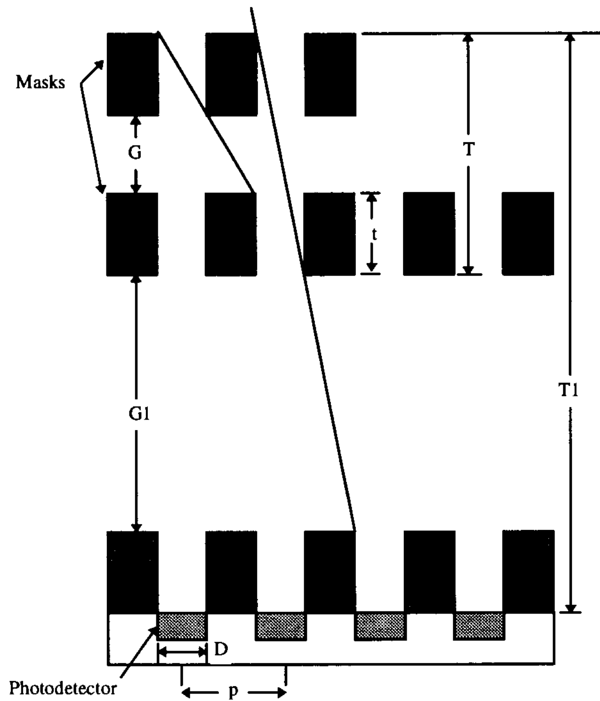

Figure 2-9: Three mask proximity sensor

Adding the new height, the thickness from (2-11) and one mask thickness results in a new thickness ratio of:

$$\text{(2-15)}\quad \frac{T1}{t} = \left[\left(\frac{p}{D}\right)^2 - 1\right] + \left(\frac{p}{D} + 1\right) + 1 = \left[\frac{\left(\frac{p}{D}\right)^3 - 1}{\left(\frac{p}{D} - 1\right)}\right]$$

The new effect aspect ratio is in equation (2-16):

$$\text{(2-16)}\quad \frac{T1}{D} = \left[\frac{\left(\frac{p}{D}\right)^3 - 1}{\left(\frac{p}{D} - 1\right)}\right]\frac{t}{D}$$

As seen, a number of masks can be joined to create a larger effective aspect ratio. The formulas in equation (2-17) and (2-18) show the gap spacing and effective aspect ratio for value n, which is the number of masks being used. These formulas produce the same results for 1,2 and 3 masks.

$$(2\text{-}17)\quad G(n) = \left[\left(\frac{p}{D}\right)^{n-1} - 1\right]t$$

$$(2\text{-}18)\quad A(n) = \left[\frac{\left(\frac{p}{D}\right)^{n} - 1}{\left(\frac{p}{D} - 1\right)}\right]\frac{t}{D}$$

Table 2-1 shows the gap spacing and the effective aspect ratio for different numbers of masks assuming a mask thickness of 0.5 mm, a hole diameter of 60 μm, and a hole to hole spacing of 300 μm.

Table 2-1: Multilayer mask examples for 0.5 mm thick mask, 60 μm, and a hole to hole spacing of 300 μm

Number of Masks	Gap (μm)	Aspect Ratio	Angle (Deg)
1	500	8.33	6.84
2	2000	50	1.14
3	12000	258.3	0.22
4	62000	1300	0.044

2.4 Charge Coupled Device

The system used for the sensor to gather light was a Charge Coupled Device (CCD) image sensor.

"Its fundamental structure consists of an MOS capacitor with an electrode attached on top of the silicon dioxide on the semiconductor substrate surface. When voltage is supplied between the electrode and substrate, a depletion layer is formed at the silicon dioxide and semiconductor interface, resulting in a potential well of low energy ranking for the minority carrier"[8].

If charge is created from light, it can be temporarily stored in the potential well. To facilitate the transfer of a signal (photoelectrons), these MOS capacitors are arranged next to each other, such that charge can be transferred from one MOS capacitor to the next,

thus creating an analog shift register. Figure 2-10 demonstrates the configuration as well as the applied control signals. At time t1, charge is stored under electrode $\phi 1$. Part of the charge under electrode $\phi 1$ is transferred to electrode $\phi 2$ at t2. The voltage on electrode $\phi 1$ is decreased further at t3, resulting in the total transfer of the charge under electrode $\phi 2$ at t4. When this cycle is repeated, the charge is shifted.

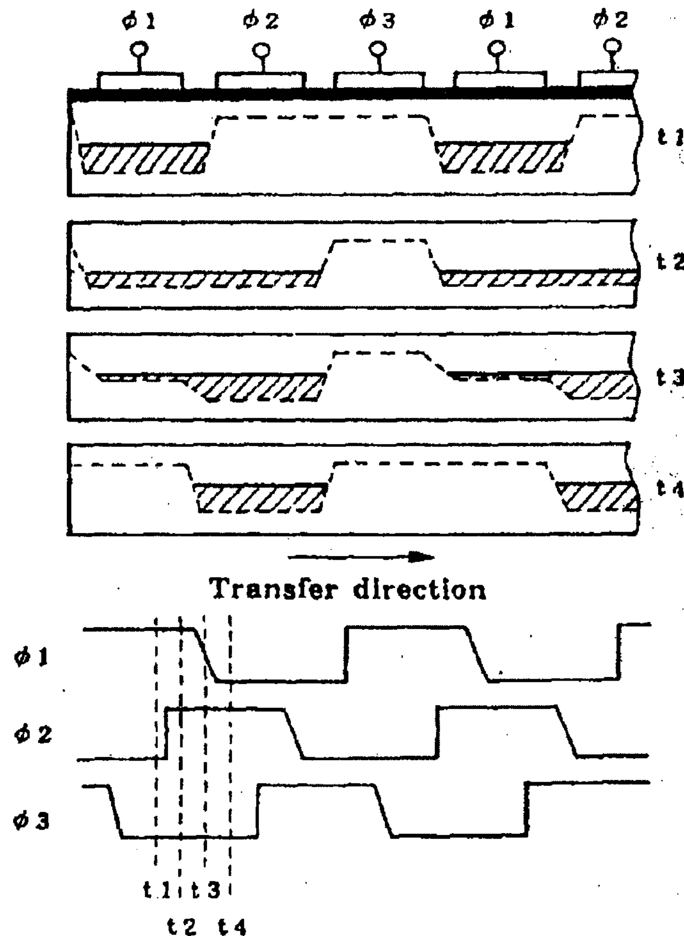

Figure 2-10: Operation principle of CCD analog shift register[8]

Light is converted to charge by the silicon and stored in the MOS capacitor. For a CCD array, the light gathering area also becomes the charge transfer region. Similar to Figure 2-10, the MOS capacitor can also contain light gathering circuitry. Each row of an array can be shifted into the neighbour row, thus allowing for light gathering and charge

transfer. Each row is then passed to a serial shift register and the charge is converted to a voltage for the output signal. Figure 2-11 demonstrates the configuration of an array. The advantage of CCD arrays, over other photogathering devices such as an array of photodiodes, is the lack of individual control lines for each photodiode which reduces the amount of area used. For the CCD array, one row contains one control line. The timing of the signals of these lines results in the transfer of charge.

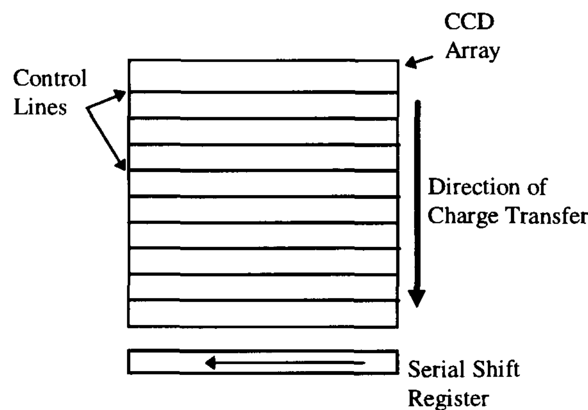

Figure 2-11: CCD array

CCD arrays are also devices readily available on the commercial market, as are the circuits to control and read the signals from the arrays. These items were necessary in order to create the proximity sensor.

CCDs have the advantage of being more sensitive to low light levels than a photodiode. A CCD collects light and converts it to charge, thus an integration of the light level can be created. For a photodiode, the light level is converted directly into current, and thus very large light intensities are needed to create a significant signal. The low currents can be used, but are more susceptible to noise. One disadvantage of CCDs is that they do have higher dark currents, since the dark currents are integrated over time as well as the light levels.

2.5 Summary

This chapter has introduced the basic operation of the sensor for proximity measurements and imaging. The explanation of the importance of the aspect ratio and the ability of the sensor to have a narrow acceptance of light were presented. Also discussed was the ability to join identical masks to create effectively larger aspect ratios thus decreasing the angle of acceptance. A brief explanation of CCDs was presented as this type of photocollection device was used in the creation of the sensor.

CHAPTER 3: MANUFACTURE OF SENSOR

The proximity sensor was a new design and in order to test the concept, a prototype had to built from scratch. Image devices and control circuitry were found and integrated with a mask which had to be fabricated in the microelectronics fabrication lab in Engineering Science. The major obstacle in the construction of this sensor was the fabrication of the mask which requires holes of <100 μm on spacing of <200 μm through a 0.5 mm material. Many different techniques could have been used, but the one which was focused on was to drill holes in materials with a laser beam using an accurate positioning table to locate the spots.

Discussed in this chapter is the equipment used for the construction of the mask, the type of CCD sensor used, image acquisition, mask production and the gluing of the mask. The mask production focuses on the material used, and the results of the laser drilling.

3.1 Equipment

An INNOVA 300 series Argon ion laser (488 nm) from Coherent, with a maximum power of 5.0 Watts and a beam radius of 1.5 mm, was used for fabrication of the mask. The samples of material were placed on an X-Y positioning system which uses laser

interferometery and has a repeatability of 0.1 μm. The X-Y table is controlled through an IBM PC computer. The laser and table are integrated into one complete system which is located in a 1000 class cleanroom. Figure 3-1 shows the layout of the laser, beam path and the table. The beam is reflected by four mirrors, into the objective lens.

The laser operates in a continuous mode, but the beam path travels through a KD*P electro-optic shutter which chops the beam into pulse streams with durations >2 μs. The shutter is controlled by a function generator and the function generator in turn is controlled by the same IBM PC that operates the X-Y table. The shutter has an on/off ratio of 30:1.

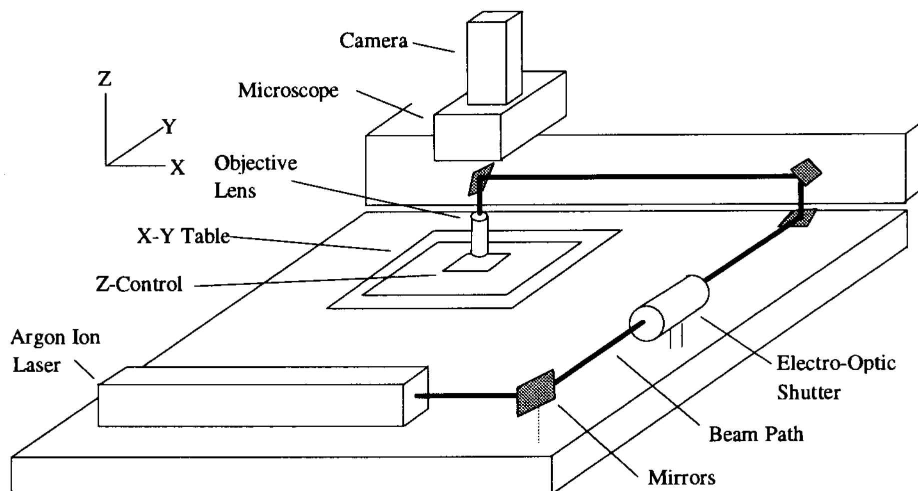

Figure 3-1: Laser control table

The last mirror under the microscope is a dielectric mirror, in which only the wavelength of the laser light will be reflected, while being transparent to other wavelengths. The wide wavelength microscope uses infinity corrected lenses which uses a parallel light source. This light can pass through the mirror, be focused by the lens, reflect off the object being processed, and travel back without reflection by the mirror. Figure 3-2 demonstrates the setup. The focusing lens also processes the laser light and thus when the object to be viewed is in focus, it is also in focus for the laser beam. The

microscope itself has a camera and the video signal is produced by the IBM PC through a video display card, which displays the image on the control computer.

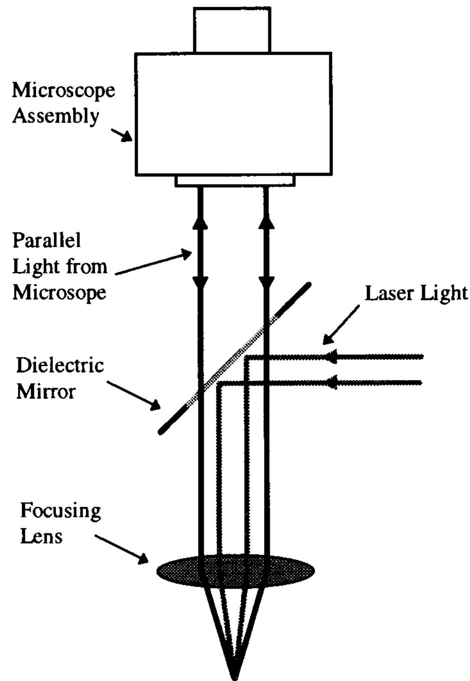

Figure 3-2: Microscope and laser beam

The materials to be processed by the laser are placed on top of a computer controlled Z-axis, again using the same IBM PC as used for controlling the X-Y table. The software used to run the X-Y table, electro-optic shutter and Z-axis is an in-house product controlled under MS Windows. The table can be controlled manually through the program or with a set of commands in a text file (script file). Both the control system and camera image are viewed on the PC's screen during operation.

The polypropylene samples were placed in a holder as shown in Figure 3-3. The holder creates an air gap under most of the sample, which reduces heat loss from the polypropylene. Placing the samples on an aluminum stand would increase the heat conductance, and a higher laser power would be needed. The air gap also allows for the beam to defocus, thus the laser energy that reaches the stand surface or reflects back to the sample has a sufficiently low power density.

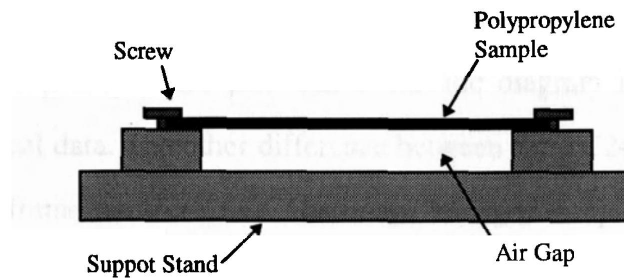

Figure 3-3: Support stand for polypropylene samples

3.2 CCD Sensors

The CCD sensors used for the construction of this device are Texas Instruments' TC211 and TC245. The TC211 consists of an array of 192x165 pixels, and the TC245 consists of 755x242 pixels.

The TC211 is the simpler of the two arrays. The array is smaller and contains only six terminals, which makes operating the TC211 easier. A schematic diagram of the TC211's physical package is shown in Figure 3-4. The total viewing area is 2640 µm by 2640 µm, with pixels of dimensions 13.75 µm by 16 µm. The TC211 uses only one clock to transfer charge row by row through the array. As each row is passed to the adjacent row, light can be collected by those cells, which results in a smearing of the image. The TC211 needs to be used in conjunction with some type of shutter, to stop any light falling upon the sensor when the charge transfer is taking place. An example would be a camera shutter, or pulsed light source.

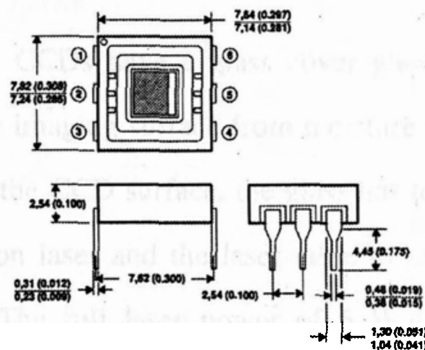

Figure 3-4: TC211 mechanical data, unit in mm (inches)[9]

The TC245 is a larger array with a total image area of 6417.5 μm by 4779.5 μm and a pixel size of 8.5 μm by 19.75 μm. The schematic diagram in Figure 3-5 shows the TC245's mechanical data. The other difference between the TC245 and the TC211 is that the array is a full frame-transfer CCD. The image (charge) is rapidly shifted to an array of identical size that is covered and not exposed to the light. For CCD arrays, the bottleneck in transferring the image is not the row transfer, but the serial shift of the columns of each row into the charge-to-voltage converter. For the TC245, the bottleneck is alleviated by transferring the image rapidly to a temporary storage area. Then the image is transferred from the temporary array to the serial shift register. Because the temporary array is protected from light, there is no light contamination, or smearing of the image. Also, using this sensor requires no shuttering device, since the shutter exists in electronic form on the array.

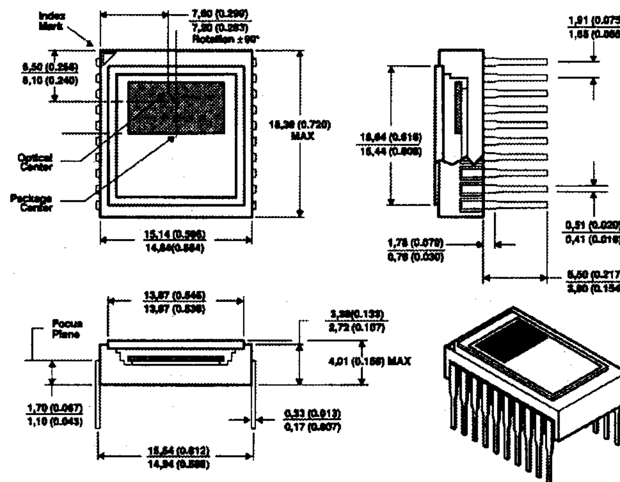

Figure 3-5: TC245 mechanical data, unit in mm (inches)[9]

When purchased, both CCDs have a glass cover glued to the top of the package which is used to protect the imaging surface from moisture and dirt. For the purposes of placing the mask on top of the CCD surface, the glass has to be removed. The glass was detached using an Argon ion laser and the laser table to expose the edges of the glass where the epoxy existed. The full laser power of 5 Watts with the 50x object lens focusing the spot onto the glass surface was used. The traversing of the edges in a back

and forth pattern with a 50 μm spot size, resulted in the glass cover lifting from the surface with some simple leverage, such as the tip of a tweezer.

One aspect of using the CCD, is that there are image detectors to spare, and they tend to be smaller (8 - 20 μm) then the holes (30 μm). The CCD array is such that the whole sensor is covered with photocells, and using the vision skin mask covers most of this, so only a few at illuminated areas will be needed. The solution is to ignore the detectors not needed, but this still leaves the problem of more than one detector per hole. Hence a virtual detector is created, which is nothing more than adding all the detectors that exist under one hole. An example is given in Figure 3-6, where four detectors exist under one hole. By adding all the sensors under the hole, a value for the total light falling in one hole can be calculated. The edges of the detectors not under the hole can be ignored because no light will fall upon them. The dark current from these areas may cause a problem, but by using a dark current image for each pixel (taken with no light) any error will be subtracted off.

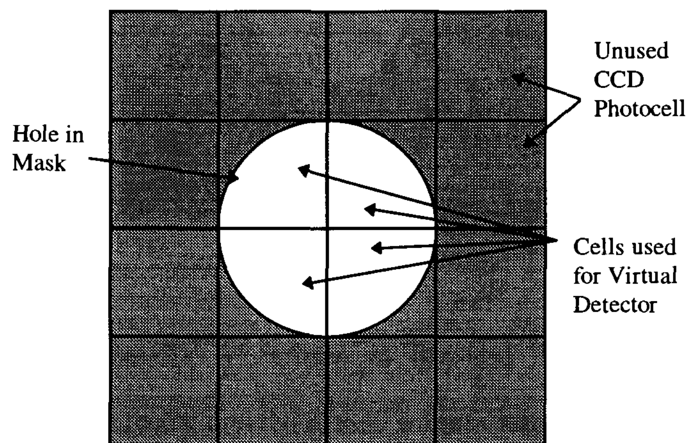

Figure 3-6: Example of virtual detector

To determine whether each pixel is under a hole is a large task, and requires the memory storage of which photocells belong to each hole. For the TC211 this would amount to either storing 31680 pixels with the corresponding hole values or storing all

pixels under a certain hole. Even with every 7th pixel being used, it would require storing and identifying 7920 pixels. An easier way is to parse areas of the image that correspond to a certain hole. The parsing area is just a square range, which represents most of pixels under a hole. The values are summed in this range and then stored in an array whose index is the virtual detector location. Thus only one value is needed for each virtual detector. Figure 3-7 demonstrates a parsing of part of an image. Of course square parsing for a round hole results in photocells that may be totally covered by the mask and offer no image information about the hole. Because these detectors are not exposed to light, they can only contribute dark current, and again by using dark current subtraction, this error is eliminated. With dark current subtraction, the parsing areas can be larger than the holes with no additional errors, as long as the area does not overlap another hole area.

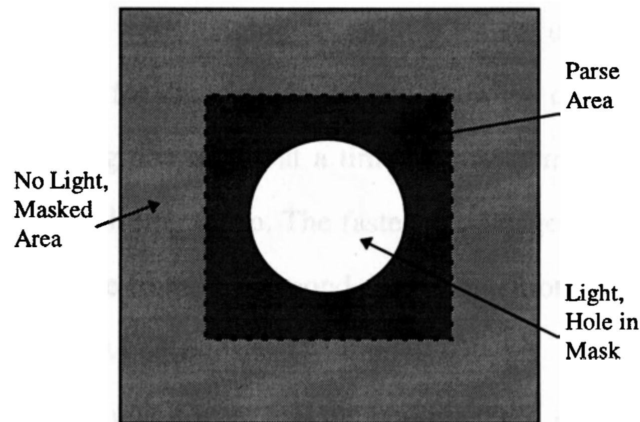

Figure 3-7: Parsing example

Parsing code exists in Appendix A, written in Borland TurboC 2.0. The parsing is specific to each proximity detector created due to orientations of the mask. The code also shows functions for reading the data files created by the acquisition boards. Both of these CCD arrays have boards that read and control them, and that are available on the commercial market.

3.3 Image Acquisition Boards

One reason for using the TC211 and TC245 from Texas Instruments was the availability of boards that would control and read the images from the CCDs. The two boards that controlled the TC211 and the TC245, were created from the CCD Camera Cookbook [10]. The book gives instructions for the construction of a fully working camera that connects to an IBM PC. For the thesis, the only items of interest were the CCDs and the boards.

The printed circuit boards were obtained from University Optics. The programs included with the CCD Camera Cookbook gave step by step instructions for building and debugging the circuits. I built three boards, two for the TC211 and one for the TC245.

Programs for grabbing and displaying an image from the camera were included in this book. These programs were running on an MSDos environment. The board makes use of the PC parallel port for data transfer to and from the camera. The camera boards were only capable of taking one image at a time. The system had to be used for single frame images instead of real time video. The fastest the image displayed, using a reduced view of the camera, was one frame per second. The acquisition boards allowed the image exposure time be set from 0.1 seconds to 15 minutes.

The advantages of this board were that the parts to build it were available, was fairly simple to put together, and had the software to take and store images on the computer. These images have a 12 bit accuracy, and can be stored on a hard drive or diskette. Functions in Matlab and C were written to read these data files, allowing for processing of the images, such as parsing. The most useful functions for small data sets was in Matlab allowing for easy displaying and analysis on the data. Both types of data files (TC211 and TC245) were created to be read by Matlab, which was running on a Sun Sparc station. Appendix A shows the C Code for reading the TC211 image files, which functioned well when a large number of data files needed to be analyzed. Also, because

of the relative simplicity of the boards and programs, older models of 80X86s could be used. Both a 486 and 286 were used in image acquisition. All cards are external to the computer, so only the parallel cable had to be plugged in.

3.4 Mask Production

Production of the mask was one important aspect of creating the sensor. No items were commercially available that would offer the aspect ratio or the spacing of the holes for a mask. The mask had to be created on the laser table discussed in section 3.1. Many different materials were processed using the laser, from plexiglass to wax. None of these created holes in thickness around 500 μm to 1 mm. Experiments by other researchers have resulted in depth-to-width (aspect) ratios ranging from 5:1 to 50:1 in metal sheets less than 1 mm in thickness, but used Copper Vapour Lasers (CVL) (30 W and 250-500 W)[11]. Holes with a 60 μm entrance hole diameter (exit diameter < 20 μm) have been laser drilled in 1 mm thick metals, but again used a CVL (50 W)[12]. Vias with 15-70 μm diameter have been created in 200 μm thick ceramic sheet using a frequency-doubled Nd:YAG laser[13]. Laser drilling of small holes has been reported with an Argon ion laser in 25 μm thick teflon, where 50 μm diameter holes were completed[14, 15], and the same sized holes were also drilled in 25 μm thick polyimide[16]. Not only were the aspect ratios low (0.5), but both experiments made use of ultrasonic cleaning to clear the holes. For our experiments no such post-processing of the drilled material was needed. Polypropylene was suggested by The Laser Institute (Edmonton, Canada) where experiments had been done on polypropylene using a 50 Watt, CO_2 laser with promising results.

Properties that make polypropylene useful are its low melting point of 168-175 ^{o}C, resistance to chemicals, low thermal conductivity (0.12 W/m-k). With its high electrical resistivity ($>10^{15}$ Ω-m), the masks will not adversely affect electronic circuits.[17].

3.4.1 Material

The material used for the early prototypes of the mask was a commercial white opaque polypropylene. The material was milled from a larger piece using a CAMM-3 machine. The final thicknesses used were between 400 μm and 500 μm.

Further experiments were conducted on black coloured polypropylene which would be more absorbent to laser light. Because thin black polypropylene is not available commercially, T.S. Weeks, a graduate student at the New Mexico Institute of Mining and Technology, produced black polypropylene with thicknesses of 0.25 mm, 0.5 mm, and 1 mm. The colouring for the polypropylene, was from a carbon black concentrate, manufactured by Reed-Spectrum of Sandoz Chemicals Corporation. The carbon concentrate were pellets with 50% carbon and 50% virgin polypropylene. The polypropylene, a virgin Marlex HLN-200 manufactured by Phillips Petroleum, was mixed with the carbon black concentrate pellets to a 10% mixture by weight. The materials were then compounded in a Custom Scientific Instruments' (CSI) Max Mixing Extruder, with an extruder temperature of 195 °C. The polypropylene mixture was then placed between two aluminum flashings and was preheated to 190 °C in a Carver Laboratory Hot Press. Shims were placed between the flashing to produce the desired thickness. After the flashings were at the proper distance, the material was allowed to cool at room temperature.

More information about the material from the manufacturer is contained in Appendix B.

3.4.2 Early Laser Processing Result

Different lenses and laser powers were used in the laser processing experiments to determine the optimal parameters. Lenses change the beam diameter and thus the

power density (Watts/m^2) and power, of course, changes the power density as well. Equation (3-1) is the formula for the new radius (w) of a Gaussian laser beam, through a lens with a focal length (f). The value w_o is the original radius or e^{-2} value of the beam before the lens and λ is the wavelength.

$$(3\text{-}1) \quad w = \frac{\lambda f}{\pi w_0}$$

Also looked at was the depth of focus (ΔZ), which is the distance where the beam radius expands by no more than 5 percent. Equation (3-2) shows the formula for the depth of focus where the value w_o, is the $1/e^2$ of the spot at the focal point of the lens.

$$(3\text{-}2) \quad \Delta z = \pm \frac{0.32\pi w_o^2}{\lambda}$$

The first early experiments were done with commercial white polypropylene. The best variables were a single lens with a focal length of 100 mm, a laser power of 5.12 W, 1000 pulses, and a 2 ms pulse with a 50 % duty cycle. The computer controlled electro-optic shutter allowed for multiple firings of a laser pulse. The beam radius from this lens (where λ ~ 488 nm, and beam radius = 1.5 mm) was 10.4 μm and from (3-2) the depth of focus was 220.9 μm. The resulting hole diameter was 127 μm in 500 μm thickness, which created an aspect ratio of only 3.9. All hole diameters change about 10 % from hole to hole. Another important feature was the spacing between hole centers and for these experiments, only a 500 μm spacing was achieved. The closer the holes are, the better accuracy for the XY alignment of a light source, where the error is ± hole spacing/2. When holes were too close, they would fill in the holes near them. Even with a 2-3 second delay between each hole drilling, this spacing was the closest that could be achieved. Not only was the aspect ratio and the spacing between holes (interspacing) poor, but the white polypropylene was translucent at a thickness of 500 μm, and thus did

not block all the light falling on the mask. Detectors which were between the holes and were covered by the mask would measure some light. Thus, the white polypropylene did not make an appropriate material for a mask.

The black polypropylene was a better material to work with and was completely opaque. Because of its black colouring, the material was more absorbent to laser light and required much lower power. For example, with a 1 mm thickness polypropylene sample, 144 μm diameter holes were created at a interspacing of 500 μm with a laser power of 0.97 Watts, 500 pulses (10 pulses x 50 times), 2 ms pulse with a 50 % duty cycle, and a lens of f = 100 mm. The power was reduced by a factor of 5, with a doubling of the aspect ratio. Unfortunately, the interspacing and hole size could not be reduced further with this thickness, so the 0.5 mm thick black polypropylene samples were experimented on.

Initial tests using the same lens (f = 100 mm), resulted in 63 μm diameter holes in 500 μm thick polypropylene with a hole spacing with a 300 μm hole spacing. The laser parameters used were 0.37 W, 250 pulses, and a 2 ms pulse with a 50% duty cycle.

For both black polypropylene samples, a delay of 2-3 seconds was used between each hole being drilled. The delay allowed for the polypropylene to cool down, and thus reduced the hole's chances of being filled-in or blocked by its neighbour, when the latter was being drilled.

3.4.3. Laser Processing Results

Better results occurred when a lens with a focal length of 50 mm was used on the 500 μm thick samples. The lens creates a beam width of 5.2 μm and a depth of focus of 55.2 μm. Different powers, pulse widths and duty cycles were tried in order to find an optimum setting. Figure 3-8 shows the black polypropylene with a 50 mm focal length lens.

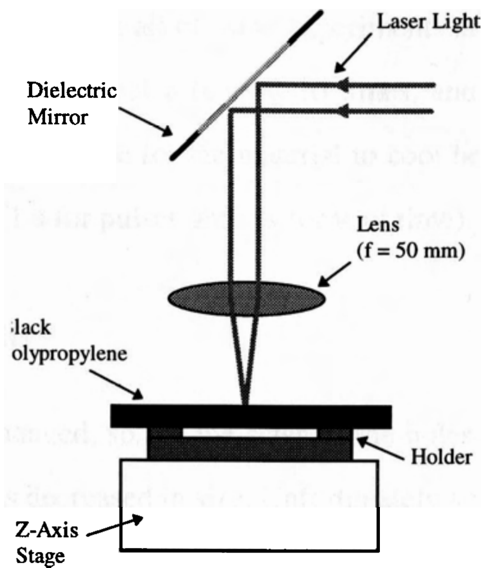

Figure 3-8: Polypropylene with a 50 mm focal length lens

3.4.3.1. Threshold Power

The minimum laser power required for hole drilling, the threshold power, changes with the pulse durations (width) and the duty cycle. As the width increases, the threshold power decreases, and the same is true for an increase in duty cycle.

Table 3-1 below shows the threshold power for the 500 μm thick black polypropylene samples, with the results for the best hole diameters and center to center hole spacing shown in bold.

Table 3-1: Threshold power in Watts

	Pulse Width				
Duty Cycle	500 ms	100 ms	10 ms	1 ms	0.1 ms
50 %	0.12 W	0.15 W	0.35 W	0.45 W	0.60 W
16.7 %	0.18 W	0.20 W	**0.40 W**	0.60 W	
9.1 %	0.23 W	**0.25 W**	**0.60 W**	0.90 W	
2.0 %	0.75 W	0.25 W	1.75 W		

The blank entries in Table 1 represent powers that are unsafe or inappropriate to be used in drilling. Too high a power may produce a hole that is not appropriate for the mask, such as holes greater than 200 microns, or irregularly shaped.

The number of pulses used in all of these experiments are based on a total time of 1 second. For example, a 100 ms pulse is used 10 times, and a 10 ms pulse, 100 times. Because of a two second wait time for the material to cool between holes, the number of holes per minute was 20 (1 s for pulses and 2 s for wait time).

3.4.3.2. Tabulated Results

As the parameters changed, so did the sizes of the holes. For a small pulse width or small duty cycle, the holes decreased in size. Unfortunately smaller pulses required higher power, and can result in power far too high to be used safely on the polypropylene. Such results can limit interspacing of holes and hole-size. Smaller pulses do not necessarily create smaller holes and the total thermal energy can be too low. Increasing the number of pulses can have a detrimental effect similar to too much power. A wide range of powers and pulse durations was explored to find the optimal holes. The criteria for the optimal holes for specific pulse widths and duty cycles are ones that offer the smallest hole diameters, the closest center to center hole spacing between neighbouring holes, and the lowest power. Table 3-2 shows the results of the best holes for different pulses and duty cycle. The blank entries are ones in which an optimum power could not be found and the bold entries are the best laser pulse parameters.

If the number of pulses are increased or decreased at the same power level, different hole characteristics are produced. A smaller pulse width and an increase in the number of pulses can produce better holes and interspacing. For example, a 10 ms pulse, with 100 pulses, and a laser power of 1.75 W produces 35 μm holes and 150 μm spacing. The result is the same as for 100 ms with 10 pulses with 0.3 W but uses a lower laser power. Thus the lower power result would be preferred in creating holes reducing the chance of deformed and incomplete holes.

Table 3-2: Hole and interspacing results

Pulse width (ms)	Duty Cycle (%)	Number of Pulses	Power (W)	Hole Diameter (μm)	Interspacing (μs)
500	50.0	2	0.15	55	250
500	16.7	2	0.20	45	200
500	9.1	2	0.25	42	200
500	2.0	2	0.75	45	200
500	1.0	2	1.20	52	200
100	50.0	10	0.15	35	200
100	14.3	10	0.20	32	175
100	**9.1**	**10**	**0.30**	**30**	**150**
100	**2.0**	**10**	**0.90**	**27**	**150**
100	**1.0**	**10**	**1.50**	**30**	**150**
10	50.0	100	0.35	60	250
10	16.7	100	0.50	45	200
10	9.1	100	0.65	40	200
10	**2.0**	**100**	**1.75**	**35**	**150**
10	1.0	100	Very High		
1	50.0	1000	0.50	72	250
1	16.7	1000	0.70	60	250
1	9.1	1000	0.90	60	250
1	2.0	1000	Very High		
1	1.0	1000			
0.1	50.0	10000	0.60	72	250
0.1	16.7	10000		60	250
0.1	9.1	10000		60	250
0.1	2.0	10000			
0.1	1.0	10000			

Table 3-3 shows the etch rate in microns per pulse for the optimum results. These values are much larger than identified in the literature, with an average etch rate of only 0.1 μm/pulse. The highest etch rate seen for the optimum results in table 3-3 were 50 μm/pulse.

Table 3-3: Etch rate of optimum results

Pulse width (ms)	Duty Cycle (%)	Number of Pulses	Etch Rate (μm/pulse)
100	9.1	10	50
100	2.0	10	50
100	1.0	10	50
10	2.0	100	5

3.4.3.3. Optimum Parameters

From table 3-2, choosing the lowest power and the smallest hole spacing as the optimal result was the 100 ms pulse with a 9.1 % duty cycle, 10 pulses, with power of 0.3 W, which produced 30 μm sized holes and 150 μm spacing. These values were used to create the masks for the proximity sensor. Figure 3-9 shows a cross sectional view of the hole. The entrance point shows a hole opening larger than 30 μm, but the hole tapers rapidly to its small dimension in the top 60 μm.

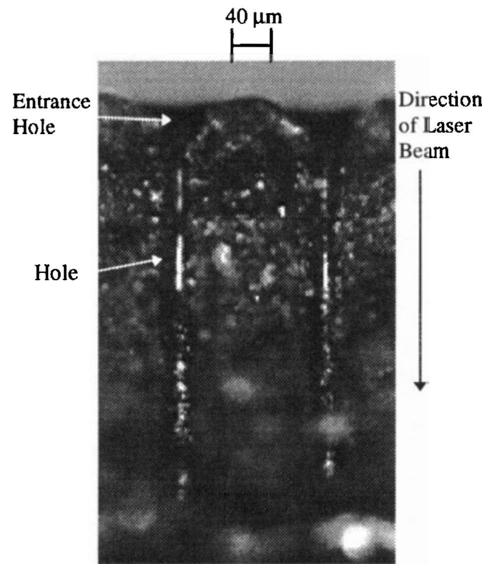

Figure 3-9: Cross sectional view of a hole

3.4.3.4 Mask Density

Two different types of masks were created for each CCD in order to make good use of the pixel spacing. The pixel spacing and number of holes are shown in Table 3-4. The interspacing is based on the best multiple of pixel size near 150 μm.

Table 3-4: Grid density for CCDs

	Number of Pixels	Interspacing	Number of Holes
TC245			
Horizontal	252	153	41
Vertical	242	157.6	29
TC211			
Horizontal	165	144	18
Vertical	192	151.25	17

One of the hole spacings created for these masks is smaller than the values in table 3-2 because of slight optimization. Also, the results are such that not all the holes in the array are completely through the material. Thus these masks are created but the probability of success for all the holes to be clear is lower than in the case with larger spacing.

3.4.4 Double Multilayer Mask

In making double multilayer using the black polypropylene, the main trick was the drilling of alignment holes at each corner. The two types of double masks created were just a simple double layer and two masks separated by a shim, which was created from polypropylene. Extra alignment holes were created 500 μm from each corner with the Argon ion laser at the time of mask fabrication. The sizes of the holes were large around 100-200 μm. Figure 3-10 shows an example of the holes.

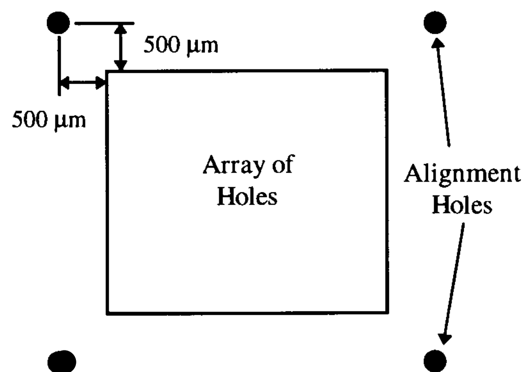

Figure 3-10: Alignment holes for double mask

Two identical masks with alignment holes were created in polypropylene. The two masks were placed on top of each other. Pins were inserted into the alignment holes to align the two masks. A minimum of three pins were used in joining the masks. The pins were #000 insect pins, which have a diameter around 250 μm. Each hole was first expanded by inserting the pin then pulling it out. The pins were placed one at a time, in the first mask, then the second mask had the pins inserted into it one at a time as well.

The masks were then moved together. The edges of the masks were melted with a soldering iron to bond them. Because the melting point of polypropylene is low, the soldering iron had sufficient temperature to melt the edges. Once cooled, the two mask were essentially one complete unit. The pins were then removed, and the edges furthered heated to remove excess material so that the double mask would fit on the surface of the CCD. For a double mask with a shim, the same technique was used, except that a shim made of polypropylene was used between the layer (See Figure 3-11). The shim was of the same thickness and consisted of a square with the center removed. Alignment holes were also located on the shim. Figure 3-11 shows a cross-sectional view of the double mask with and without the shim, using the alignment pins.

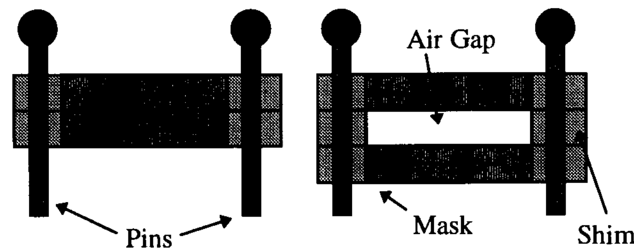

Figure 3-11: Alignment of masks

The technique of using pins for alignment was only successful for early work in the 500 μm thick polypropylene. The hole spacing of 300 μm and hole diameter of 63 μm sample discussed in section 3.4.2 were successful. For the optimized results with 150 μm hole spacing, the alignment was not accurate enough such that half the holes would become blocked. For the 300 μm samples, the holes were large enough that even a 15-30 μm misalignment meant that half the hole would align. For the 150 μm spacing, this error can result in one half to all the area of a hole to be covered. The use of double masking was proved for the low density mask, but future work has to include a better alignment technique as mentioned in section 7.5.

3.5 Gluing

The final step in sensor fabrication was the insertion of the mask in the CCD array and its alignment to the pixels. Once the glass cover was removed from the ceramic package of the CCD, the mask was placed directly on top of the CCD surface. For the smaller TC211, a probe was used to hold down the center of the mask during gluing. Unfortunately this technique did not work too well because of the movement of the mask during gluing and resulted in the next technique to be used. Three of the corners of the mask were held in placed by using (chip) probes. The micromanipulators allow X, Y, and Z positioning with the resolution of a few microns. The probes were moved slowly such that the mask's position on the surface could be changed. While the mask was moved, an image from the CCD was displayed so the changes in alignment could be observed. The mask was moved such that the CCD surface was properly covered, and to make sure little rotation existed relative to the horizontal direction of the CCD array. The mask then had quick drying epoxy (Epoxy-Path, 608 Clear) placed on the edges, usually the corners to permanently hold it down onto the CCD. The probes were kept in position for twenty-four hours to guarantee proper bonding. The image in Figure 3-12, taken by the CCD, is a few rows of mask after being placed on the CCD. A slight rotation exists relative to the row, and thus must be compensated for when parsing the image.

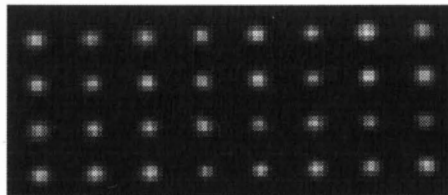

Figure 3-12: Image of rows of holes in TC211 mask

3.6 Summary

This chapter has described the manufacturing of the proximity sensor. Shown was the laser and control equipment used to construct the mask. The TC211 and TC245 were the CCDs used in the construction of the sensor. The boards used to obtain an image from the CCDs were put together using an instruction book. The laser produced many different results in hole quality and spacing, but the final parameters chosen resulted in a hole diameter of 30 μm with 100 μm spacing for a laser power of 0.30 Watts, 100 ms pulse width, 9.1 percent duty cycle and 10 pulses. A number of masks were created for the sensor, each a different size to optimize the pixel sizes and location. Double multilayer masking was achieved on earlier masks, but with no success with the optimized masks. The masks were then finally glued to the surface of the CCDs, which made use of probes to keep the assembly steady during drying and to hold the mask down.

CHAPTER 4: LENSLESS IMAGING

As mentioned in section 2.2, the proximity sensor has the capability of imaging at close range. This sensor is different from other systems in that no lens is needed to perform the imaging, making it small. Some tests with simple images were performed with the sensor.

To better understand the functioning of the sensor, formulas and simulations were created in Matlab and C code. The simulations done in this chapter are based on the formulas in this chapter and those given in section 2.2.

4.1 Theory of Operation and Simulation

In order to properly understand the function of the sensor, formulas and simulations were performed which dealt with a point source of light. From equation (2-2), the condition is given for when the light from an emitting spot no longer illuminates the sensor.

$$\text{(2-2)} \quad \frac{Z}{x} \leq \frac{t}{D}$$

When the point source is directly over a hole, the whole detector is illuminated because the light is scattered. As the spot source moves away in the horizontal direction, the mask begins to shadow the detector. The shadowing will cover a percentage of the area of the circular detector. Another way of viewing the shadowing effect is the intersection of two circles. Figure 4-1 demonstrates the idea. One circle is the circular detector under the mask hole, and the other is the projected circle of light from the circular opening on top of the mask seen at the detector surface.

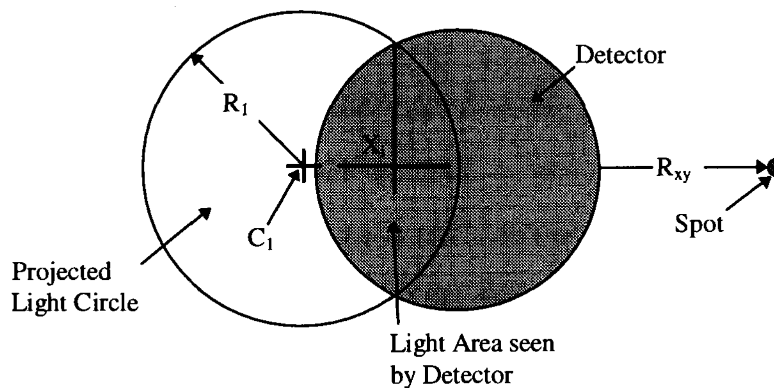

Figure 4-1: Intersection of light circle and detector

Appendix C shows that the projected light is a circle. Essentially, the cone of light created from the point source enters the top hole of the mask as a circle, and since the bottom of the detector surface is at the same angle (parallel to) as the opening at the top, a circle is projected. The area of intersection of the light circle and the detector surface is the amount of light falling upon the sensor. The area outside the detector circle would not produce a signal, and would be blocked by the walls of the hole. The radius of the detector is known, since it is the one half the hole diameter of the mask. The radius of the projected light circle is in formula (4-1).

(4-1) $$R_I = \left(\frac{t}{Z} + 1\right)\frac{D}{2}$$

The value of R_l is the radius of the projected light circle, D is the diameter of the hole, t is the thickness of the mask, and Z is the distance from the spot to the top of the mask. As the vertical distance (Z) approaches infinity, the light circle approaches the radius of the hole opening (0.5D), which makes sense because the scattered light rays become parallel. The center of the light circle is C_l in formula (4-2), where the origin is the center of the detector circle.

$$(4\text{-}2) \quad C_l = \left(\frac{D}{2} + R_{xy}\right)\frac{t}{Z}$$

Only one value is needed for the center because the formula has no radial dependence. Essentially it is the direction along the central axis of the detector. The value of R_{xy} is the distance from the edge of the detector to the point source on the X-Y plane where the path would go through the center of the detector.

The point along the central axis where the two circles intersect is in equation (4-3).

$$(4\text{-}3) \quad Xi = \frac{\left[\frac{D^2}{4} - R_l^{\,2} + C_l^{\,2}\right]}{2C_l}$$

The percentage area of the circular detector exposed to light is in equation (4-4).

$$(4\text{-}4) \quad A = \frac{\left(f(R_l, C_l - X_i) + f(0.5D, X_i)\right)}{\pi\left(\frac{D}{2}\right)^2}$$

The function f(u,v) is shown in equation (4-5).

$$(4\text{-}5) \quad f(u,v) = u^2\cos^{-1}\left(\frac{v}{u}\right) - v\left(u^2 - v^2\right)^{\frac{1}{2}}$$

As can be seen from Figure 4-1, it is possible that the projected light circle and the detector do not intersect. At this point, the equations (4-4) and (4-5) would produce imaginary values. Thus formula (4-4) is valid only for a certain range, that being the

distance when shadowing starts and the detector is in total shadowing. If the light source is between the edges of the two holes, the total light area exposed is 100 %, and would result in an infinite number of points that intersect the circles instead of two. The range of R_{xy} for equation (4-4) is shown in (4-6).

$$(4\text{-}6) \quad 0 < R_{xy} < \frac{ZD}{t}$$

The complete calculations for the percentage area of light exposed on the detector is shown in greater detail in Appendix C.

The light intensity (I) of the point source at the surface falls as one over the square of the distance from the center of the detector to the light source point which changes little over the circle. To calculate the total intensity, the intensity I is multiplied by the percentage area A covered by light. The formula is shown in equation (4-7).

$$(4\text{-}7) \quad I_{total} = I \times A$$

The formula assumes that the light intensity is close to being the same for the whole surface of the detector. Even though a change in intensity exists from one end of a detector to the other because of a change in total distance, the values are quite small. By doing a calculation where the light source is over the center of the detector (R) and the addition of the radius of the hole (ΔX) which is perpendicular to the direction over the detector, equation (4-8) shows the change in the square of the distance. As can be seen from (4-8), the effect of ΔX is small compared to large distances (R).

$$(4\text{-}8) \quad \frac{\left(R^2 + \Delta X^2\right)}{R^2} = 1 + \left(\frac{\Delta X}{R}\right)^2$$

Because the simulations usually work with distances around 1000 μm, and the holes created are only 30 μm, the change in the square of distance from the center to the edge of

the hole (±15 μm) creates an increase of only 1.5%, which results in the edge of the detector being only 99.97% of the value in the center of the detector.

These formulas are used for showing relative changes in light intensity and would be normalized to some value such as the largest intensity. The increase in area for hole sizes were not compensated by these formulas, since it is assumed that the same sized hole would be used. To take into account the extra area exposed from a larger hole, the formula in (4-7) would only need to be multiplied by area, or just the square of the diameter (the difference being out by $\pi/4$ which would be a multiplication factor on the results).

Simulations can be performed using the equations given to determine the response of an array of detectors or just one. Figure 4-2 is the graph of a simulation of an ideal point source of light that passes from the left to right over the center of the sensor. This light sweep produces a view of the response of one detector with the shadowing taking effect.

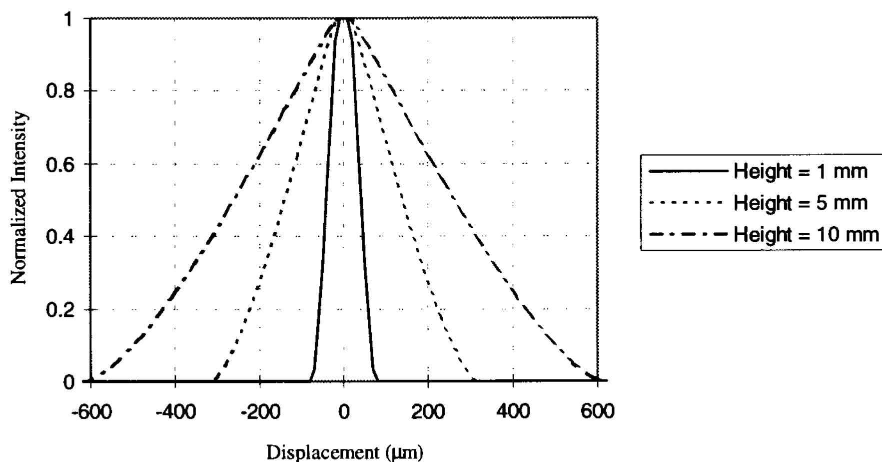

Figure 4-2: Simulation results of a point source of light moving across detector with 30 μm holes and an aspect ratio of 16.7

The graph is a simulation where the spot of light is at different heights from the surface of the mask. The path of light passes over the center of the detector (displacement of zero). The shadowing of the light does not take effect until the light source is over the

edge (aligned in the X-Y plane) of the hole. When the spot is within the hole boundaries, there is no attenuation except for the $1/R^2$ law. The intensity from the edge of the hole (15 μm) to the cut off region ($I = 0$), is attenuated somewhat linearly by the shadowing.

Appendix D contains the C-code of the functions for simulating one detector. These functions are used to create simulations, such as the one shown in the graph, where a spot position is changed as a variable.

4.2 Set-up for Lensless Imaging

To test the lensless imaging of the sensor, a checkerboard pattern was viewed at various heights by the sensor. The checkerboard pattern were squares of 1 mm on the side. The test set-up made use of a light source, a micrometer and the test pattern which is shown in Figure 4-3. The micrometer was moved in well defined increments to slowly increase the height from the sensor. The light source was pulsed and shone above the checkerboard pattern. The checkerboard pattern allowed light to diffuse through, and was the substitute for projecting light between the sensor and the pattern. The pattern was used to test the sensor's capability to image objects at varying heights from the surface of the mask. As the pattern moves further away, the more the image becomes blurry. Ideally an object would be illuminated from underneath, but this set-up was easier to implement.

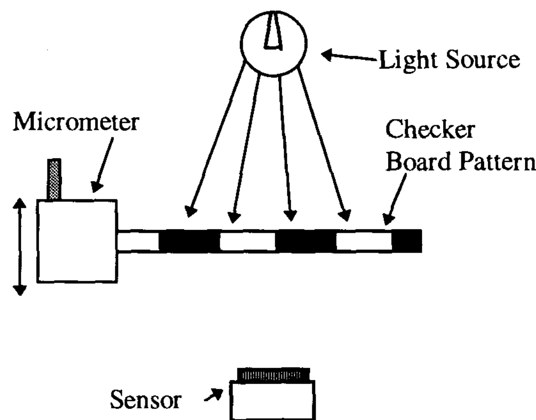

Figure 4-3: Lensless imaging set-up

4.3 Imaging from High Density Sensor

Imaging tests were conducted on the proximity sensor that contained the high density masks discussed in section 3.4.3.4 consisting of 30 μm holes spaced at 150 μm in 500 μm thick polypropylene, placed on the TC211. The test set-up discussed in section 4.2 was used. All the pictures in this section used a 0.3 second pulsed light source for a 2 second camera integration time. A dark current image was also subtracted from each the pictures.

The first image shown in Figure 4-4 is the checkerboard pattern at a height of 484 μm from the surface of the mask. The image shows the picture taken from the TC211, and the small holes can be seen. Some of the holes are bright while others are dim or non-existent. The checkerboard pattern can be seen from these holes. At this point the image was about one mask thickness from the surface of the mask. Using equation (2-4) the viewing size of each hole was (D = 30 μm, t = 500 μm, Z=484 μm) 88 μm, which left a space of approximately 62 μm between holes that was not being observed.

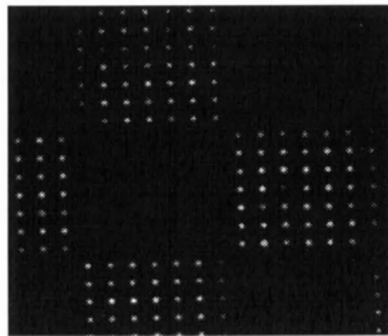

Figure 4-4: 1 mm checkerboard pattern at a height of 484 μm with TC211, 30 μm holes, 16.7 aspect ratio and 150 μm hole spacing

Figure 4-5 shows the same picture as in Figure 4-4, but is parsed with the code shown in Appendix A. Each pixel (square) is the light gathering of one hole. Thus, a virtual detector is created under each hole. The code in Appendix A also reads the original image data files which contain data for 192x165 pixels. The parsed image only contains 16x17 pixels (one pixel per hole). The checkerboard can clearly be seen in the

image of Figure 4-5. All further pictures from the high density mask will be shown in this section as parsed images.

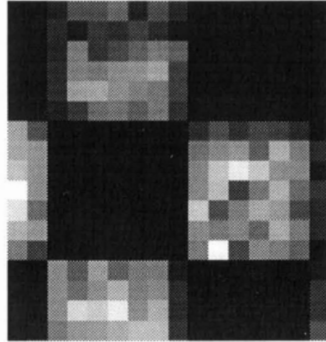

Figure 4-5: Parsed image of 1 mm checkerboard pattern at a height of 484 μm with TC211, 30 μm holes, 16.7 aspect ratio and 150 μm hole spacing

Using equation (2-5), the height at which acceptance cones intersect between two neighbouring holes is 1000 μm (using p = 150 μm, which is an estimate since two different hole spacings were used, 144 μm and 151.25 μm). The image in Figure 4-6 is the same pattern but at a height of 1119 μm (2.2 mask thicknesses) from the surface of the mask. As can be seen, the image is still sharp and well defined as expected from the calculations. At this point, the acceptance cones overlap only about 14.3 μm.

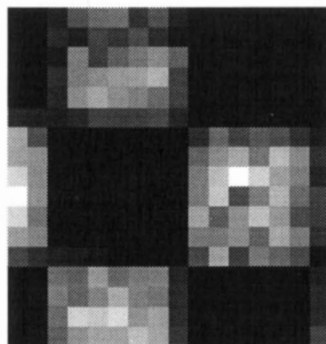

Figure 4-6: 1 mm checkerboard pattern at a height of 1119 μm with TC211, 30 μm holes, 16.7 aspect ratio and 150 μm hole spacing

The right edge of the images so far contain a faint line which is the continuation of the checker image out of the range of the sensor. The checkerboard pattern is not a constant intensities for the white areas as would be expected. The images are uncalibrated

and are not compensated for these anomalies which could be caused by the sensitivity of the detectors and differing hole diameters.

The checkerboard image was clearer than expected at larger heights. The image in Figure 4-7 is the checkerboard pattern at a height of 2389 μm (4.8 mask thicknesses) from the surface of the mask. At this height, the size of the viewing circle of each hole is 317 μm, and thus each hole will be viewing area seen by its neighbour.

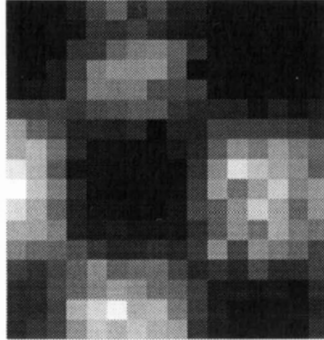

Figure 4-7: 1 mm checkerboard pattern at a height of 2389 μm with TC211, 30 μm holes, 16.7 aspect ratio and 150 μm hole spacing

Even at very large distances, the sensor is still able to image some of the checkerboard pattern. Figure 4-8 shows the image of the checkerboard pattern at a height of 6120 μm (12.2 mask thicknesses) from the surface of the mask. As can be seen, the image is still somewhat distinguishable as a checkerboard pattern. The light area of the checkerboard pattern is merging with the dark area because of the blurring caused by the distance. At this height the size of the viewing circle of each hole is 764 μm in diameter, which results in each hole overlapping in image area of two neighbours on each side.

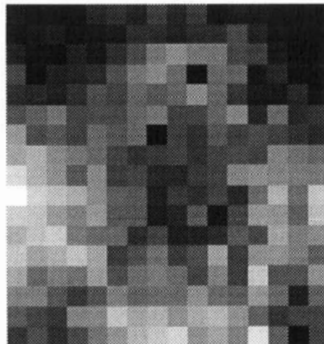

Figure 4-8: Checkerboard pattern at a height of 6120 μm with TC211, 30 μm holes, 16.7 aspect ratio and 150 μm hole spacing

An image filter was used to produce a clearer image because of the blurring. The sensor does not have the capability of seeing very much detail of an object it views, which is inherent in the way the sensor collects light over a region. Thus only low detail will be seen with much clarity and is the reason why a low pass filter was used. A 3x3 averaging filter, as shown in equation (4-9), was used on the image in Figure 4-8. The filter is also known as neighborhood averaging[18].

$$\text{(4-9)} \quad \text{filter} = \begin{bmatrix} 1 & 1 & 1 \\ 1 & 1 & 1 \\ 1 & 1 & 1 \end{bmatrix} \times \frac{1}{9}$$

Figure 4-9 shows the same image as Figure 4-8 but with the 3x3 averaging filter applied and a gamma correction of 0.8, which allows values at the lower end of the gray scale to have less difference in brightness. The image was gamma corrected after the low pass filtering. The checkerboard image is more discernible after the filter has removed the high frequency image noise. The areas in which the pixels seem overly bright were reduced by this filter. The filter could be used on all images from this sensor, thus improving the viewing capability especially at large distances from the sensor's mask surface.

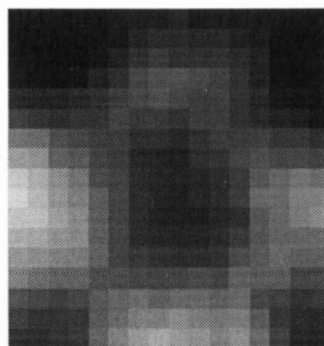

Figure 4-9: Image correction of checkerboard pattern at a height of 6120 μm with TC211, 30 μm holes, 16.7 aspect ratio and 150 μm hole spacing

Some of the noise seen in the images could be caused by pixels that are overly sensitive to light, either from a higher quantum efficiency or larger holes. Another source of error could be caused by the image itself. The quality of the image is sharp to only about 40-80 μm, and does not block all light in the black area. The image was not perfectly aligned to the rows and columns of the mask, and thus a rotation of the image in the plane parallel to the mask would create small corners and shapes that would be difficult to see at large distances.

In addition to using a filter, a calibration should be completed on the sensor that compensates for the differing sensitivities of the photodetectors, and the changes in hole diameter. The calibration could be a multiplication matrix based on an evenly illuminated white image taken by the sensor. With this calibration, different sensitivities for each hole could be compensated.

As seen from the figures in this section, the sensor does provide a simple lensless imaging system. Even at heights many times larger than the mask thickness, the images are still distinguishable as the original checkerboard pattern.

4.4 Simulation of High Density Mask Viewing Checkerboard Pattern

A simulation was written based on the functions in Appendix D, of the sensor viewing the checkerboard pattern image at various heights. The pattern was represented by a light square of size 996 μm, with a light spot at every three microns. Appendix E shows the code for this simulation. Essentially the square was an array of light points. The values in the simulation were close enough to the approximate 1 mm size in the experiments in section 4.3. The size used in the simulation was of a multiple of 3 and also could be centered (i.e. a value that represents the true center of the square). These squares were laid out in the simulation in a similar manner as the actual checkerboard pattern. The simulation was then tried at heights similar to ones in section 4.3.

The first image in Figure 4-10 is at a height of 500 μm or 1 mask thickness. The image is definitely clear. The image seems more even in the light level than the data.

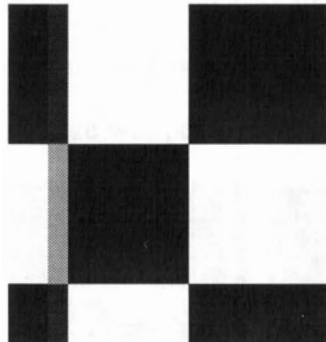

Figure 4-10: Simulation of checkerboard pattern at a height of 500 μm with 30 μm holes, 16.7 aspect ratio and 150 μm hole spacing

The images in Figure 4-11 and 4-12 are at heights of 1100 and 2400 μm respectively. As can be seen, the images are more sharp and clear than the actual data. One reason is that the light source for the experiments was not evenly illuminating the checkerboard image.

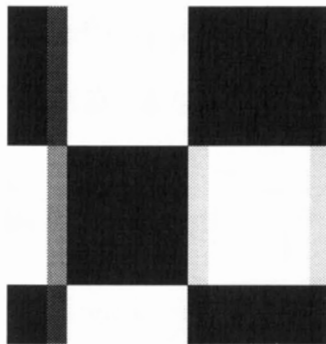

Figure 4-11: Simulation of checkerboard pattern at a height of 1100 μm with 30 μm holes, 16.7 aspect ratio and 150 μm hole spacing

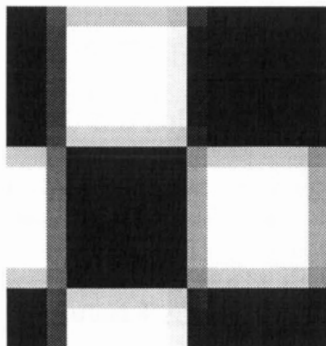

Figure 4-12: Simulation of checkerboard pattern at a height of 2400 μm with 30 μm holes, 16.7 aspect ratio and 150 μm hole spacing

The final simulation of a height of 6100 μm is shown in Figure 4-13. The image is less blurry than the data. Again, the simulation was the ideal case where the light was evenly illuminating the image, no light was passing through the dark area, all pixels had the same light sensitivity and the image was perfectly aligned with the sensor.

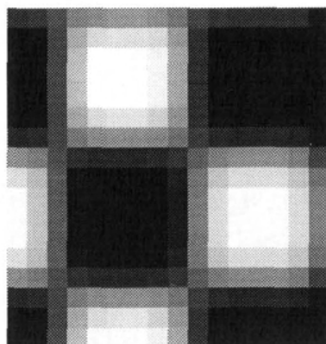

Figure 4-13: Simulation of checkerboard pattern at a height of 6100 μm with 30 μm holes, 16.7 aspect ratio and 150 μm hole spacing

Although the simulations shows a better image should occur at the different heights, it does indicate the noise associated with the original images. Still, the sensor was working similar to the simulations for the heights around 1-3 mask thicknesses.

4.5 Imaging from Double Mask

Imaging was tested on a double mask with a shim like the one discussed in section 3.4.4 with 63 μm holes with 300 μm spacing in 500 μm thick polypropylene. The double mask consists of two identical masks with a shim in the middle. The masks were aligned properly. This sensor was one of the earlier prototypes, and no imaging has been performed on double masks with 150 μm hole spacing, since the current technique does not seem to work with them. The resulting aspect ratio of the double mask was 23.8. The CCD array used for the sensor was the TC211. The pictures in this section used a 2 sec integration time and a 1.5 sec light pulse. Because this sensor was an early prototype, no

parsing of the images was performed, and these were the only experiments performed on this sensor.

The picture in Figure 4-14 is the checkerboard pattern at a height of 496 μm (≈1 mask thickness) from the surface of the mask. Because of the low density of these holes, there is a lack of detail from the mask. At this height the size of the viewing circle, using equation (2-4), is 105 μm, which leaves about 195 μm between holes that is unobserved.

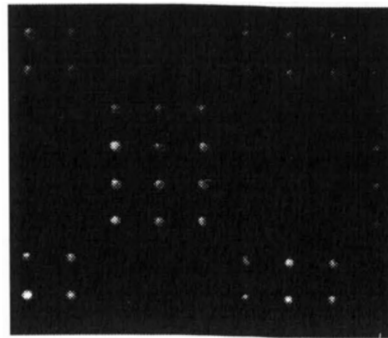

Figure 4-14: Double mask with 1 mm checkerboard pattern at a height of 496 μm with TC211, 30 μm holes, 7.9 aspect ratio and 300 μm hole spacing

Because of the larger apparent thickness and a wider spacing between the holes, the image can be seen further away. The height at which the viewing circles intersects neighbouring holes is 2821 μm. At a height of 5001 μm (10 mask thicknesses), the size of the viewing circle is 483 μm, and they overlap by 183 μm. The checkerboard image is still visible as can be seen in Figure 4-15.

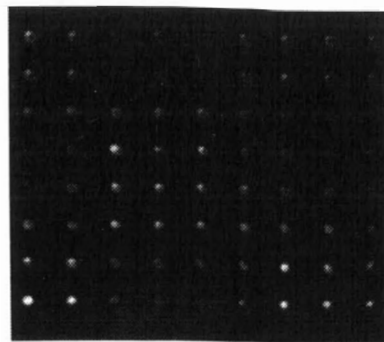

Figure 4-15: Double mask with 1 mm checkerboard pattern at a height of 5001 μm with TC211, 30 μm holes, 7.9 aspect ratio and 300 μm hole spacing

The picture in Figure 4-16 is the checkerboard pattern at a height of 7997 μm. The size of the viewing circle is 735 μm, and even though they overlap, the checkerboard pattern is still discernible.

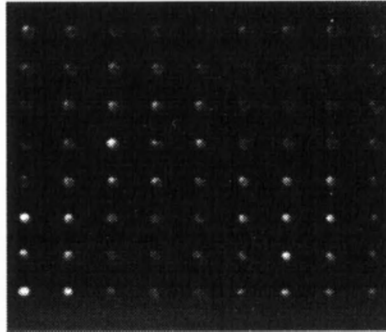

Figure 4-16: Double mask with 1 mm checkerboard pattern at a height of 7997 μm with TC211, 30 μm holes, 7.9 aspect ratio and 300 μm hole spacing

So at large heights the checkerboard pattern is still imaged by the sensor. The images in this sensor are from an early prototype but do show that imaging worked and is improved by using a double mask configuration.

4.6 Summary

A checkerboard image was used to test the vision capability of the proximity detector. Even though the simulations produced better results than the experiments, the experiments did show that viewing the image was possible at heights equaling twelve times the thickness of the mask. Noise and varying intensities caused by differing hole sizes and hole diameters were probably the major source of error for the sensor and using a simple averaging filter improved the quality. Imaging was also performed on a double mask, showing that the mask was still capable of imaging with this configuration.

CHAPTER 5: PROXIMITY MEASUREMENT

The accuracy of measuring height by the sensor is one the most important aspects of its operation. Multiple tests were performed on the sensor, which makes use of the TC211, to determine the accuracy of proximity measurements. This chapter contains the discussion of the formulas and the simulations of the gaussian beam. As well, the experimental results and a discussion of the errors are presented.

5.1 Simulation of Gaussian Beam

The measurement of distance makes use of a gaussian laser spot as opposed to an ideal point source of light. As mentioned, the intensities seen by the detector will differ as well as the intensity seen by one detector as a laser spot moves across it. For Figure 4-2 in section 4.1, an ideal light spot was simulated moving over the center of one detector. To simulate a laser spot a slightly different approach was used. The gaussian laser spot can be thought of as an infinite number of spots with intensity that varies with position. Equation (5-1) shows the change in intensity from the laser spot center, where r is the distance from the center of the beam and w is the $1/e^2$ beam radius.

$$(5\text{-}1) \quad I(r) = \exp\left(\frac{-2r^2}{w^2}\right)$$

Instead of calculating an infinite number of points, a finite number was used. A range of 804 by 804 µm was simulated for a beam radius ($1/e^2$) of 200 µm. Every 3 µm was a simulated point source, with an intensity matching the formula for equation (5-1). The total number of points calculated for one laser spot was 71824. The code for this simulation is in Appendix F.

The graph shown in Figure 5-1 is a simulation of a 200 µm beam as it moves across the center of a detector with the laser spot at varying heights from the surface of the mask, which has 30 µm holes and an aspect ration of 16.7. Instead of a $1/e^2$ radius of 200 µm, the new value at a height of 1 mm is 207 µm, thus the beam has the radius is expanded by only 7 µm.

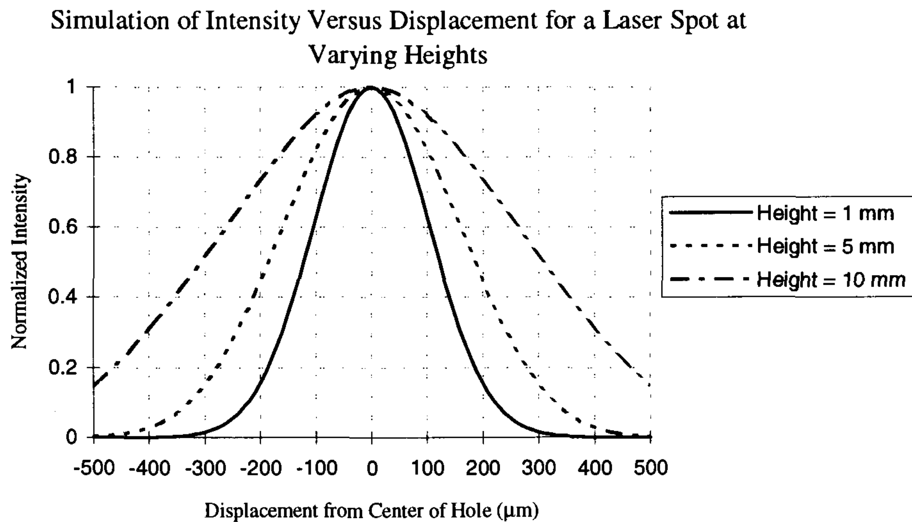

Figure 5-1: Simulation results of a laser spot moving across detector with 30 µm holes, an aspect ratio of 16.7 at a varying heights

For a proximity sensor with a specific spacing between hole centers, one only has to look on the graph in Figure 5-1. For the TC211, the spacing in one direction is 144 µm, thus to see the values at each hole (assuming the beam center is over one sensor), the values at multiples of 144 µm (-288, -144, 0, ..) only need be looked at. To determine the

intensity of each hole with the spot moved 10 μm to the right from the a hole center use the intensity at multiples of 144 μm minus 10 μm (-298, -157,-10,...).

5.2 Center of Gaussian

The proximity sensor does not need any formula to find the center of the gaussian spot. As seen from Figure 5-1, the brightest detector is the location of the center of the spot. Unfortunately the accuracy of this method is only plus or minus one half of the hole spacing. The detector with the largest intensity is a rounding off of location, in which it will be the brightest if the spot is within half the detector spacing. For the sensor created this means an error of ±75 μm on the X-Y plane, and the error would be multiplied by the tan(θ) for the error in the height measurement.

A better way to determine the center of the beam is to not only use the detector with the largest intensity, but to also analyze the neighbouring holes around this detector. A labeling convention is to name the detector (hole) with the largest intensity value maximum (max.). The holes before and after this location are named minimum (min.) and middle (mid.), where minimum is the smallest signal of the three, and the middle value is between the minimum and maximum value. By using only three holes, better accuracy can be obtained. The full gaussian is not seen by the sensor like the graph in Figure 5-1, because of the distance between holes. The gaussian becomes sampled at specific distances (144 μm for the simulation), and looks somewhat like a triangular distribution over position. If the beam was instead a triangle, the center could easily be calculated by drawing a line from the min. point to the max. point, and then drawing a line with the same slope but negative at the mid. point. The point where the two lines intersect would be the center. The diagram in Figure 5-2 demonstrates this line intersection.

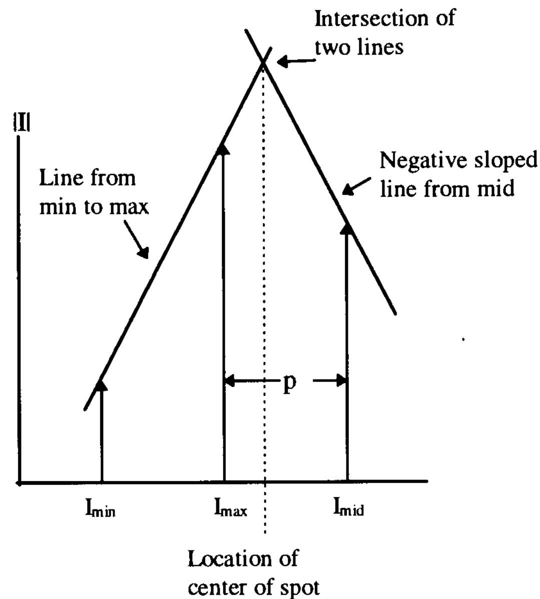

Figure 5-2: Intersection of lines for center of laser spot

The equation for this line intersection is shown in (5-2). The values are the same as shown in Figure 5-2. The formula is multiplied by p which is the pitch or the spacing between hole centers.

$$\text{(5-2)} \qquad \Delta x = \frac{(I_{mid} - I_{min})}{2(I_{max} - I_{min})} p$$

Even though the equation (5-2) assumes a triangular spot, it does produce zero error for two specific positions for the gaussian laser spot. Thus, the equation is not just for a triangular spot, but the formula meets two conditions in the position of the laser spot. The first condition is where the laser spot is in the middle of the max. detector. At this point the intensities of both mid. and min. are equal. Figure 5-3 is a graph showing the three intensities based on the data from Figure 5-1 at a height of 1 mm. The center to center hole spacing is assumed to be 144 μm. In this case, the spot is in the center of the max. detector. By knowing that min. and mid. are equal, it can be determined that the spot is in the center.

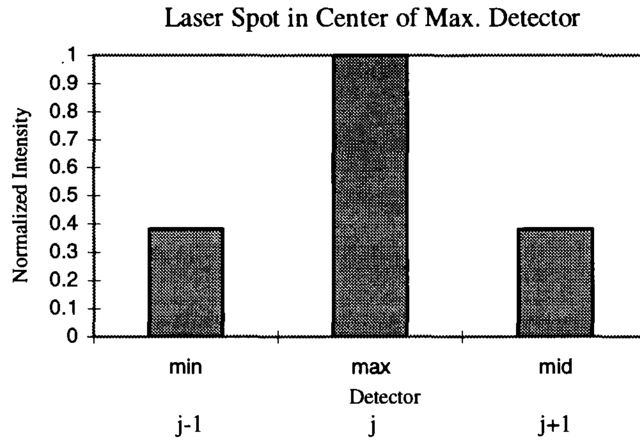

Figure 5-3: Simulation of laser spot in center of max. detector assuming 144 μm hole spacing

The second condition is where the spot is half way between the max. and the mid. detector and is also at this point that the maximum error occurs. The position based on the brightest spot will be either the max. or the mid. detector. From the graph in Figure 5-4, the simulation shows the max. and mid. values are equal.

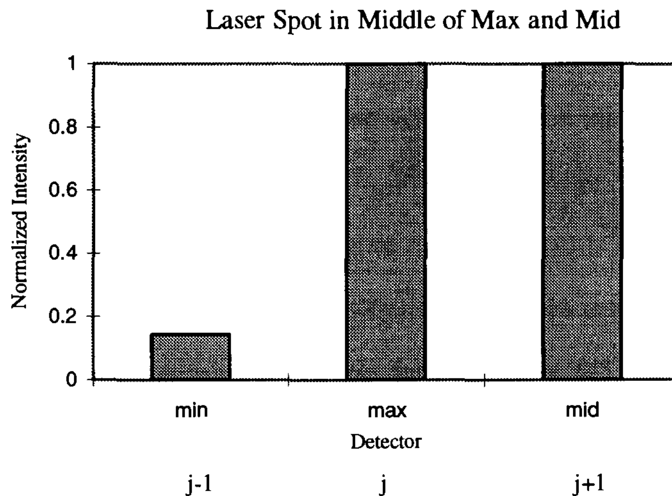

Figure 5-4: Simulation of laser spot in middle of max. and min. detector assuming 144 μm hole spacing

Therefore whenever the two are equal, the spot is in the middle. Deciding which value becomes the max. and mid. values depends on the algorithm used. If the condition of maximum is only when the value is greater, then the first detector found will be the maximum. Even if the mid. and max. where reversed, the min. value would be to the right of the detector, but would still have the same value.

For the case of the spot in the middle of the two detectors, the min. value does not matter, as the position is known when mid. and max. are equal. Equation (5-2) creates a value of one half the pitch when the two are equal which is the correct value of the position and no error results. Thus equation (5-2) meets both conditions mentioned, when the spot is in the center of the max. detector, and directly in-between the max. and the mid.

The equation (5-2) reduces the error to zero for the condition of the spot being in the middle of the max. and mid. detectors and produces a value of zero when the spot is directly over the max. detector. If the shape of the beam was triangular for intensity versus position, then the formula would produce zero error.

For the equation to work, the radius of the laser spot should be at least as large as the hole to hole spacing, such that the three detectors can see the laser spot when it is as close to the sensor as possible (a height of zero). Intensity should be measured by all three detectors when the spot is shifted from 0 to the mid way point. Thus, using a beam radius of 200 μm is fine since the spacing in the simulation is 144 μm, and for the real sensors around 150 μm. To use equation (5-2) for the data from the TC211, the value of the pitch was 144 μm or 151.25 μm depending on which direction (X or Y) on the sensor, either row or columns.

5.3 Angled Laser Experiments

The first set of tests for measuring the accuracy of the proximity made use of an angled laser beam projected on a light diffuser. Images were taken of the spot, and then data processing was performed to determine the X-Y position. The height was then calculated from the position and the angle of the laser. Although this set-up yielded some results, a better experiment was performed later as will be discussed in section 5.4.

5.3.1 Experimental Set-Up

The experimental set-up used an Argon ion laser as the light source but with the power decreased by neutral density filters. As shown in Figure 5-5, the beam approaches from the top of the light diffuser at an angle of 36.1 °. The beam approaching from the top is analogous to approaching from the bottom. A micrometer was used to raise and lower the light diffuser. Thus an experiment similar to an object moving in height from the sensor was achieved. As the diffuser moved up (ΔZ), the position of the spot moved by $\Delta x = \Delta Z/\tan(\theta)$ based on equation (2-1). The laser was manually blocked to act as a shuttering device for the laser beam. The relative intensities between the detectors (holes) at each sampling were the important values as opposed to the changes of intensities between samples. Thus small changes in the intensity values at each reading were not as important.

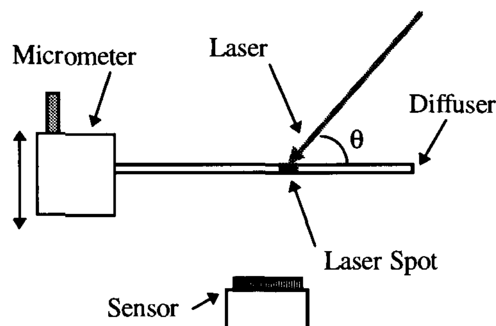

Figure 5-5: Set-up for angled laser experiments

The laser beam spot was reduced using a 25.4 cm lens, such that the apparent size of the spot at a height of 1531 µm from the sensor was 325 µm. Figure 5-6 shows a plot of this parsed image. The graph shows the data at each detector (hole) and the simulated values from an ideal gaussian beam with the radius of 325 µm. As can be seen, a good match has occurred. The C-code functions for parsing the data from the TC211 sensor is shown in Appendix A. The parsing parameters are specific to each sensor, because the position of the holes over the sensor changes when a new one is created. Also shown is a more generic parsing code in Appendix I, but is meant to be used in other experiments.

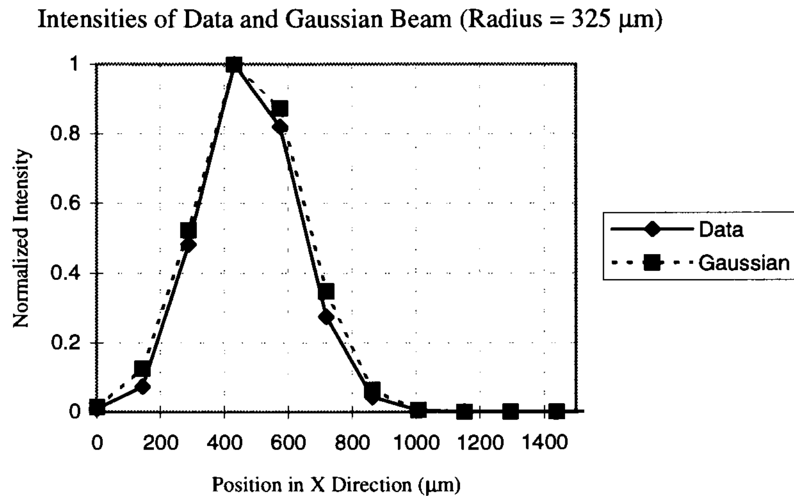

Figure 5-6: Comparison of data and ideal gaussian beam for laser angled experiment with TC211, 33 µm holes and 16.7 aspect ratio

The calculation of position was performed both in C code and Matlab functions. Appendix G shows the code calculating the position. The C code was written in Borland TurboC 2.0 in an MSDos environment.

5.3.2 Results

In several data sets the height (Z) was changed for a wide range of values to measure the accuracy of the proximity sensors. The graph in Figure 5-7 shows a plot of the measured height versus the actual height. The measured height is the height calculated from the X-Y position obtained from the data using the formula in equation (5-2). The graph shows heights starting at zero, but this represents the starting height of the diffuser which was 1532 μm. The graph shows relative height changes. The diffuser was moved in an upward direction in steps of 39.7 μm. The accuracy of the micropositioner was around 5 μm. The micropositioner had to be moved carefully in one direction to ensure that no backlash occurred. The graph shows a correlation that almost looks like a one to one correlation to the measured and actual height.

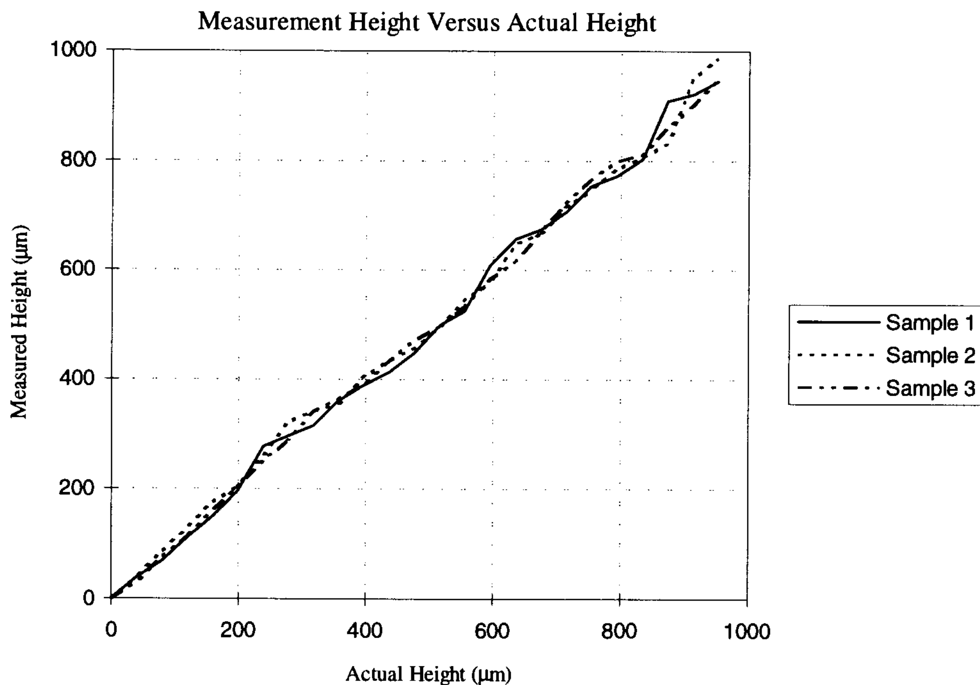

Figure 5-7: Graph of angled laser height measurements with TC211, 33 μm holes and 16.7 aspect ratio

The graph in Figure 5-8 shows a better representation of the data for seeing the position error between the real and measured values. The data was plotted as error versus height where the error is the difference between the measured and actual height. The graph shows that the experimental results have error ranges of 45.2 µm to -42.4 µm. The error is less with equation (5-2) than it would have been with the technique of using the detector with the largest intensity.

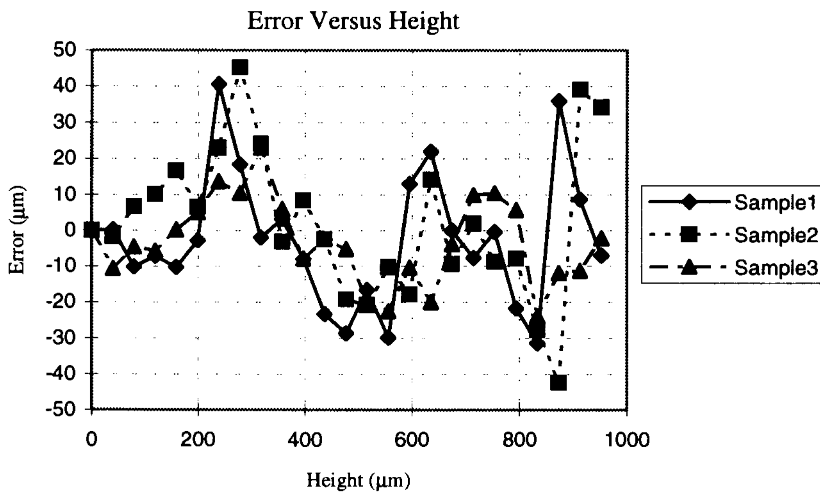

Figure 5-8: Graph of error for angled laser height measurements with TC211, 33 µm holes and 16.7 aspect ratio

Figure 5-9 shows the error from the three samples if only the highest signal detector was used.

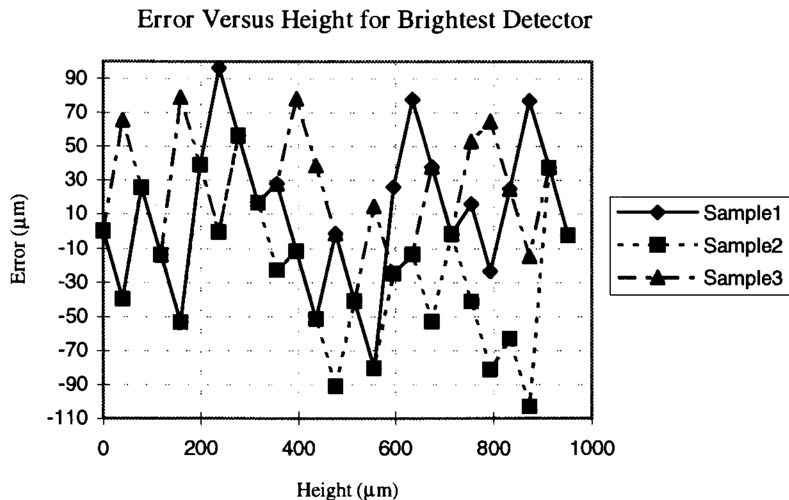

Figure 5-9: Graph of error using the brightest detector with TC211, 33 µm holes and 16.7 aspect ratio

In this case the position can only have values with multiples of 144 μm for one direction and 151.25 μm for the other direction. This technique results in an error range of 96 μm to -103 μm. Thus by using equation (5-2), the error is approximately reduced by half.

The accuracy at larger heights were experimented using this test set-up. The graph in Figure 5-10 is the error using equation (5-2) and the brightest spot technique for a starting height of 3502 μm from the surface of the mask. The change in height was in an upwards direction. The error range for values using the formulas was 43 μm to -80 μm, and for the brightest spot the error was 94 μm to -93 μm. The error is still less for the equation then the brightest spot, but not by as much as in Figures 5-8 and 5-9. The most probable result is a lessening in accuracy because the spot appears larger at this height. The error using the brightest detector did not change as compared to the last result, but the equation results in a larger error. The laser spot is further away and thus a spreading of the beam occurs and less accuracy is expected.

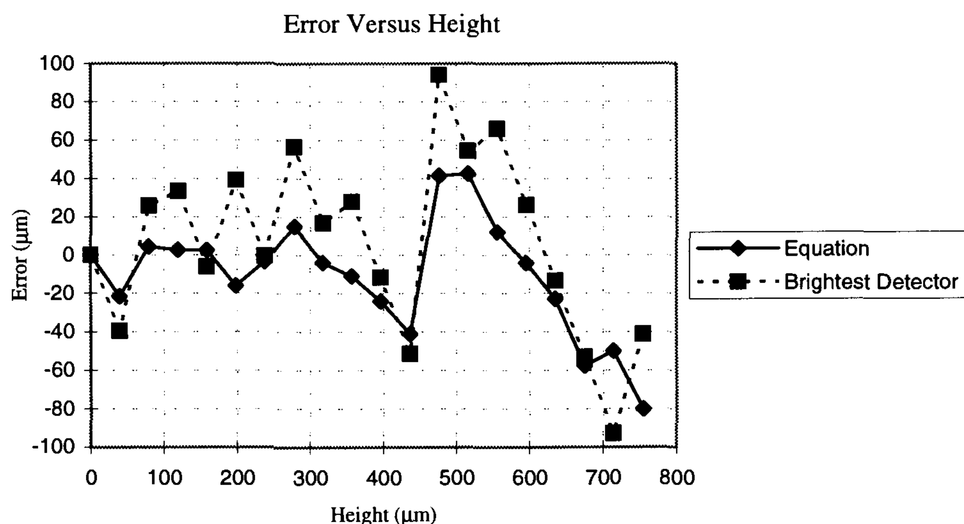

Figure 5-10: Graph of error for a starting height of 3502 μm with TC211, 33 μm holes and 16.7 aspect ratio

The errors were quite large for the results shown so far but for all the samples in Figure 5-8, the errors did follow very similar patterns which implied a constant error to

the experiments. The main source of error was the light diffuser itself. As the height was changed, the laser spot moved across the surface of the diffuser. Any changes in the distance between the surface and the mask due to anomalies in the surface would show up in the measurements. Even a change of 25 μm in surface texture would result in a fairly substantial change in the expected height. Because of the possibility of this error in these sets of experiments, a different set-up was used.

5.4 X-Y Table Laser Experiments

The angled spots of section 5.3's experiments do introduce larger errors due to the uncertainty in the Z position caused by the micropositioner, and the diffuser itself. To eliminate the error of the spot moving across the surface of the diffuser, a set-up was created in which the height was kept constant and the accuracy of the spot location was measured. As in section 5.3, images were taken of the spot, and then data processing was performed to determine the X-Y position of the spot over the sensor.

5.4.1 Experimental Set-Up

The proximity sensor measures height by knowing the position of the spot over the sensor, and knowing the angle of the laser. In fact the sensor is measuring the location on the X-Y plane of the laser spot. The better the sensor is able to measure the location of the spot, the more accurate the height. Thus, the experimental set-up shown in Figure 5-11 is such that the height from the laser spot on the diffuser to the sensor is kept constant. Instead of the diffuser moving up and down, the sensor is moved with the high accuracy X-Y table beneath the diffuser. The image from the sensor was then taken and the position of the spot over the sensor was then estimated. At all positions, the height is the same. Even if height anomalies exist in the surface of the diffuser, they will be the same for all measurements. Because only X-Y accuracy is being measured and not height, the

anomalies in height will only produce a constant change in beam shape. For the set-up in 5.3, any changes in height across the surface could be different in each height change, thus producing a random error. The set-up for these experiments were placed on the same X-Y table as shown in section 3.1. The Argon ion laser passed through the electro-optic shutter and thus could be pulsed. The laser was projected onto the light diffuser using lenses and the beam was normal to the diffuser. The sensor was placed on the Z-axis stage, which allowed measurements of the accuracy at different heights. The sensor surface was also aligned parallel to the diffuser.

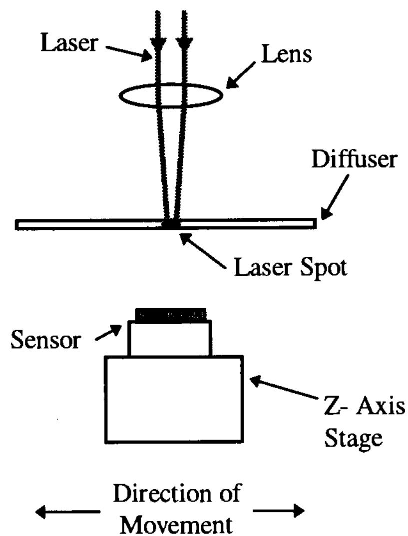

Figure 5-11: Set-up for X-Y table laser experiments

The movement of the sensor was such that only one direction in the X-Y plane was used. The movement was relative to the grid directions of the mask. In these experiments the direction of the 144 μm spaced holes was used. This direction would correspond to a movement in the Y position on the grid if viewed on a screen.

The image in Figure 5-12 is the parsed data of the laser spot taken at the starting position of the experiments. The height of the spot from the surface was 1000 μm. The 144 μm spacing is in the direction of the columns.

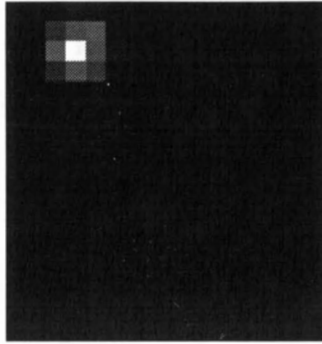

Figure 5-12: Parsed image of laser spot for TC211, 16x17 holes, 30 μm holes, and 16.7 aspect ratio

The apparent size of the spot at a height of 1000 μm from the sensor was 280 μm. Figure 5-13 shows a plot of this parsed image. The graph shows the data at each detector (hole) and the ideal value from a gaussian beam with the radius of 280 μm which results in a good match.

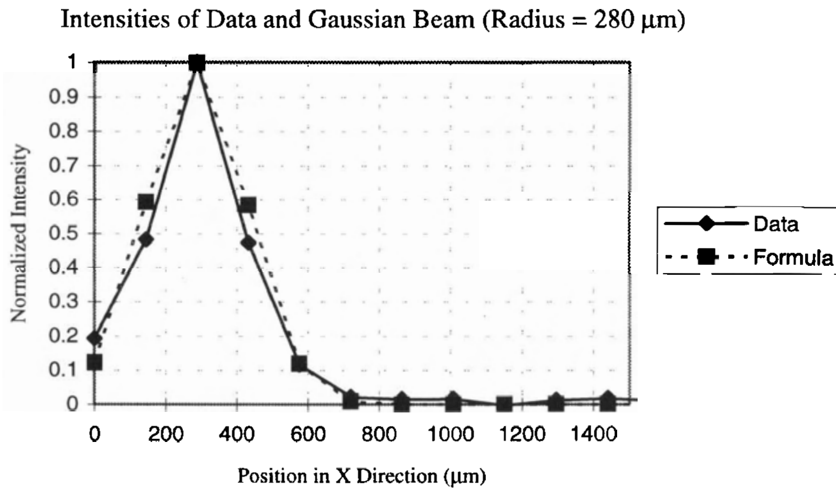

Figure 5-13: Comparison of data and ideal gaussian beam for X-Y table laser experiment with TC211, 33 μm holes and 16.7 aspect ratio

5.4.2 Results

The graph in Figure 5-14 is a plot of the error versus displacement. The error is the difference between the calculated position from the data minus the actual position (displacement). The displacement is the distance from the center of one hole. From both

samples it can be seen that the error is 18.2 μm to -32.9 μm. These results used equation (5-2) to calculate the distance. The height of the light diffuser is 1000 μm.

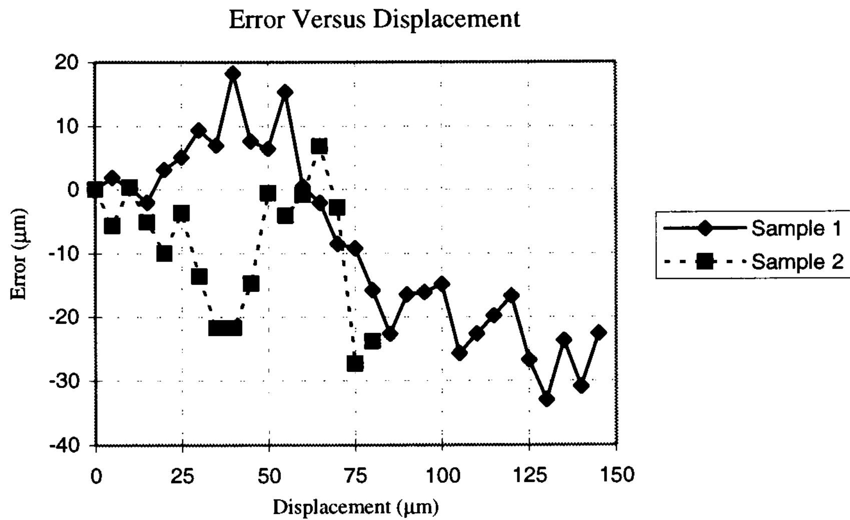

Figure 5-14: Graph of error for a height of 1000 μm with TC211, 33 μm holes and 16.7 aspect ratio

The graph in Figure 5-15 shows the error that results if only the highest signal detector is used.

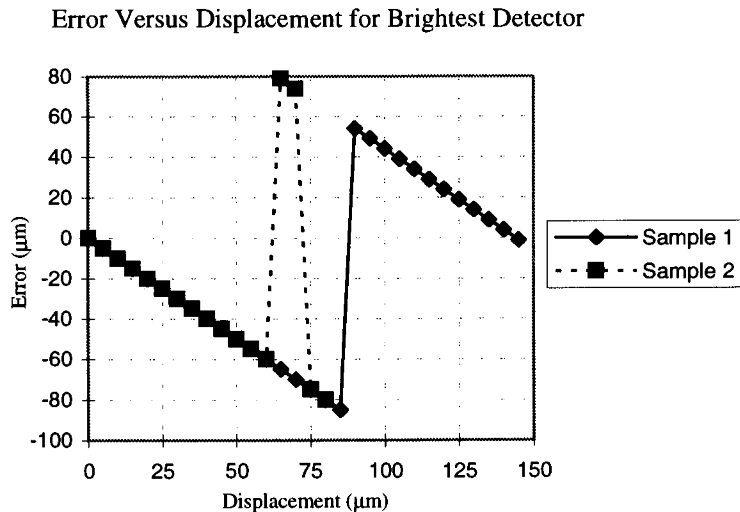

Figure 5-15: Graph of error using the brightest detector for a height of 1000 μm with TC211, 33 μm holes and 16.7 aspect ratio

Of course the error is mostly a straight line, which changes from a positive to a negative error when the brightest hole switches from one detector to the next. The error range is from 79 μm to -85 μm. The error shown in Figure 5-14 is about 3 times less using equation (5-2) then using the brightest spot.

Measurements were also tried at larger heights. The graph in Figure 5-16 is the error at a height of 2000 μm. Both the error from using formula (5-2) and the brightest spot are shown. The error at this height using the formula was 16.9 μm to -66.1 μm and using the brightest spot resulted in an error of 74 μm to -100 μm.

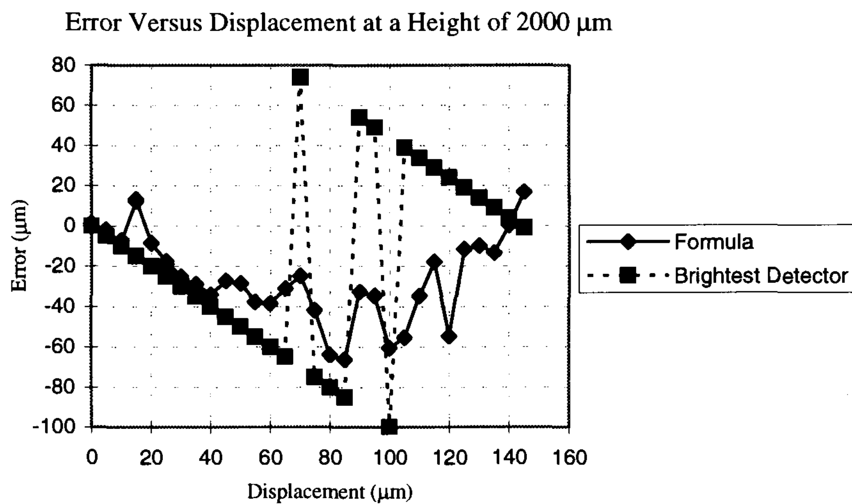

Figure 5-16: Graph of error at a height of 2000 μm with TC211, 33 μm holes and 16.7 aspect ratio

As seen from the graphs, even using equation (5-2) results in an error from the actual displacement. Some of these are inherent in using the formula itself. The next section discusses the errors resulting from the formula as well as from other sources.

5.5 Discussion of Errors

The sources of error are important to find the reasons on how to obtain the maximum accuracy from the sensor. The source of error from the formula is discussed as well as the

error from differing hole sizes. Simulations of a gaussian beam were performed on a row of holes separated by 144 μm between holes, the same spacing seen in section 5.4. A gaussian beam simulation was used as discussed in 5.1 but the beam radius simulated was 300 μm, and the range over which the simulation of the beam took place was a 1200 μm square.

5.5.1 Simulation of Ideal Sensor Error

To determine the error inherent in the equation (5-2), a simulation of the laser beam was completed for a sensor of 30 μm sized hole, 500 μm thick mask, and a height of 1000 μm and 2000 μm which were the same nominal parameters as the measured sensor. The graph in Figure 5-17 shows the error from the formula, which results from a perfect or ideal sensor and spot. The sinusoidal error is caused by the interpolation formula approximation of the true distribution as in Figure 5-1.

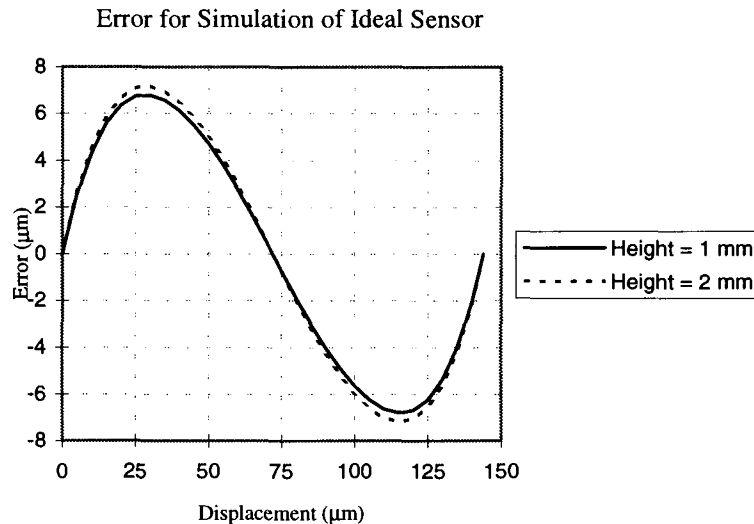

Figure 5-17: Error from simulation of ideal sensor with 30 μm holes, 16.7 aspect ratio and 144 μm spacing

The error range using this formula is ±6.8 μm for a height of 1000 μm and ±7.2 μm for a height of 2000 μm. Thus the maximum error expected from using equation (5-2) is

no more 8 μm. Yet from the data seen in section 5.4, the error is much larger then the one shown in the simulation. The simulation was an ideal case where the sensor was perfect, the hole spacing was 144 μm, and the hole diameters were exactly 30 μm. Further simulation were done to investigate the source of the error encountered in the experiments, as shown in sections 5.5.2 and section 5.5.3.

Finding the errors that existed was important for using a correction factor. The laser spot, as seen from the graph in Figure 5-13 in section 5.4.1, is close to being an ideal gaussian. The accuracy of the holes' center to center spacing is the same accuracy as the laser table with a value of 0.1 μm. The hole is consistently the same diameter through the thickness of the mask. The only parameter that is variable in the mask is the hole diameter. The data in section 3.4 shows that slight changes in power and duration changes the sizes of the holes. A fluctuation of holes sizes by about 10% were seen when diameters where measured. Thus, the parameters that are changed are the hole diameters.

5.5.2 Simulation of Large Homogenous Hole Diameters

The simulation seen in section in 5.5.1 consisted of homogenous hole diameters of 30 μm. The simulation in this section assumes all the holes are the same diameter but are larger than the ideal value. The diameter used was 40 μm for all of the holes. Again the simulation moved the gaussian between two holes and equation (5-2) was used. The graph in Figure 5-18 shows the result of the simulation at two different heights. The error for a height of 1000 μm is ±6.9 μm and for a height of 2000 μm is ±7.6 μm. The error resulting from the larger holes is only slightly larger than for the 30 μm. Equation (5-2) still functions properly for this data. For example, in the middle of two sensors, the middle and maximum still have the same intensity. The only difference is that the detectors see more light.

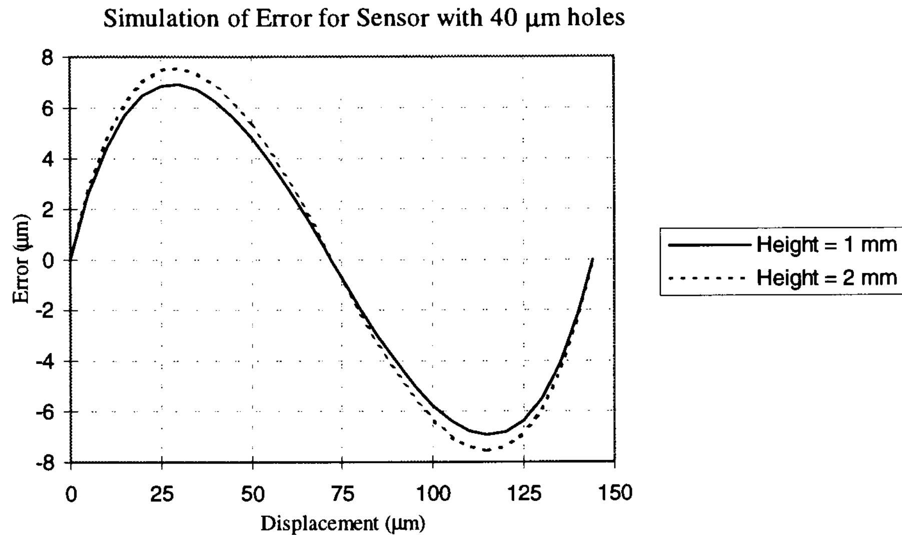

Figure 5-18: Error from simulation of 40 μm holes, 12.5 aspect ratio and 144 μm spacing

A more realistic situation for the detector is not one in which the holes are the same diameter for the whole mask, whether 30 or 40 μm, but where the hole diameters vary from hole to hole.

5.5.3 Simulation of Differential Hole Diameters

The simulation of varying hole diameters was tried. The simulation results, shown in Figure 5-19, was a sensor with the same hole to hole spacing and mask thickness as the other simulations, but the hole at the starting central position had a diameter of 32 μm instead of 30 μm and all other holes in the simulation have the same radius of 30 μm. The starting position was at the displacement of 0 μm. The next hole was at 144 μm and the simulation moves the laser spot from one hole center to the next.

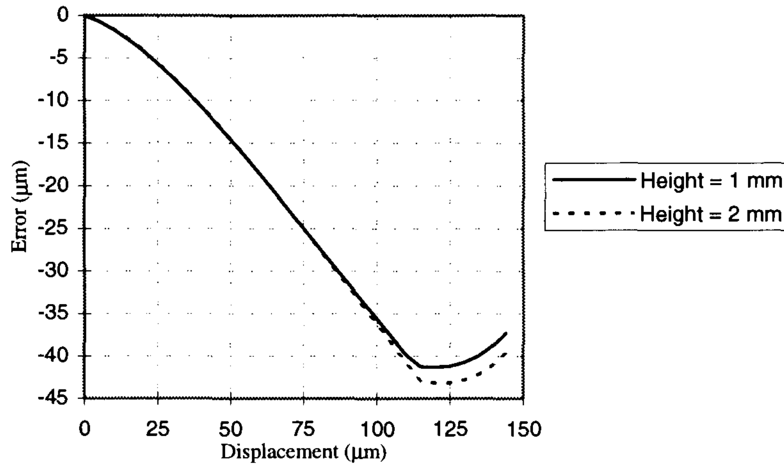

Figure 5-19: Error from simulation of differential diameters

Not only does the hole at the origin have a larger light acceptance angle (3.67 ^{o} compared to 3.43 ^{o}) because of the larger hole, but it also collects more light. Thus, the simulation also multiplied the area of each detector to simulate the larger light collection area. The error for the height of 1000 μm was from 0 μm to -41.3 μm, and for the height of 2000 μm, 0 μm to -43.2 μm. The difference in the error from the two heights is small, but the error is still quite large for each. For example a 2 μm change (6.25 % larger) in the diameter of the hole at the 0 μm location, resulted in an error range that tripled.

Also noticeable is that the shape of the error curve is very similar to the graphs of data shown in section 5.4.1, as well as the error values being similar. Although the error is larger in the data for the 2000 μm height, the values for 1000 μm are close. The discrepancies for the error could be caused by other holes being variable in size and thus having a greater effect at larger distances. The simulation was completed with only one hole being larger than the rest of holes in the mask. The possible combinations of hole sizes are large, so only a simple case was simulated. From the data and the simulation, especially for the height of 1000 μm, it is likely that the hole positioned at the 0 μm location for the data is larger than the rest similar to the simulation. The positive error

seen in the lower displacement values. could be caused by a neighbouring hole (minimum value hole) being too low, and thus creating a position value that is too high.

Because the simulation shows that the hole sizes play a key role in error, and the holes are seen to vary in diameter on the actual mask, the hole sizes and pixel sensitivity are the main source of error in the experiments. The diameters will not only vary for one hole, but will change from hole to hole throughout the array. Although too complex to look at all the possibilities, the simulations do show a sensitivity to these variances in holes sizes.

5.5.4 Calibration

The simulations and data show a need to calibrate the results to compensate for the errors, which were mainly caused by the changes in hole size. The calibration is based on the data from the simulation. The same calibration was then performed on the data. The calibration is just a change to equation (5-2).

5.5.4.1 Corrected Formula

The two conditions mentioned in section 5.2 for equation (5-2), that being when the spot is over the center of a hole and when its in the middle between two holes, are important for the formula to give a proper result. When the spot is over the center of a sensor, the two neighbour holes on either side are the same intensity (Figure 5-3, j-1, j+1), and when the spot is in the middle between the two holes, the two holes have the same intensity (Figure 5-4, j, j+1). But when one of the holes is too large, this condition is not met. When the holes are equal and are about to switch intensities (i.e. the middle value becomes the maximum value and vice-versa), this change in value will not occur. Thus a hole will stay the maximum, when it should become the middle value. The same can be true when the spot is over a detector. If one the holes is too large, it will register as a

middle (j+1) value when, it should be a minimum (j-1) value. To counteract this effect, equation (5-2) has been modified with constants as shown in equation (5-3).

$$(5\text{-}3) \quad \Delta x = \frac{I_{mid} - AI_{min}}{2(BI_{max} - AI_{min})}$$

The constants A and B are different for each hole set of I_{min}, I_{mid}, and I_{max}. The formula for A is in equation (5-4) and is derived when the laser spot is directly over the center of a hole, and thus the two neighbours on either side are the min. and mid values.

$$(5\text{-}4) \quad A = \frac{I_{mid}}{I_{min}}$$

The constant A changes the values such that I_{mid} and I_{min} become equal, meeting the first condition from section 5.2.

The formula for B is in equation (5-5) and is derived only when the laser spot is in the middle between two hole. The constant thus makes I_{mid} and I_{max} equal, the second condition from section 5.2. Thus the two conditions are met in equation (5-3) as they were for equation (5-2).

$$(5\text{-}5) \quad B = \frac{I_{mid}}{I_{max}}$$

To use these ranges in a program, the uncalibrated intensities would be looked at to determine the minimum, middle, and maximum values, and then the A and B constants would be grabbed from a table. For extra accuracy, if after calibration the intensities change such they are not in proper placement (i.e. minimum value now becomes a middle value), then this new set of constants can be chosen from the new set of minimum, middle and maximum values. This extra calibration may not work and should only be done once.

No program was written to take care of these corrections, instead the intensities were looked at directly and calibration occurred on a spreadsheet.

5.5.4.2 Correction of Simulation

The correction formula was tried on the differential hole diameters, because the new formula in equation (5-3) was meant for this type of error. The values of A and B were calculated from the simulated data. The graphs in Figure 5-20 shows the error with and without calibration at a height of 1000 μm. The error range has been reduced from 0 to -41.3 μm, to ±6.8 μm for the calibrated values.

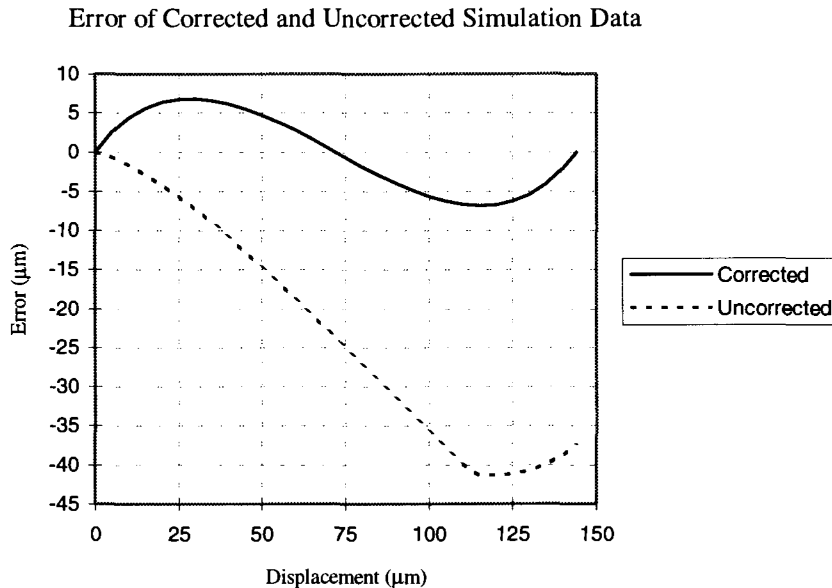

Figure 5-20: Error of un/corrected simulation data at 1000 μm, with differential hole sizes

Also, as can be seen in the graph in Figure 5-21, the error 2000 μm was reduced. The calibration values were calculated from the 1000 μm height, and applied to both sets of data. The error at a height of 1000 μm is ±6.8 μm and for a height of 2000 μm, the error was from 7.9 μm to -6.4 μm, which is a very small difference from the error at 1000 μm.

The error has been reduced to a value similar to that of the ideal sensor. The technique of using equation (5-3) has almost corrected the error.

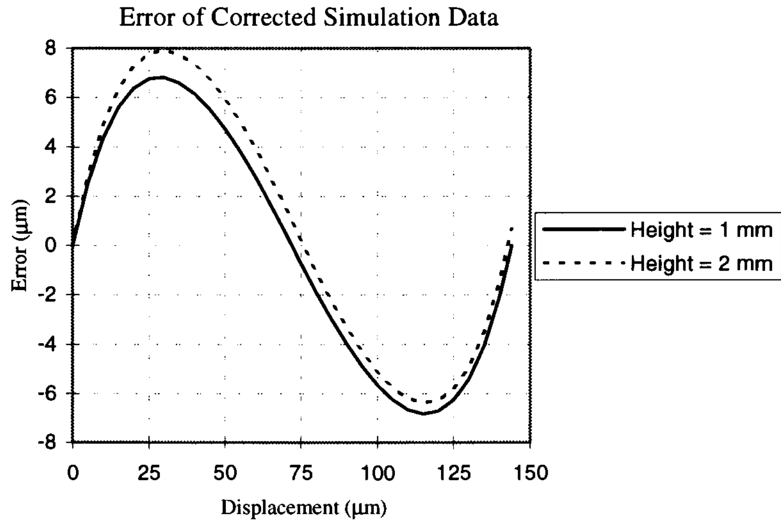

Figure 5-21: Error of corrected simulation of differential hole diameters

5.5.4.3 Correction of Data

Only the data sample at a height of 1000 µm was calibrated from the X-Y table experiments. Comparing the results of directly over the jth hole, and mid way between the jth and the $j+1^{th}$ hole, the measured data showed the jth hole to be too large. Figure 5-22 is a graph of the error of the corrected data.

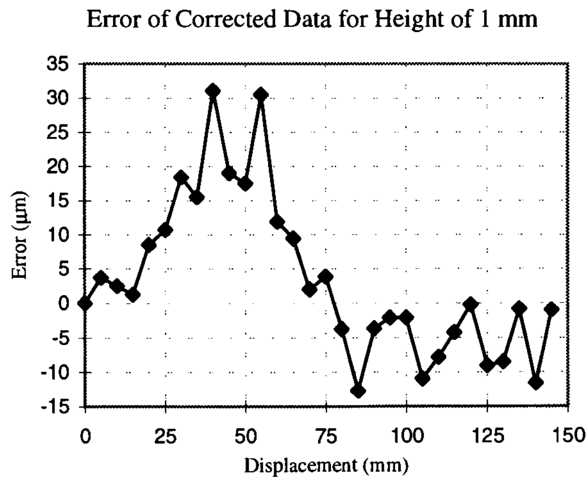

Figure 5-22: Graph of error for calibrated proximity data at a height of 1000 µm

The error range of the corrected data is 31.1 μm to -12.7 μm. For an unknown reason the error is greater in the positive range, it is less in the negative range. The root mean square of the error was reduced by 27.7 % using this calibration technique. The error correction is not as good as was expected from the simulation. The first half of the displacement range (0-72 μm) seems to have odd data, whereas the second have seems to fit the correction. Because a 72 μm and 144 μm point were not originally measured, the values at 70 μm and 145 μm were used instead. These values are only off by no more than 2.5 μm, which is about the same as the starting point error of 1 μm.

Reasons why the data could not be corrected properly may have resulted from additional sources of errors. One obvious error is the shape of the holes and the material around the opening. Some holes may have been deformed and contained low aspect ratios dependent on the direction, such as a slight notch. Also, material on the surface that was ejected out of the hole during the laser drilling could have produced shadowing effects that could be direction dependent. Even with these errors, the error ranges were still less than the expected value of ± 72 μm when using the brightest spot location.

The data from the 2000 μm resulted in no improvement over the original data because there was no good center point between the holes to get the calibration from. Even using the calibration from the 1000 μm height resulted in no improvement.

5.6 Summary

The proximity measurements were conducted on the sensor and the data was shown in this chapter. The simulation of a gaussian beam showed that the beam still looked gaussian from the sensor and this was confirmed by the data fitting well to a gaussian. A simple formula was used to calculate the center of the spot as opposed to the brightest spot. The data from the angled laser experiments resulted in errors of 45.2 μm to -42.4 at a height of 1532 μm, which was about half the error if the brightest spot technique was

used. A different set-up using the laser table was used, and the experiments had errors of 18.2 μm to -32.9 μm at a height of 1000 μm. Even though the simulations showed less error, and these errors should have been eliminated through calibration, the data only showed a 27.7 % decrease in the root mean square of the error. Sources of error other than hole diameter may have played a role in the measurements, such as material around the edges that were produced during laser hole drilling.

CHAPTER 6: INTEGRATED PROXIMITY SENSOR

As an integrated implementation of the vision skin concept, a proximity sensor with the photocells and circuitry to calculate the proximity was designed and then sent to the Canadian Manufacturing Corporation (CMC) for fabrication in the Mitel 1.5 μm technology. The integrated sensor contains an 8x8 grid of photocells, and the brightest spot is determined and outputted. The chip was meant as a prototype and is flexible enough to support larger arrays.

6.1 Concept

The circuit finds the brightest spot in the 8x8 array of photodiodes, which are 100 μm squares with 200 μm spacing from center to center. The control circuitry uses a current comparator and searches through the whole array for the detector with the largest intensity. Figure 6-1 shows the layout of the circuit and Figure 6-2 shows a picture of the actual circuit. The control circuitry contains a finite state machine, the comparator register, and circuitry that creates signals for comparing intensities. The control circuitry stores the address of the winner (largest value so far), the diode to be compared to the winner, and the final value. The final value register is updated after the full array is

searched. The photodiodes array was set up in a similar manner as memory and would be no problem in expanding the array in this circuit.

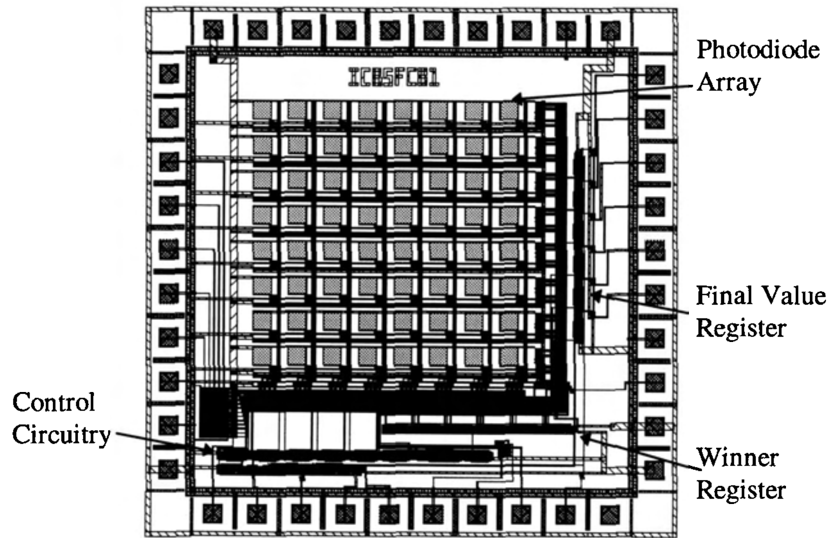

Figure 6-1: Layout of integrated proximity sensor (3.1 mm x 3.1 mm)

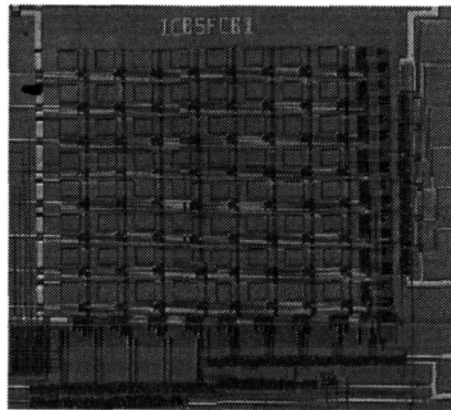

Figure 6-2: Picture of integrated proximity sensor (3.1 mm x 3.1 mm)

At each new pass through the array, the first photodiode is assumed to be brightest detector. The operation of the sensor can be summarized in the given pseudo code below. The values X_{winner}, Y_{winner}, $X_{compare}$, $Y_{compare}$, and X_{final} and Y_{final} are the X and Y location (registers) of the array of the winner diode, the diode to be compared and the location of the final winner of the whole array respectively. The variable P(x,y) is the photodiode array with the address or location of x and y.

Table 6-1: Integrated proximity sensor pseudo-code

```
X_winner = 0
Y_winner = 0
for Y_compare = 1 to 7
    if P(X_compare,Y_compare) > P(X_winner,Y_winner)
        X_winner = X_compare
        Y_winner = Y_compare
    end if
end loop

for X_compare = 1 to 7
    for Y_compare = 0 to 7
        if P(X_compare,Y_compare) > P(X_winner,Y_winner)
            X_winner = X_compare
            Y_winner = Y_compare
        end if
    end for
end for

X_final = X_winner
Y_final = Y_winner
```

The algorithm is made longer because of setting the first photodiode (P(0,0)) as being the winner at the start. The first location could not be compared with itself, since it would mean the photodiode would pull two sources. The operation of the photodiode is discussed in section 6.2. The sensor must then compare the first column starting at the second row. The remaining array then had to be compared. Not only is the algorithm longer, but the finite state machine was also made more complex, in order to handle these starting conditions.

6.2 Photodiode Cell

Light collection is obtained through the use of photodiodes that are part of the microchip. Figure 6-3 shows the layout of the cell. The photodiode is a n-doped region

inside a p-well, where the p-well is tied to V_{ss}. The circuit diagram of the photodiode cell is shown in Figure 6-4.

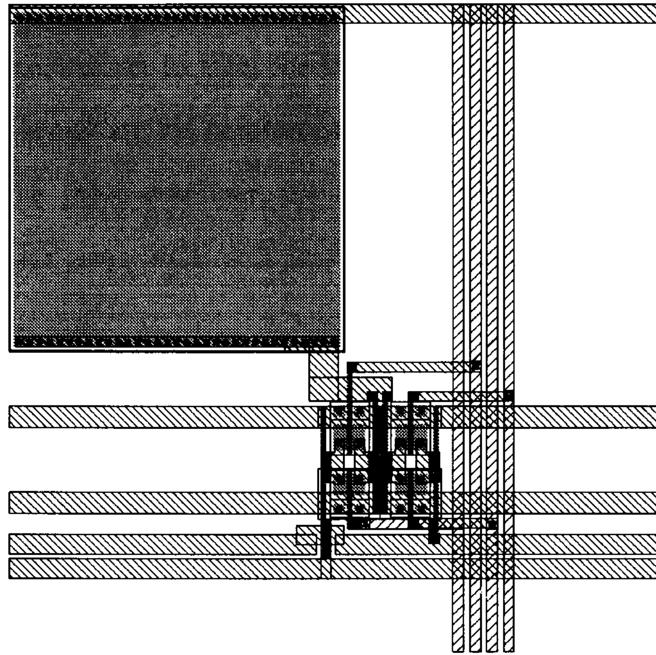

Figure 6-3: Layout of photodiode cell (200 μm x 200 μm)

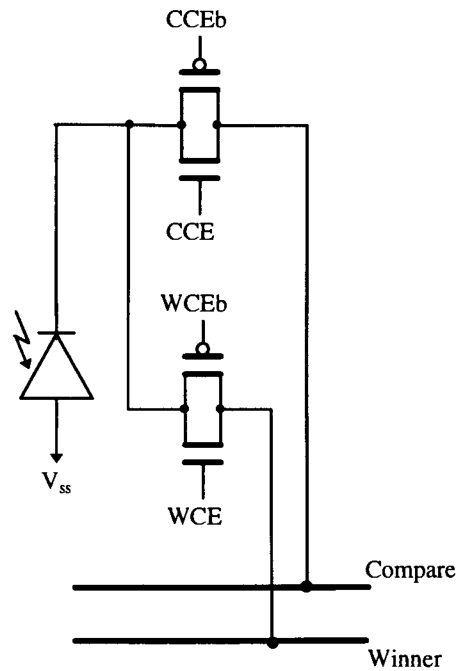

Figure 6-4: Circuit diagram of photodiode cell

The photodiode cell is made modular such that they can be laid out in either the X or the Y direction to create an array. Each photosensitive area of the cell is 100 μm square and the total size of the cell is 200 μm, thus the spacing between each photodiode is 200 μm as well. This size was set to meet the initial expectation for the shadow mask. The vertical lines in the layout are the column enables for the winner and comparator line. If the photodiode is the present winner, the winner column enable (WCE) line will be active, and the transfer gates WCE will pass the current to the winner line. Note that the winner values are not stored, so that it is assumed the signal remains nearly constant over the scanning time of the array (which is short). If the diode is the next cell to be compared, the comparator column enable will be activated (CCE). Each column in the array has to be activated separately. Each cell in all the rows of one column will become active, but each row has a separate compare and winner line. At one side of the array a row select for both the winner and compare are activated. No photodiode is both the comparator and the winner, because this condition is guaranteed by skipping the first photodiode for comparison.

Even if the comparator and winner are on the same column, and thus all the compare and winner lines are connected in one column, the row select will only complete the circuit for one line (both can not have the same row because they already have the same column value). For the case when the same row selected, two different columns will be activated separately for the winner and comparator line.

6.3 Current Comparator

The current comparator determines which two currents are the largest. The circuit diagram is shown in Figure 6-5. Because of the configuration of the photodiodes, the larger the intensities, the larger the current that is pulled through the comparator. The line 'Compare' and ''Winner' are the same lines from the photodiode diagrams. For the

comparator to operate, the first signal Precharge is set high. The currents from each of the photodiodes (comparator and winner) are pulled through the transmission gates and the two nodes, n1 and n2, are shorted at this time as well. In the next clock cycle, Precharge is turned off. The voltage in the inverter pair then equalizes. If the compare line produced a higher current, then n1 is low and n2 is high. In the next clock cycle Grab is set high and the value at n3 becomes high. In the next clock cycle the Latch is high, and WCLK becomes low. The normal value for WCLK is high, thus if 'Winner' is still the largest intensity, WCLK will remain high. Only if 'Compare' is larger will WCLK go low. The cycle is started over in the next clock cycle. Thus a low pulse occurs if the 'Compare' is larger. The signal WCLK latches the compare value to the winner register (D flip-flops, negative edged triggered, asynchronous reset and clear), when the signal goes from high to low, thus latches when 'Compare' is larger.

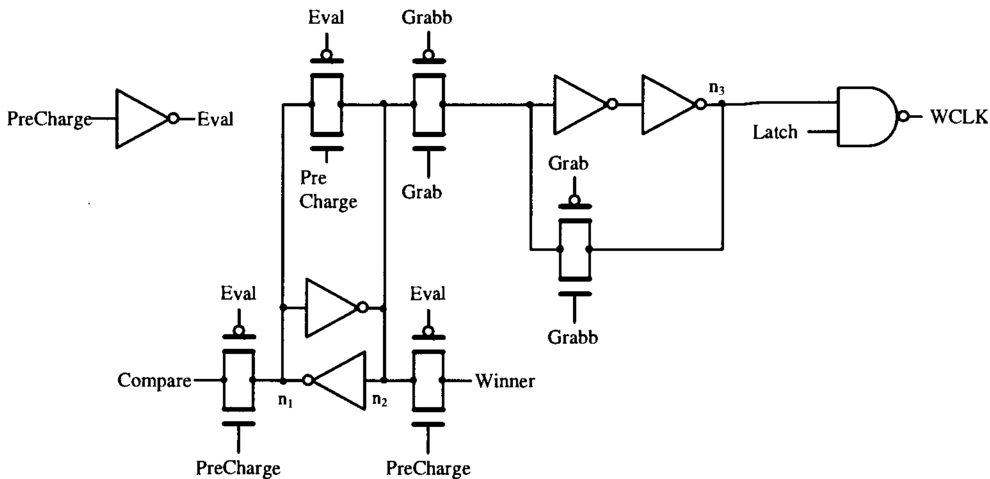

Figure 6-5: Circuit diagram of current comparator

6.4 Control Circuit

The control circuit consists of three major parts: the circuitry for the control signals for the comparator, the comparator register (the address of the photodiode to be compared), and the finite state machine which is shown in Figure 6-6.

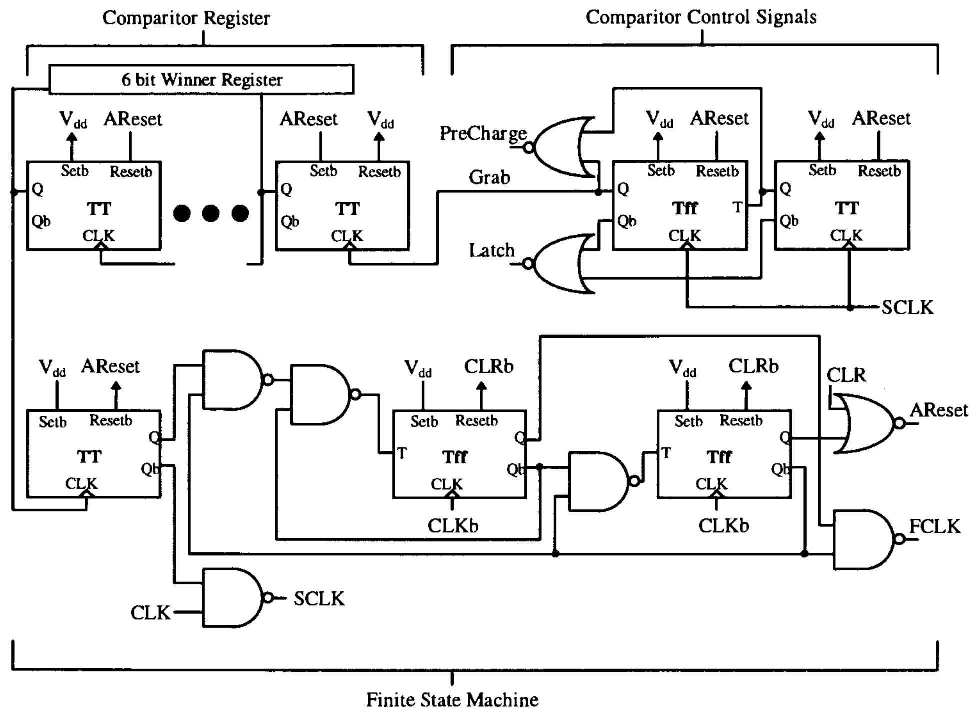

Figure 6-6: Circuit diagram of control circuit

The cell Tff is a T flip-flop that toggles at the negative clock edge when T is high, and the cell TT is a T flip-flop with the T line held high. All the flip-flops are negative clock edged triggered and contain an asynchronous reset and set on a low signal.

The control signals from the comparator are generated by the flip-flops and produce the signals discussed in section 6.3. The signal WCLK is generated by the latch signal and the comparator (Figure 6-5). When the Q output line of the Tff for the control signal goes from high to low it triggers the comparator register. Thus the comparator register is incremented one value after all the signals needed for a comparison are finished. The comparator register is just a binary counter used to store the 6 bit address of the diode to be compared. The first flip-flop will be set high when AReset goes low, unlike the rest of the counter that is set low, which is meant for the first location of the photodiode to be skipped. When the highest bit of the comparator address goes from high to low, the finite state machine starts. At this point the first flip-flop will turn off the clock (SCLK) for the control signals, by setting it constantly high. Both the control signals and the finite state

machine use an inverted clock, making the circuitry a little simpler and not requiring an inverter at the end of SCLK. The finite state machine resets the comparator register and comparator signals through the line of AReset. As can be seen, if the comparator register changes its highest bit from high to low, then the register becomes low. Because we do not want to compare this first photodiode, extra circuitry is needed for the finite state machine. A general reset signal (Reset) will reset the whole control circuit (finite state machine at zero state).

The finite state machine resets the control circuitry, stops the clock and also controls the signal FCLK (final clock). When the signal FCLK goes low, the address of the winner from the scan will be stored in the final register as shown in Figure 6-7. This register tells the outside world the location of the brightest photodiode, which is the location of the center of the spot, and thus the height can be determined.

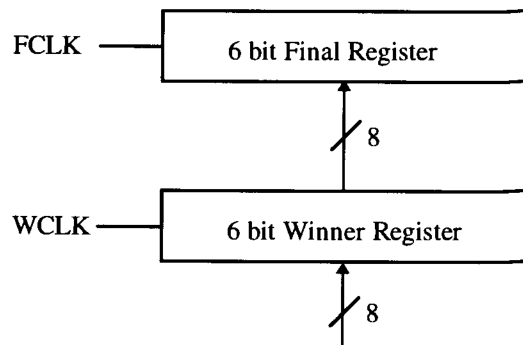

Figure 6-7: Final and Winner registers

The table 6-2 is the state table for the finite state machine. The bold entries are conditions or states that are not suppose to exist. The Q0 (which is TT) should not toggle at any time because SCLK is always off, thus there can not be toggling through the control circuit, and thus no carry out from the comparator register. Also, the dual values in some of the bold entries indicates the value will change depending if the carry out is before or after the next clock cycle. Also, the AReset is asynchronous thus SCLK will be equal to CLKb when AReset is low, but nothing will happen to the comparator control

signals, because the flip-flops will be held low at that time. All entries not bolded show the flow of the finite state machine under normal operation

Table 6-2: State table

Present State			Input Signals		Output Signals			Next State		
Q_2	Q_1	Q_0	MSB (1 to 0)	CLR	SCLK	AReset	FCLK	Q_2	Q_1	Q_0
0	0	0	0	0	CLKb	1	1	0	0	0
0	0	0	X	1	CLKb	0	1	0	0	0
0	0	0	1	0	CLKb	1	1	0	0	1*
0	0	1	0	0	1	1	0	0	1	1
0	0	1	X	1	1	0	0	0	0	0
0	**0**	**1**	**1**	**0**	**1**	**1**	**0**	**0**	**0/1**	**0**
0	**1**	**0**	**0**	**0**	**CLKb**	**1**	**1**	**1**	**0**	**0**
0	**1**	**0**	**X**	**1**	**CLKb**	**0**	**1**	**0**	**0**	**0**
0	**1**	**0**	**1**	**0**	**CLKb**	**1**	**1**	**1**	**0/1**	**0**
0	1	1	0	0	1	1	0	1	0	1
0	1	1	X	1	1	1	0	0	0	0
0	**1**	**1**	**1**	**0**	**1**	**0**	**1**	**1**	**0**	**0**
1	**0**	**0**	**0**	**0**	**1**	**0**	**1**	**0**	**0**	**0**
1	**0**	**0**	**X**	**1**	**1**	**0**	**1**	**0**	**0**	**0**
1	**0**	**0**	**1**	**0**	**1**	**0**	**1**	**1/0**	**0**	**1**
1	0	1	0	0	1	0	1	0	0	0
1	0	1	X	1	1	0	1	0	0	0
1	**0**	**1**	**1**	**0**	**1**	**0**	**1**	**1/0**	**0**	**1**
1	**1**	**0**	**0**	**0**	**CLKb**	**0**	**1**	**0**	**0**	**0**
1	**1**	**0**	**X**	**1**	**CLKb**	**0**	**1**	**0**	**0**	**0**
1	**1**	**0**	**1**	**0**	**CLKb**	**0**	**1**	**1/0**	**1/0**	**0**
1	**1**	**1**	**0**	**0**	**1**	**0**	**1**	**0**	**0**	**0**
1	**1**	**1**	**X**	**1**	**1**	**0**	**1**	**0**	**0**	**0**
1	**1**	**1**	**1**	**0**	**1**	**0**	**1**	**1/0**	**1/0**	**0**

* Immediately switches to 001 state, before clock next clock cycle ends

6.5 Simulation

A simulation of the integrated proximity sensor was completed on HSpice and the spice file is shown in Appendix H. The graphs below in Figure 6-8 are the timing diagrams from the simulation. For the simulation, only 4 addresses were available, to reduce the simulation time. Also, the location 01 is where the largest intensity exists.

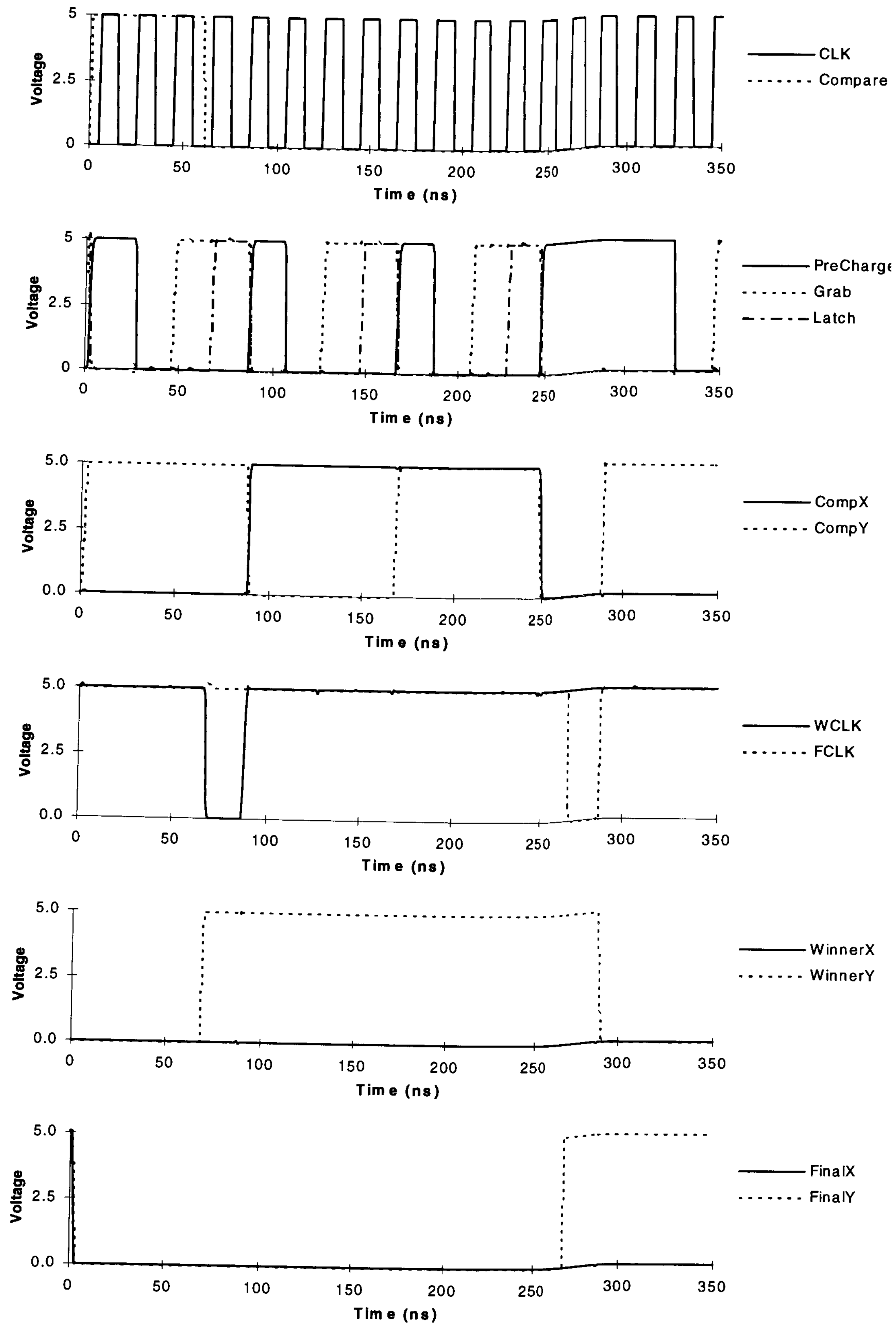

Figure 6-8: Timing diagrams from simulation of integrated proximity sensor

As can be seen from the simulation, the winner becomes location 01 and the value is propagated into the final register value. Note that at the end of the latching the final values and the compare register are set back to 01 and the winner register is set to 00. The fastest clock cycle that could be used in the simulation was 20 ns, which results in a possible frame rate of 190 thousand frames per second for the full circuit. This simulation does not take into account the capacitance effects from the pads, so the frame rate is expected to be lower for the actual circuit.

6.5 Second Design Improvements

A second design of the integrated proximity sensor was submitted to CMC in the Mitel 1.5 μm technology. The design was improved upon by providing a current tap, and bias current capability. The current tap allows for current from the photodiode that is being compared, to be seen from the outside. Because the compare register cycles through 0 to its maximum value, it can be used for addressing each photodiode. By looking at the current from the output line, the value from each sensor can eventually be seen. The second improvement was a bias current offset for the winner photodiode. This current allows the winner photodiode to have a slightly larger intensity than its original value. Thus an error range can be established, where the compare intensity has to be higher by a certain amount than the winner, before it becomes the winner. Of course, the current can not be too large to the point of pulling current through the photodiode (the voltage at cathode would have to be lower than 0). The circuit diagram in Figure 6-9 shows the improvements with the changes to the winner and compare line. The labels, compare and winner, are the lines after the photodiode and before it enters the comparator. I_{out} is the tap, and I_{bias} is the bias current. When the tap signal is on, the current stops flowing through the winner line and I_{bias}. The current from compare is diverted to I_{out}.

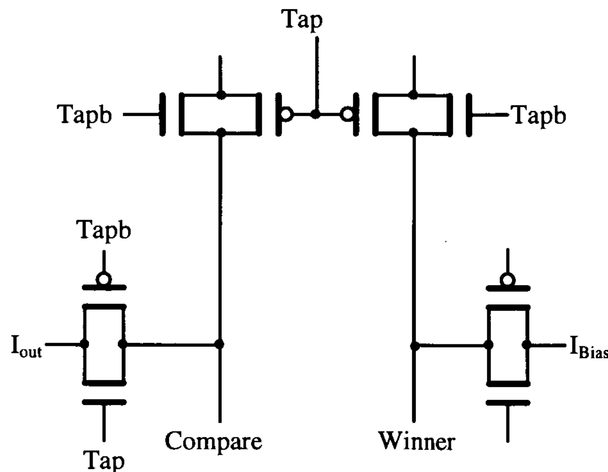

Figure 6-9: Circuit diagram of improvements

6.6 Status of Integrated Proximity Sensor

The first sensor has been manufactured and has been tested. The photodiodes seem to function properly, but the chip does not work. The chip was not able to find the photodetector with the largest intensity when used with the laser. A few signals were analyzed to investigate the problem. The line AReset was found to functioning properly. The signal is an asynchronous clear for some of the registers and control circuitry and is controlled by the circuitry and the input signal Reset. The signal Precharge did not have the expect voltages of 0 and 5 Volts. Instead the signal stayed at a value of 2.86 Volts and randomly would go to 0 Volts for a few clock periods. As seen from Figure 6-8, the signal Precharge is supposed to alternate between 0 and 5 Volts, and stays at 5 Volts for only one clock period expect near the end of cycling through all the photodiodes. The conclusion is a poor p-dopant level and thus transmission gates would not function properly for transmitting 5 Volts. All the flip-flops use transmission gates and would not function properly. The control circuitry would thus be in random states.

The modified design has been sent to CMC and will most likely be manufactured in the next months. Unfortunately the production of these chips are low priority and thus the exact date of delivery is unknown.

6.7 Summary

An integrated proximity sensor was designed in Mitel 1.5 μm CMOS and has been manufactured by CMC. The circuit finds the value of the photodiode with the largest intensity by looking through an 8x8 array. The control circuits scans this array, produces a final value in the form of an address or location of the photodiode with the largest intensity. The final address is stored in a 6 bit register. The simulation shows a possible frame rate of 190 thousand frames per second. The modification of the design enables the current to be tap from each photodiode, as well as a biasing of the winner photodiode current. The sensor at present is still being tested and the modified design is waiting to be manufactured.

CHAPTER 7: FUTURE DESIGN

From the thesis design and testing of the proximity sensor future design improvements are suggested. The integration of the laser beam, larger arrays, real time acquisition boards, and angled holes are some of the suggestions.

7.1 Integrated Laser

The complete design of the proximity sensor uses a laser beam, off to the side of the sensor, that projects a spot. The testing done has simulated this laser beam, without actually integrating the laser into the sensor assembly. Continuing work is proceeding to investigate the integration of this laser, and the accuracy of the assembled sensor. The laser used is a laser diode of wavelength 670 nm. The diagram in Figure 7-1 is a representation of the prototype of the integrated laser.

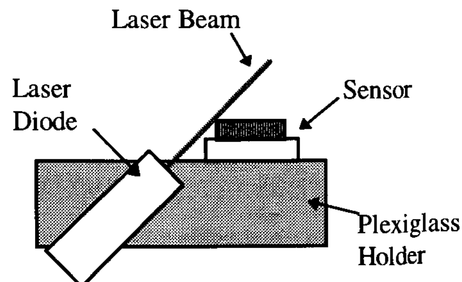

Figure 7-1: Prototype of integrated laser

The angle of the laser beam relative to the mask surface is 45°. In the ideal sensor, each row, or set of rows, will have its own laser for proximity measurements. The range of the sensor is limited by the size of the array. If the spot travels too high, it will go past the CCD sensor. One way to increase the height range is to make the angle of the laser larger. The larger the angle, the further the beam has to travel upwards before it is over the edge of the CCD array. Because height is determined by the equation (2-1) $Z = L \, Tan(\theta)$, any error will of course be translated by the same formula: $\Delta Z = \Delta L \, Tan(\theta)$. Thus if the tangent of the angle is large, then the error will be multiplied. For a 45° angle the error, the height is a one to one correlation to the distance across the surface of the CCD. The same sensor could also have multiple laser beams being project at different angles. Each beam would be for a certain height range, and have an error specific to it. For example with an angle of 63.43 ° the height error is twice the location error and for an angle of 77.57 ° the error is three times the location error.

Another way to increase the operating range is to increase the size of the photoarray, such that the laser has to travel a larger height before the spot goes off the edge of the array.

7.2 Large Photoarrays

Photoarrays with larger areas are needed for future proximity sensors. At present the TC211 has been used for testing, but the TC245 is being used with the integrated laser sensor. The TC245 offers a larger area (about 4 times more), and thus has an increase in the height range of the sensor. Unfortunately larger CCDs are more expensive to make than a smaller CCD for the same quality. For example, a 5x5 cm Kodak array cost $10,000 compared to $340 for the TC245 which is a 6.4x4.7 mm (assuming minimum quality on both). However linear CCD arrays give more proximity range at lower cost but would give up vision. For example a 1 pixel by 3 cm array costs only $140.

Even if larger arrays could be used with areas twice as large as the TC245, the more pixels means that more data has to be transferred from the CCD to the computer. The needs for faster and real time acquisition boards are necessary to allow the sensor to operate in real time.

7.3 Real Time Acquisition Boards

Not only do larger CCDs need a faster acquisition rate, but the present sensors using the TC245 needs these faster acquisition boards as well. Not only is the real time acquisition necessary but the ability to read and process the data, such as parsing and proximity calculation, needs to occur. The proximity sensors using the TC211 had to be parsed and processed after the data was collected and stored by another program. With an acquisition board, the light gathering and processing can be integrated.

A new board is being used for the TC245 that does this, which is an EDC1000L by Electrum. This board reads the pixels, does an 8 bit A/D conversion, and stores it in memory. The computer system used is an IBM PC, and the programs so far run only on a MSDos platform. Unfortunately, to read the complete array is only about 5.5 frames/sec as opposed to 32 f/s for real time systems but does allow a subset of all the pixels to be read, thus allowing the system to read rows that are relevant to parsing the information. The number of pixels read could be cut down by an order of 2-3. Some pixels between rows do not need to be read since they serve no function and are not even used by parsing. Depending on the spacing of the holes, determines the number of pixels that is useful. The system allows for rows to be skipped and this function would speed the data acquisition. The program listing in Appendix I shows the functions needed to process and parse the data from these boards.

For larger arrays, faster boards will need to be found, or a different photoarray that allows for quicker access of intensity values.

7.4 Mask Hole Patterns

As seen from section 3.4, the smallest hole to hole spacing for the mask is around 150 μm. But the mask was laid out in a grid pattern, thus not all neighbours for each hole are as close as 150 μm. To increase the density of the mask a different hole pattern should be tried, which makes sure all neighbours are 150 μm from each other, essentially an equilateral triangular pattern, with the holes at each intersection. The spacing on each edge would be 150 μm. The diagram in Figure 7-2 demonstrates the pattern. Although this array configuration has not been tried because a simple grid pattern is easier to extract the data from, the higher density array should work. The main parameter limiting density is the hole spacing, and since all neighbours are no closer, flow from one hole should not effect the neighbour. This configuration should increase the density of the grid by 15 percent.

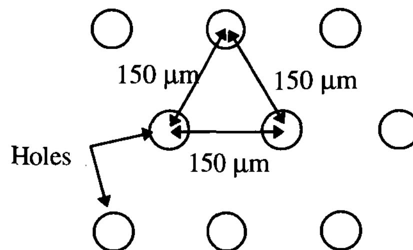

Figure 7-2: Higher density grid array

The increase in density allows for finer detail in close imaging with the sensor. The closer holes mean that more points can be sampled for the proximity detection. Unfortunately, the configuration adds a little more complexity if the spot is being located between rows, since it requires the distance between holes at a 60° angle.

7.5 Double Masking

Although double masking was successfully done for earlier mask density as discussed in 3.4.4, for the higher density masks the alignment was not accurate enough.

Half the holes in the double mask (for 150 μm hole) were misaligned during the first test. The technique of using pins was not accurate enough and a different procedure will be needed. One suggestion is to glue the masks separately, one at a time, such that when the second mask is placed, it is separately aligned. Using probes could offer the accuracy of moving the mask. Whether this works remains to be seen.

7.6 Angled Holes

One possible modification that could change how the sensor functions is the use of angled holes in the mask. For the lensless imaging, a form of stereo vision could be created. The diagram in Figure 7-3 is an example.

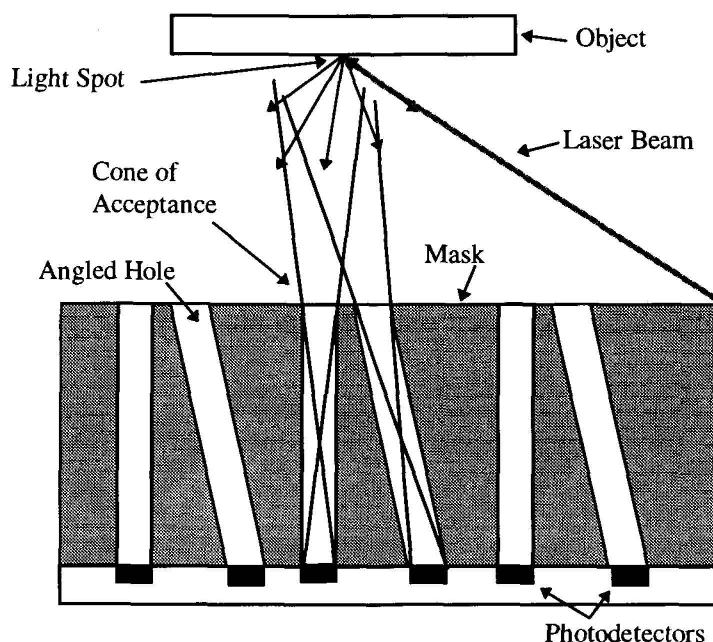

Figure 7-3: Angled holes

Not only is a stereo image created, but proximity could be calculated as well. If a spot is seen by two holes (both at different angles) then the intersection of their lines of sight will give a distance from the surface of the mask. Of course, the cone of acceptance does create an error range, where the spot will not be located at a point but in a range in a

volume of space. The angled hole should be possible but it will present challenges. One possible problem is the increase in the apparent thickness of the mask. If the laser approaches from an angle, the beam has to travel more distance though the mask material in order to create a hole. Whether these holes will be of good quality or the hole to hole spacing will be similar to the original masks will have to be investigated.

7.7 Summary

Although the sensor was built, different areas do exist for improvement on its design. One major implementation is the integration of the angled laser with the sensor. This integrated package would be more functional. Larger photoarrays were suggested to increase the range of the sensor as well as the need for faster boards to acquire the photoarray data.

Suggestions for the mask were to increase the density of the number of holes in the mask by changing the hole pattern. To increase the working distance, a new technique to join two masks together should be found. For more functionality, angled holes in the mask were mentioned, which would create stereo imaging, and a different technique to calculated height.

CHAPTER 8: CONCLUSION

A new type of proximity sensor was built and tested during this thesis. Small holes in thick black polypropylene were created to form a high density mask with an aspect ratio of 16.7, and an acceptance angle for each hole of 3.4°. The black polypropylene was found to be the best material for the construction of the mask, having such properties as low thermal conductivity and high electrical resistivity.

The sensor was capable of viewing simple images at a distance of 12 mask thickness from the sensor. Although the images were defocused for large heights, by using a simple 3x3 averaging filter and gamma correction, the images were enhanced and were made more recognizable. Proximity tests were completed and at a height of 1 mm, an accuracy of ±33 μm was measured, and for 2 mm an accuracy of ±67 μm was measured. These heights were calculated using a formula that required only three points. The formula estimated the gaussian beam as a triangular spot. The major limitation to the accuracy, learned from the data and simulation, was the quality of hole sizes. Very small variability in hole sizes created large errors in the measurement of height.

An integrated proximity sensor was designed and manufactured in Mitel 1.5 μm CMOS technology, and simulation showed the possibility of a frame rate far greater than

32 frames/second. The sensor contained a 8x8 photodiode array to locate the position of the brightest spot. Future enhancements on the proximity sensor included integrating laser systems in order to create a more functional sensor. Larger photoarrays and faster acquisition boards were suggested to increase the total operating range of the sensor and frame rate. Other suggestions included were denser mask array designs, angled holes, and better alignment techniques.

APPENDIX A: CODE FOR PARSING IMAGE FILE

The code shown below is used for parsing one particular TC211 proximity sensor, which was the one used in testing. The parsing is specific to each detector because of changes in the hole positions and alignment. The code below was written in Borland TurboC 2.0 but equivalent code was written for Matlab so the same type of processing could be completed on Sun workstations. The code also includes functions for reading the image files off of a diskette or hard drive. Also, a function to subtract dark current from the picture data is included. Any pixels less than zero after subtraction are assumed to be zero.

```
/* Size of pix file array */
#define i_size 165
#define j_size 192

/* Size of Parse Array */
#define i_parse 17
#define j_parse 16

/* The x and y spacing of the holes */
#define x_space 144
#define y_space 151.25

/* Pix file array */
typedef unsigned int pix_matrix[i_size][j_size];

/* Parse Array */
typedef unsigned long int parse_matrix[i_parse][j_parse];
```

```
/*****************************************************/
/* load_pix : loads a pix file and stores it in an    */
/*            array.  Return a true or false for the  */
/*            proper loading of the file.             */
/*                                                    */
/* pix_name : the name of the pix file.               */
/*                                                    */
/* pix : the array where the pix file is stored.      */
/*****************************************************/

int load_pix(char *pix_name,pix_matrix pix)
{
  FILE *pix_file;
  int i,j;

  pix_file = fopen(pix_name,"rb");

  if (!pix_file)
    return(FALSE);

  else
  {
    printf("\nReading %s\n",pix_name);
    /* Removes Header from PIX file */
    for(i=0;i<7;i++)
      getc(pix_file);

    for(i=0;i<i_size;i++)
    {
      for(j=0;j<j_size;j++)
      pix[i][j] = (int)getc(pix_file) + (int)getc(pix_file)*256;

      printf(".");
    }

    fclose(pix_file);

    return(TRUE);
  }
}


/*****************************************************/
/* dodark : Does a dark current subtraction from the  */
/*          the pix array.                            */
/*                                                    */
/* pix_name : the name of the pix file.               */
/*                                                    */
/* pix : the array where the pix file is stored.      */
/*                                                    */
/* dark : the array where the dark file is stored.    */
/*****************************************************/

void dodark(pix_matrix pix, pix_matrix dark)
{
  int i,j;

  /* The sum of the light value and dark current */
  int Sum;
```

```
  for (i=0;i<i_size;i++)
    for(j=0;j<j_size;j++)
    {
      Sum = pix[i][j] - dark[i][j];

      if (Sum < 0)
      pix[i][j] = 0;

      else
      pix[i][j] = (unsigned short) Sum;
    }
}


/******************************************************/
/* parse : Parses the pix file into an array.  Sums   */
/*         the values around the hole.  This parsing  */
/*         is specific to the sensor (slight angle in */
/*         mask)                                      */
/*                                                    */
/* pix : the array where the pix file is stored.      */
/*                                                    */
/* p_matrix : the parsed array.                       */
/******************************************************/

void parse(pix_matrix pix,parse_matrix p_matrix)

{

  /* parsing values.  s and s1 is sloping offset */
  int v,h;
  float s,s1;
  int i,j;
  int is,ifh,js,jfh;
  for(v=2;v<=18;v++)
    for (h=2;h<=17;h++)
    {
      p_matrix[v-2][h-2] = 0;
      s=(18-(double)v)/4;
      s1=(double)h/4;
      is=(int)(9*((float)v-1)-s1+0.5);
      ifh=is+8;
      js= (int)(11*((float)h-1)+1-s+0.5);
      jfh=js+10;
      for(i=is;i <= ifh;i++)
      for(j=js;j <= jfh;j++)
        p_matrix[v-2][h-2] += pix[i][j];
    }
}
```

APPENDIX B: PROPERTIES OF POLYPROPYLENE

Contained below is the manufacture's data on the polypropylene. As extra information, the thermal conductivity is 0.12 W/m-k and the electrical resistivity is $>10^{15}$ Ω-m.

<u>Nominal Physical Properties of Marlex HLN-200 Polypropylene</u>

Property	Value
Density, ASTM D1505, (g/cc)	0.913
Melt Flow, ASTM D1238, Condition 230/2.16 (g/10min)	20
Tensile Yield Strength ASTM D638 Type I specimen, 2 in/min, psi (MPa)	5300 (37)
Flexuaral Modulus ASTM D790, psi (MPa)	290,000 (2000)
Izod Impact Strength ASTM D256, ftlb/in (J/m)	
Notched, (73 F) 23 C	0.4 (21)
Unnotched (73 F) 23 C	15 (800)
Deflection Temperature ASTM D648, F, (C)	
66 psi (0.46 MPa)	260 (127)
264 psi (1.8 Mpa)	170 (77)

Hardness, Shore D ASTM D2240	75
Avg. weighted Molecular Weight	300,000
Recommended Processing Temperature Stock Temperature, F (C)	375-450 (190-232)

Resin Identification System:

- Polymer Type (first letter)
  - H = Homopolymer
- Additive System (second and third letters)
  - L = Antistatic
  - N = Nucleated
- Melt Flow (first three numbers)
  - Melt flow carried to one decimal place (ie, 200 = 20 MFI)

APPENDIX C: CALCULATIONS FOR POINT LIGHT SOURCE

This appendix shows the calculations for a point light source, and the formulas that are used in the simulation. The first set of calculations shows that the projected light circle is a circle and not an ellipse.

The diagram in Figure C-1 is a three dimensional point of view of a light point and a hole. Also shown is the arbitrary axis labeling.

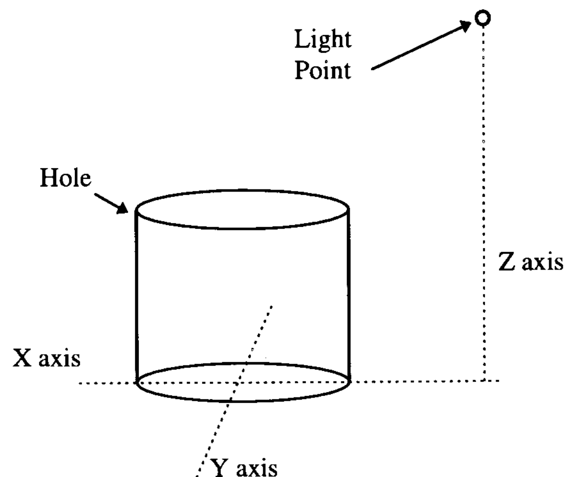

Figure C-1: Three dimensional view of hole

The diagram in Figure C-2 shows an X-Y plane view (above) of a light ray from a point source and intersecting an arbitrary point on the hole (circle) edge. The light source

is aligned in the X axis direction. The value R_{xy} is the distance from the edge of the hole nearest to the light source to a point under the light source on the X-Y plane. The value R_{xy} is assumed to be known, or can be calculated by knowing the distance from the light point to the center of the hole on the X-Y plane, in which R_{xy} can be calculated by subtracting half the hole diameter from it. The value X_p and Y_p is the point relative to the center of the hole of where the light ray intersects the detector surface. The value X_d and Y_d are arbitrary points that the light can intersect the edge of the circle.

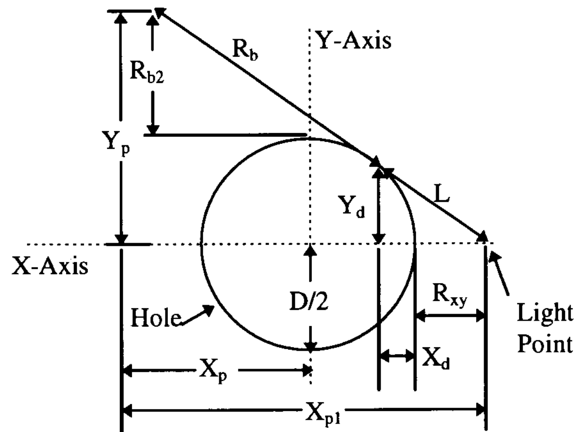

Figure C-2: X-Y view of hole and light point

Figure C-3 is a side view of the hole in the direction of dimension L of Figure C-2. The value t is the thickness of the mask, and the Z is the height from the top of the mask to the point source of light.

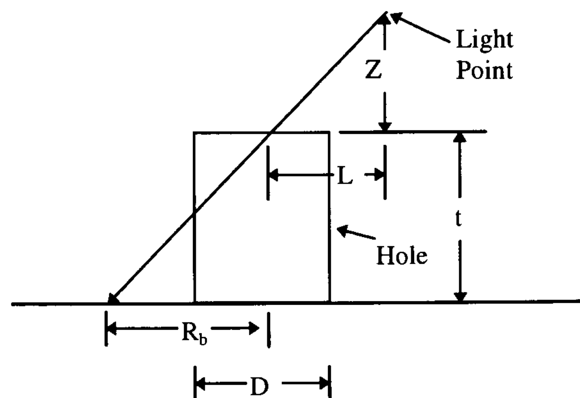

Figure C-3: Side view of light source

The value R_b is shown in equation (C-1) based on the angle of acceptance or the ratio of the sides of similar triangles.

$$\text{(C-1)} \quad R_b = \left(\frac{L}{Z}\right)t$$

The value R_{b2} is shown in equation (C-2).

$$\text{(C-2)} \quad R_{b2} = \left(\frac{Y_d}{L}\right)R_b$$

The value Y_p is shown in equation (C-3).

$$\text{(C-3)} \quad Y_p = R_{b2} + Y_d$$

By replacing (C-1) into (C-2) and then to (C-3) and simplifying, results in equation (C-4) for Y_p.

$$\text{(C-4)} \quad Y_p = \left(1 + \frac{t}{Z}\right)Y_d$$

The equation shows that the value Y_p is linearly related to all values of Y_d which are on the outside of the circle (the hole of the detector). The result would be a circle with a diameter multiplied by a constant. To further show that a circle is projected the value for X_p is found. The value for X_{pl} is shown in equation (C-5).

$$\text{(C-5)} \quad X_{pl} = \frac{(X_d + R_{xy})}{Y_d}Y_p$$

Apply equation (C-4) to (C-5) and simplifying results in equation (C-6).

$$\text{(C-6)} \quad X_{pl} = \left(1 + \frac{t}{Z}\right)(X_d + R_{xy})$$

Equation (C-6) shows that the X_{pl} values are linearly related to the value of X_d which exists in a circle and thus a circle is what would be projected.

The value of X_p is just a shifting of half of the diameter of the circle and the value of R_{xy} as shown in equation (C-7).

$$(C\text{-}7)\quad X_p = X_{pl} - \frac{D}{2} - R_{xy}$$

Applying (C-6) into (C-7) and simplifying results in equation (C-8) for X_p.

$$(C\text{-}8)\quad X_p = \left(1 + \frac{t}{Z}\right)X_d + R_{xy}\frac{t}{Z} - \frac{D}{2}$$

Again the value of X_p is linearly related to X_d and thus a circle is projected from the point of light.

To continue to show a circle is projected, the value of Y_d is shown in equation (C-9).

$$(C\text{-}9)\quad Y_d^{\,2} = \frac{D^2}{4} - \left(\frac{D}{2} - X_d\right)^2$$

Applying equation (C-4) to (C-9) results in a value for Y_p as shown in equation (C-10).

$$(C\text{-}10)\quad Y_p^{\,2} = \left[\left(1 + \frac{t}{Z}\right)\frac{D}{2}\right]^2 - \left[\left(1 + \frac{t}{Z}\right)\frac{D}{2} - \left(1 + \frac{t}{Z}\right)X_d\right]^2$$

Applying (C-8) to (C-10) and simplifying results in equation (C-11).

$$(C\text{-}11)\quad \left(X_p - \frac{Dt}{2Z} - R_{xy}\frac{t}{Z}\right)^2 + Y_p^{\,2} = \left[\left(1 + \frac{t}{Z}\right)\frac{D}{2}\right]^2$$

Equation (C-11) shows the equation of a circle with a radius R_l in equation (C-12) and a center in the X axis of the value C_l as shown in equation (C-13). The value of the

center in the Y axis is zero. The radius and center are relative to the center of the detector circle.

$$(C\text{-}12)\quad R_1 = \left(1+\frac{t}{Z}\right)\frac{D}{2}$$

$$(C\text{-}13)\quad C_1 = \left(\frac{D}{2}+R_{xy}\right)\frac{t}{Z}$$

A circle is projected from the top of the hole in the mask from a point source of light. The diagram in Figure C-4 shows the intersection of the project light circle and the detector circle. The values of C_1 and R_1 are also shown.

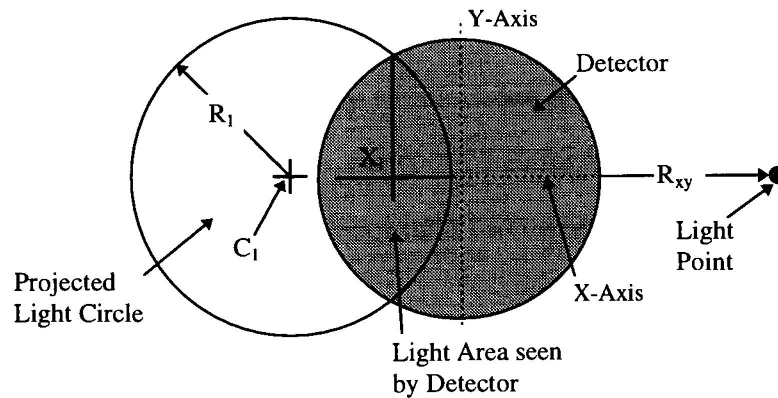

Figure C-4: Intersection of two circles

Finding the X value of the intersection (X_i) of the two circles, the detector and light circle, requires finding the intersection of a half circle. The diagram in Figure C-4 shows the two circles. The origin is based in the center of the detector circle. All of these equations are radially independent, since it is always possible to create an axis that intersects the center of the detector and the light point.

Equation (C-14) shows the half circle formula for the detector.

$$(C\text{-}14)\quad Y=\sqrt{\frac{D^2}{4}-X^2}$$

The half circle formula for the projected light circle is in equation (C-15).

$$\text{(C-15)} \quad Y = \sqrt{R_1^{\;2} - (X - C_1)^2}$$

By making (C-14) equal to (C-15), the value of X_i, the X value of the intercept can be calculated. The final value after simplification is in equation (C-16).

$$\text{(C-16)} \quad Xi = \frac{\left[\frac{D^2}{4} - R_1^{\;2} + C_1^{\;2}\right]}{2C_1}$$

The area in the intersection region is found by using the formula in equation (C-17), which calculates the area in a chord by using the value of the radius (u) of the circle and the distance (v) from center of the circle to the chord (perpendicular to the chord line). Thus by applying (C-17) to both circles, the chord area for both the detector circle and the projected light circle, the percentage area of light falling on the detector can be calculated which is shown in equation (C-18).

$$\text{(C-17)} \quad f(u, v) = u^2 \cos^{-1}\left(\frac{v}{u}\right) - v\left(u^2 - v^2\right)^{\frac{1}{2}}$$

$$\text{(C-18)} \quad A = \frac{\left(f(R_1, C_1 - X_i) + f(0.5D, X_i)\right)}{\pi\left(\frac{D}{2}\right)^2}$$

The total intensity value is calculated with equation (C-19) where the I is a some intensity value and R is the distance from the center of the detector to the light source.

$$\text{(C-19)} \quad I_{total} = \frac{IA}{R^2}$$

The equations (C-18) and (C-19) are only valid for R_{xy} being in the range in (C-20). When the spot is within the edge of the detector just the $1/R^2$ of the intensity will be used. Greater than that the range, the intensity is zero

$$\text{(C-20)} \quad 0 < R_{xy} < \frac{ZD}{t}$$

For taking into account different hole diameters, the value in (C-19) just needs to be multiplied by the square of the hole diameter.

APPENDIX D: CODE FOR SIMULATING THE DETECTOR

The code below contains the two functions necessary to simulate a point source for one detector. The parameters used are for hole size, thickness, distance and light intensity. These functions can be used to simulate an array, where the distance is offset from the spot source.

The values in the function sensor are eventually normalized to the hole diameter and thickness of the mask, which makes the calculations simpler. The formulas are valid for certain ranges, thus depending on the range, determines the formula to be used.

```
/* formula(r,c,point)                                              */
/*  u - radius of circle                                           */
/*  v - distance from chord to center                               */

double formula(double u,double v)
{
  double R1;
  u2 = pow(u,2);
  return(u2*acos(v/u) - v*sqrt(u2 - pow(v,2)));
}

/*  X,Y,Z - Cartesian co-ordinates for light point source */
/*          Z is defined as distance above mask surface    */
/* i - intensity of point of light                         */
/* D - diameter of round sensor                            */
/* t - thickness of mask                                     */
double sensor(double X,double Y,double Z,double i,double D,double t)
{
  double Rxy;
```

```
  double In;
  double light;
  double C1;
  double R1;
  double Xi;
  double on;

  Rxy = pow(X,2) + pow(Y,2);

  In = i/(Rxy + pow(Z+t,2));

/* normalizing the values so the sensor is a circle with */
/* diameter 1                                            */

  Z = Z/t;

  Rxy = sqrt(Rxy)/D - 0.5;

/* Special case where light point is over sensor */
/* no mask effect                                */
  if (Rxy <= 0)
  {
    light = In;
  }

/* special case where the mask is totally covering the sensor */
/* all values have been normalized                            */

  else if ((Z/Rxy) <= 1)
  {
    light = 0;
  }

  else
  {
    center = (0.5 + Rxy)/Z;
    R1 = 0.5/Z + 0.5;

/* X intersection, the Y need not be calculated because of integration
*/
    Xi = (0.25 - pow(R1,2) + pow(C1,2))/(2*C1);

/* calculate what is on or lite, using integration */
    on = formula(R1,C1-Xi) + formula(0.5,Xi);

    on = on/(pi/4);
    light = on*In;
  }


  return(light);
}
```

APPENDIX E: CODE FOR SIMULATING CHECKERBOARD PATTERN

The code below is used for simulating a checkerboard pattern as seen from the TC211 sensor, with the 144 μm and 151.25 μm hole spacing. The simulation uses only six squares that are approximately 1 mm on each side and uses the other functions mentioned previously in Appendix D.

```
/* 1 mm squares                                        */
/* 1e6 light intensity is to increase the              */
/* accuracy when printed to a file                     */
/* Assuming a mask thickness of 500 um and hole        */
/* diameter of 30 um.                                  */

double checker(double Z,double off,double off2)

{

  double answer = 0;

  int a,b=0;

  for (a=1317;a<=2313;a+=3)
    for (b=942;b<=1938;b+=3)
    {
      answer = answer + sensor((double)(a)-off,(double)(b)-
        off2,Z,1000000,30,500);
    }

  for (a=-683;a<=313;a+=3)
    for (b=942;b<=1938;b+=3)
    {
```

```
      answer = answer + sensor((double)(a)-off,(double)(b)-
off2,Z,1000000,30,500);
    }

    for (a=1317;a<=2313;a+=3)
    for (b=-1058;b<=-62;b+=3)
    {
      answer = answer + sensor((double)(a)-off,(double)(b)-
off2,Z,1000000,30,500);
    }

    for (a=-683;a<=313;a+=3)
    for (b=-1058;b<=-62;b+=3)
    {
      answer = answer + sensor((double)(a)-off,(double)(b)-
off2,Z,1000000,30,500);
    }

    for (a=317;a<=1313;a+=3)
    for (b=-58;b<=938;b+=3)
    {
      answer = answer + sensor((double)(a)-off,(double)(b)-
off2,Z,1000000,30,500);
    }

    for (a=317;a<=1313;a+=3)
    for (b=1942;b<=2938;b+=3)
    {
      answer = answer + sensor((double)(a)-off,(double)(b)-
off2,Z,1000000,30,500);
    }

  return(answer);
}


/* main program */

void main()

{ FILE *filepointer;
  char name[30];
  int o,x,y;
  double I;
  float Z;
  double off,off2;
  clrscr();

  printf("file name : ");
  scanf("%s",&name);
  filepointer = fopen(name,"w");
  printf("height : ");
  scanf("%f",&Z);

/* will span at 144 intervals of displacement like a sensor */
/* and for 151.25                                          */
  for (y=0;y<17;y++)
  {
    for (x=0;x<16;x++)
    {
      off = ((double)(x))*151.25;
```

```
        off2 = ((double)(y))*144;
        I=checker(Z,off,off2);
        printf("%f\t",I);
        fprintf(filepointer,"%f\t",I);
      }

      fprintf(filepointer,"\n");
      printf("\n");
    }

    fclose(filepointer);

  }
```

APPENDIX F: CODE FOR SIMULATION OF GAUSSIAN BEAM

The code below is the function for simulating a gaussian beam spot. Multiple points in intervals of 3 μm in a square area with length of $2R_{1/e2}$ are used to simulate the laser spot. Each point has an intensity based on the gaussian beam formula seen in equation (5-1). The intensity at each point is calculated using the function 'sensor' shown in Appendix D. The radius and thickness of the sensor is hard code in these functions, as they were consistently used in simulations.

```
/* Just a gaussian beam for hole            */
/* The value off is from the center of      */
/* the detector to the centroid,center of */
/* the gaussian beam.                       */

double gaussian(double off,double Z,double R)

{

  double answer = 0;

  double I;
  int a,b;

  R = pow(R,2);

/* gassian  */
  for (a=-402;a<=402;a+=3)
    for (b=-402;b<=402;b+=3)
    {
      I=200000*exp(-2*(pow(a,2) pow(b,2))/R));

      answer = answer + sensor(a+off,b,Z,I,30,500);
```

```
    }
return(answer)}
```

APPENDIX G: CODE FOR CALCULATING POSITION

The code contains the functions for calculating the position of the laser spot. The functions in Appendix A have to be used in conjunction. The data is assumed to have been parsed.

```
/****************************************************/
/* max_array : finds the maximum value index in the   */
/*             parse array.                           */
/*                                                    */
/* p_matrix : the parsed array.                       */
/*                                                    */
/* i,j : the array position of the maximum value.     */
/****************************************************/
void max_array(parse_matrix p_matrix,int *i,int *j)

{
  int m,n;
  long int max_value=0;

  *i = 0;
  *j = 0;

  for (m=0;m<i_parse;m++)
    for (n=0;n<j_parse;n++)
    {
      if (p_matrix[m][n] >= max_value)
      {
      max_value = p_matrix[m][n];
      *i = m;
      *j = n;
      }
    }
}
```

```
/*****************************************************/
/* position : Calculates the x,y position of center   */
/*            of the laser beam.  Position is based   */
/*            upon the dimensions of spacing          */
/*                                                    */
/* p_matrix : the parsed array.                       */
/* x,y : the x and y position of the spot (float).    */
/*****************************************************/

void position(parse_matrix p_matrix,double *x,double *y)

{
  int i,j;
  unsigned long int mid, mn;
  int s;
  double a,b;

  max_array(p_matrix,&i,&j);

  if (p_matrix[i-1][j] > p_matrix[i+1][j])
  {
    mid = i-1;
    mn = i+1;
    s=-1;
  }

  else
  {
    mid=i+1;
    mn = i-1;
    s=1;
  }

  a = (double) (p_matrix[mid][j] - p_matrix[mn][j]);
  b = (double) (p_matrix[i][j] - p_matrix[mn][j]);
  *x = (a/b/2*s+1+i)*x_space;

  if (p_matrix[i][j-1] > p_matrix[i][j+1])
  {
    mid = j-1;
    mn = j+1;
    s = -1;
  }
  else
  {
    mid=j+1;
    mn = j-1;
    s=1;
  }
  a = p_matrix[i][mid] - p_matrix[i][mn];
  b = p_matrix[i][j]-p_matrix[i][mn];
  *y = (a/b/2*s+1+j)*y_space;
}
```

APPENDIX H: HSPICE CODE FOR SIMULATION OF INTEGRATED PROXIMITY SENSOR

The code below is the HSPICE file for simulating the integrated proximity sensor as discussed in section 6. The simulation goes through a complete scan of a 2x2 array. The photodiodes are just diodes with an ideal current source in parallel, pulling the current.

```
. Timing Diagram of Embedded Proximity Sensor

*Rails - Vdd and Vss
VDD vdd 0 DC 5
VSS vss 0 DC 0


***************
*Clocking signals for comparison and level triggering

Vclr CLR 0 PULSE 0 5 0n 0.1n 0.1n 10n

**** Clocking signals

Vclk CLK 0 PULSE 0 5 5n 0.1n 0.1n 10n 20n

X10 S0 S0b SCLK AReset vdd vdd vss TT
X11 S0 S1 S1b SCLK AReset vdd vdd vss TFF

** Reset - feedback inverters
X12 S0 S1 PreCharge vdd vss NOR2

***Wait- grab for comp2 just use Grab
*R2 Grab 12 0

***Latchb
X14 S0b S1b Latch vdd vss NOR2
```

```
**More clocking signals but now
**is more of address and finite state machine

*Y address - setting to one, want to skip the first one
X15 QY0 QY0b S1 vdd AReset vdd vss TT

*X address
X16 QX0 QX0b QY0 AReset vdd vdd vss TT

*Stops the clocking of signals and address counter
X17 QT Qtb QX0 AReset vdd vdd vss TT

*Reset all ff expect one value of Y sets it to high
*so starting on 01.00 is winner

X20 CLK CLKb vdd vss INV

X60 QT Q1b 60 vdd vss NAND2
X61 60 Q0b T0 vdd vss NAND2

X18 T0 Q0 Q0b CLKb CLRb vdd vdd vss TFF

X80 Q0b Q1b T1 vdd vss NAND2
X70 T1 Q1 Q1b CLKb CLRb vdd vdd vss TFF


*Signal for stopping signal
X19 QTb CLK SCLK vdd vss NAND2

X99 Q1 CLR AReset vdd vss NOR2

X51 CLR CLRb vdd vss INV


 *****Comparisions

* winner voltage - will use for now


Id A vss PULSE 0u 50u 0n 0.1n 0.1n 60n
vtester A A1 DC 0

* Just a voltage copy of the current for A (compare)
* Used so can see which is greater in the voltage domain
Vcopy IC vss PULSE 0 5 0n 0.1n 0.1n 60n
Rcopy IC vss 10K

X500 vss A1 vdd PDiode
X501 vss B vdd PDiode2

X1 A B gt lt PreCharge S1 vdd vss COMP2

X3 gt Latch wCLK vdd vss NAND2

*Winner Register
X100 QY0 QYW0 QYW0b wCLk AReset vdd vdd vss DFF
X102 QX0 QXW0 QXW0b wCLK AReset vdd vdd vss DFF

****Final signal is from 19, clock trigger for registers
```

```
*Buffer for final winner
X103 Q0 Q1b FClk vdd vss NAND2
X104 QYW0 QYF0 QYF0b FCLK CLRb vdd vdd vss DFF
X105 QXW0 QXF0 QXF0b FClk CLRb vdd vdd vss DFF


.TRAN 0.8n 350n
.OPTIONS METHOD=GEAR POST
.PRINT V(CLK) V(IC) V(PRECHARGE) V(S1) V(LATCH) V(QX0) V(QY0) V(WCLK)
+ V(FCLK) V(QXW0) V(QYW0) V(QYF0) V(QXF0)

.PLOT V(gt)

*.meas tran avgpow avg p(vdata)

.subckt INV in out vdd vss
  M1 out in vdd vdd PCH15 L=1.5U W=6.3U
  M2 out in vss vss NCH15 L=1.5U W=3.3U
.ends INV


.subckt TGATE in out cp cn vdd vss
Vt1 in in1 0
M1 in1 cp out vdd PCH15 L=1.5U W=7.8U


Vt2 in in2 0
M2 in2 cn out vss NCH15 L=1.5U W=6.6U
.ends TGATE

.subckt NAND2 A B Y vdd vss
  M1 Y A vdd vdd PCH15 L=1.5u W=8.3u
  M2 Y B vdd vdd PCH15 L=1.5u W=8.3u
  M3 Y A mid vss NCH15 L=1.5u W=6.6u
  M4 mid B vss vss NCH15 L=1.5u W=6.6u
.ends NAND2


.subckt NOR2 A B Y vdd vss
  M1 mid A vdd vdd PCH15 L=1.5u W=6.6u
  M2 Y B mid vdd PCH15 L=1.5u W=6.6u
  M3 Y A vss vss NCH15 L=1.5u W=3.3u
  M4 Y B vss vss NCH15 L=1.5u W=3.3u
.ends NOR2


.subckt NAND3 A B C Y vdd vss
  M1 Y A vdd vdd PCH15 L=1.5u W=8.3u
  M2 Y B vdd vdd PCH15 L=1.5u W=8.3u
  M3 Y C vdd vdd PCH15 L=1.5u W=8.3u
  M4 Y A mid1 vss NCH15 L=1.5u W=6.6u
  M5 mid1 B mid2 vss NCH15 L=1.5u W=6.6u
  M6 mid2 C vss vss NCH15 L=1.5u W=6.6u
.ends NAND3

*comparitor circuit


*This one needs Pre and Grad seperated
.subckt COMP2 A B AgB AgBb Pre Grab vdd vss
```

```
  X1 pre eval vdd vss INV

  *M1 vdd eval A vss NCH15 L=1.5u W=6.6u
  *M2 vdd eval B vss NCH15 L=1.5u W=6.6u

  *M3 AO pre A vss NCH15 L=1.5u W=6.6u
  *M4 BO pre B vss NCH15 L=1.5u W=6.6u
  X11 A AO eval pre vdd vss TGATE
  X12 B BO eval pre vdd vss TGATE

  X2 AO BO eval pre vdd vss TGATE

  X3 AO BO vdd vss INV
  X4 BO AO vdd vss INV

  X5 Grab Grabb vdd vss INV
  X6 BO Y0 Grabb Grab vdd vss TGATE

  X7 Y0 AgBb vdd vss INV
  X8 AGBb AgB vdd vss INV
  X9 AgB Y0 Grab Grabb vdd vss TGATE

.ends COMP2



**J-K flip-flop
.subckt JKFF J K Q NQ CLK SETB CLRB vdd vss
  X1 NQ J CLK X1Y vdd vss NAND3
  X2 CLK K Q X2Y vdd vss NAND3
  X3 SETB X1Y X4Y X3Y vdd vss NAND3
  X4 X3Y X2Y CLRB X4Y vdd vss NAND3
  X5 X3Y X9Y X5Y vdd vss NAND2
  X6 X9Y X4Y X6Y vdd vss NAND2
  X7 X5Y SETB NQ Q vdd vss NAND3
  X8 Q CLRB X6Y NQ vdd vss NAND3
  X9 CLK X9Y vdd vss INV
.ends JKFF

*one half of dflip
*loop is the signal needed for looped inverters

.subckt Hff in out resetb setb loop loopb vdd vss
  X1 in n1 loop loopb vdd vss TGATE
  X2 n1 resetb outb vdd vss NAND2
  X3 outb setb out vdd vss NAND2
  X4 out n1 loopb loop vdd vss TGATE
.ends Hff


*D flip-flop
.subckt DFF D Q Qb CLK Resetb Setb vdd vss
  X1 CLK CLKb vdd vss INV

  X2 D n1 Resetb Setb CLKb CLK vdd vss Hff
  X3 n1 Q Resetb Setb CLK CLKb vdd vss Hff
  X4 Q Qb vdd vss INV

.ends DFF
```

```
*T - toggle
*This has no toggle enable, always toggle on clock

.subckt TT Q Qb CLK Resetb Setb vdd vss
  X1 Qb Q Qb CLK Resetb Setb vdd vss DFF
.ends TT


*T-flip

.subckt TFF T Q Qb CLK Resetb Setb vdd vss

  X1 T Tb vdd vss INV

  X2 Qb D Tb T vdd vss TGATE
  X3 Q D T Tb vdd vss TGATE

  X4 D Q Qb CLK Resetb Setb vdd vss DFF

.ends TFF

*photodiodes two different photo currents
.subckt PDiode P N1 vdd
M1 P P N1 vss NCH15 L=1.5U W=8.3U
.ends PDiode

.subckt PDiode2 P N1 vdd
M1 P P N vss NCH15 L=1.5U W=8.3U
Id N P DC 25u
Vtest N N1 DC 0
.ends PDiode2


.model NCH15 nmos
+(  level=3           ld=239.68n        lmlt=1            wd=100p
+   wmlt=1            vto=827.59m       tpg=1             phi=725.15m
+   gamma=585.84m     nsub=1.6e16       cgbo=255.79f      cgdo=268.57p
+   cgso=268.57p      capop=12          cf2 =100m         cf3=1
+   cf4=50            cf5=666.67m       cf6 =500          xqc =500m
+   tox=27n           cox=1.28m         is=10f            nds=1
+   cj=418.85u        mj=500m           mjsw=330m         pb=800m
+   php=800m          rsh=62.8          fc=500m           n=1
+   vnds=-1           tlev=0            tlevc=0           eg=1.11
+   gap1=473u         gap2=636          xti=3             bex=-1.5
+   af=1              nlev=2            gdsnoi=1          delta=1.06
+   eta=140.68m       kappa=10m         nfs=868.21g       theta=34.67m
+   vmax=160.4k       xj=296.9n         uo=531.92         kp=68.03u
+   deriv=1      )

.model PCH15 pmos
+(  level=3           ld=152.9n         lmlt=1            wd=97.74n
+   wmlt=1            vto=-559.63m      tpg=-1            phi=765.08m
+   gamma=863.96m     nsub=3.6e16       cgbo=250.01p      cgdo=250.66p
+   cgso=250.66p      capop=12          cf2=100m          cf3=1
+   cf4=50            cf5=666.67m       cf6=500           xqc=500m
+   tox=27n           cox=1.28m         is=10f            nds=1
+   cj=617.69u        mj=500m           mjsw=330m         pb=800m
+   php=800m          rsh=65.23         fc=500m           n=1
+   vnds=-1           tlev=0            tlevc=0           eg=1.11
+   gap1=473u         gap2=636          xti=3             bex=-1.5
+   af=1              nlev=2            gdsnoi=1          delta=1.53
```

```
+   eta=146.55m      kappa=5.69        nfs=224.75g      theta=35.94m
+   vmax=216.54k     xj=409.39n        uo=138.03        kp=17.65u
+   deriv=1      )

.end
```

APPENDIX I: CODE FOR EDC1000L

The code in this appendix is for processing the data from the EDC1000L board which gathers data from a TC245. The code contained is a module for doing the proximity calculations and dark current subtractions. Essentially, the code is more generic especially for the parsing function. The programs also handles the larger amounts of data from the TC245.

```
/*****************************************************/
/* This module is a modification on the program      */
/* prox.c.  It will be used for the TC245 instead of  */
/* the TC211.  This is used as a module because       */
/* integration is easier, and because global local    */
/* variables are going to be created related to the   */
/* parsing information, such as grid size, slope of   */
/* mask etc.  The information wil be stored in a file */
/* called "parse.val" standing for parsing values.    */
/* These values must exist in the same directory as   */
/* where the program is being called from.            */
/*                                                    */
/* Create Oct 15, 1995 by Darren Bergen - program     */
/* Modified for module Dec 16, 1995 by Darren Bergen  */
/*****************************************************/

#include <stdio.h>
#include <conio.h>
#include <string.h>
#include <stdlib.h>
#include <math.h>

#include "tc245.h"
#include "prox.h"
```

```
#define parse_name "parse.val"

/* Start of the parsing in the vertical and horizon-  */
/* tal values.                                        */
int V_start,H_start;

/* The Number of vertical and horizontal holes, parse */
/* The values in prox.h are the maximum, these values */
/* are set by the file parse.val.                     */
int NV,NH;

/* The slope of the holes when parsing. This becomes */
/* an slope applied for each hole                    */
int slope;

/* The size of the parsing area in the vertical and  */
/* horizontal.                                       */
int SV,SH;

/* The sin and cos values calculated from the slope   */
/* Used for the rotations of mask.                    */
double SinVal, CosVal;


/*****************************************************/
/* init_parse : loads the values for the parsing from */
/*              the file parse.val                    */
/*****************************************************/

void init_parse()
{
  FILE *parse_file;

  parse_file=fopen(parse_name,"r");

  if (parse_file == NULL)
  {
    printf("Cannot Read parsing information file (%s)",parse_name);
    exit(0);
  }

  fscanf(parse_file,"%d %d %d %d %d %d
%d",&V_start,&H_start,&NV,&NH,&slope,
    &SV,&SH);

  SinVal=sin(atan((double)slope));
  CosVal=cos(atan((double)slope));

  fclose(parse_file);
}


/*****************************************************/
/* max_array : finds the maximum value index in the   */
/*             parse array.                           */
/*                                                    */
/* p_matrix : the parsed array.                       */
/*                                                    */
/* i,j : the array position of the maximum value.     */
/*****************************************************/
```

```
void max_array(parse_matrix p_matrix,int *i,int *j)

{
  int m,n;
  long int max_value=0;

  *i = 0;
  *j = 0;

  for (m=0;m<NV;m++)
    for (n=0;n<NH;n++)
    {
      if (p_matrix[m][n] >= max_value)
      {
      max_value = p_matrix[m][n];
      *i = m;
      *j = n;
      }
    }
}


/*****************************************************/
/* dodark : Does a dark current substraction from the */
/*          the pix array.                            */
/*                                                    */
/* buffer : the array where the buffer is stored.     */
/*                                                    */
/* dark : the array where the dark current is stored. */
/*****************************************************/

void dodark(buffer_array buffer, buffer_array dark)
{
  int i,j;

  /* The sum of the light value and dark current */
  int Sum;

  for (i=0;i<V;i++)
    for(j=0;j<H;j++)
    {
      Sum = buffer[i][j] - dark[i][j];

      if (Sum < 0)
      buffer[i][j] = 0;

      else
      buffer[i][j] = (unsigned short) Sum;
    }
}


/*****************************************************/
/* parse : Parses the buffer into an array.  Sums the */
/*         values around the hole.  This parsing is   */
/*         specific to the sensor (slight angle in    */
/*         mask)                                      */
/*                                                    */
/* buffer : the array where the buffer is stored.     */
/*                                                    */
/* p_matrix : the parsed array.                       */
```

```
/*****************************************************/

void parse(buffer_array buffer,parse_matrix p_matrix)

{
  int i_start,j_start;
  int v,h,i,j;

  for(v=0;v<NV;v++)
    for (h=0;h<NH;h++)
    {
      p_matrix[v][h] = 0;

      i_start=V_start+V_space*CosVal*v-H_space*SinVal*h;
      j_start=H_start+V_space*SinVal*v+H_space*CosVal*h;

      for(i=i_start-1;i < i_start+SV;i++)
      for(j=j_start-1;j < i_start+SH;j++)
        p_matrix[v][h] += buffer[i][j];
    }

}


/*****************************************************/
/* position : Calculates the x,y position of center  */
/*            of the laser beam.  Position is based  */
/*            upon the dimensions of spacing         */
/*                                                   */
/* p_matrix : the parsed array.                      */
/* x,y : the x and y position of the spot (float).   */
/*****************************************************/

void position(parse_matrix p_matrix,double *x,double *y)

{
  int i,j;
  unsigned long int mid, mn;
  int s;
  double a,b;

  max_array(p_matrix,&i,&j);

  if (p_matrix[i-1][j] > p_matrix[i+1][j])
  {
    mid = i-1;
    mn = i+1;
    s=-1;
  }

  else
  {
    mid=i+1;
    mn = i-1;
    s=1;
  }

  a = (double) (p_matrix[mid][j] - p_matrix[mn][j]);
  b = (double) (p_matrix[i][j] - p_matrix[mn][j]);
  *x = (a/b/2*s+1+i)*x_space;
```

```
if (p_matrix[i][j-1] > p_matrix[i][j+1])
{
  mid = j-1;
  mn = j+1;
  s = -1;
}
else
{
  mid=j+1;
  mn = j-1;
  s=1;
}
a = p_matrix[i][mid] - p_matrix[i][mn];
b = p_matrix[i][j]-p_matrix[i][mn];
*y = (a/b/2*s+1+j)*y_space;}
```

REFERENCES

1. Daniel F. García, Manuel García, Jose L. Diaz, José R. Arias, Javier Gracía, "Real-Time Flatness Sensor Based on a Linear-Vision Multiprocessor System (RV-05)", *IECON '94*, 1994, p873-878

2. William N. Kaliardos, "Sensors for autonomous navigation and hazard avoidance on a planetary micro-rover", *Sensing, Imaging, and Vision for Control and Guidance of Aerospace Vehicles*, SPIE, 1994, p 59-68.

3. Hrishikesh P. Gadagkar, Mohan M. Trivedi and Nils Lassiter, "Versatile Multimodal Systems for Surface Profile Measurements using a Wrist-Mounted Laser Device", *Sensor Fusion V*, SPIE, 1992, p 466-474.

4. Sixto L. Vázquez, Plesent W. Goode, "Proportional proximity sensing for Telerobots using Coherent Laser Radar:, *Cooperative Intelligent Robotics in Space III*, SPIE, 1992, p 25-35.

5. Piotr Jasiobedzki, Michael Jenkin, Evanelos Milios, Brian Down, John Tsotso, Todd Campbell, "Laser Eye - a new 3D sensor for active vision", *Sensor Fusion VI*, 1993, p 316-321.

6. Rainer G. Dorsch, Gerd Häusler, and Jürgen M.Herrmann, "Laser triangulation: fundamental uncertainty in distance measurement", Applied Optics, March 1 1994, p 1306-1314.

7. Takashi Miyoshi and Yasuhiro Takaya, "Optical Ring Image 3-D Profile Sensor", *Measurement Technology and Intelligent Instruments*, SPIE, 1993, p 1014-1024.

8. *CCD Linear Image Sensor*, Toshiba, 1991, p 10-11.

9. *Area Array Image Sensor Products Data Book*, Texas Instruments, 1994.

10. Richard Berry, Veikko Kanto and John Munger, *CCD Camera Cookbook*, Willmann-Bell, Inc., Richmond, Virginia, 1994.

11. Bruce E. Warner and Paul D. Weber, "High Power Copper Vapor Lasers and Their Application to Precision Drilling and Cutting", *LEOS '93 Conference Proceedings*, pp. 782-783, IEEE Lasers and Electro-Optics Society, San Jose, Nov. 1993.

12. M.R.H. Knowles, R. Foster-Turner, and A.J. Kearsley, "Copper Lasers Go for Industrial Gold", IEEE Circuits and Devices, Vol. 10 No. 5, pp. 39-42, September 1994.

13. You-Wen Yau, David C.Long, William T. Grant, Nirmal S. Sandhu, and Joseph J. Fulton, "Overview of Via Formation Technologies for Ceramic Packaging Manufacturing", *43rd Electronic Components and Technology Conference*, pp. 155-158, IEEE, Orlando, June 1993.

14. B. Haba, Y. Morishige, S. Kishida, "Laser through hole drilling and laser cutting in teflon", Applied Physics A60, 1995, Vol. A60 No. 1, pp. 27-30, 1995.

15. B. Haba, Y. Morishige, S. Kishida, "Novel Technique of Laser Through-Hole Drilling in Teflon", Japanese Journal of Applied Physics, Vol. 33 No. 10B, pp. L1499-501, Oct. 1994.

16. B. Haba and Y. Morishige, "Novel drilling technique in polyimide using visible laser", Applied Physics Letters, Vol. 66 No. 26, pp. 3591-3, June 1995.

17. W.D. Callister, JR., *Materials Science and Engineering*, table C.4, John Wiley & Sons, Inc., New York, 1985.

18. Rafael C. Gonzalez and Richard E. Woods, *Digital Image Processing*, Addison Wesley Publishing Company, Inc., U.S.A., 1993, pp.191-192.